DESIGN OF SHAPE CHARGES

An Analytical Study of Design Parameters in Military Shape Charges

Emalie Halifax (2222482)
Advanced Physics of OME ACDB5015 | Ordnance, Munitions and Explosives Degree Apprenticeship

Word Count – 5,376

Abstract

The jet formation and penetration capability of two shaped charge designs are analysed in this report, using the Finite Element Analysis (FEA) software Abaqus. Design One consisted of a shaped charge with a continuous thickness copper liner, whereas Design Two had a gradual thickness copper liner which increased in thickness from the apex to the base. Both designs were simulated in 2D, before Design One was simulated in 3D.

The 2D simulations produced a jet capable of penetrating a steel target. The simulations were conducted initially without a target and both designs produced jets of a comparable length of 1.5-2m, travelling at approximately $4kms^{-1}$. Design Two penetrated the target further than Design One. The additional mass in the liner was considered to be a key factor in this difference.

The 3D simulation required additional mesh techniques to be applied to sections of the design. The enabled a jet to be formed, however, it was not a typical shaped charge jet. Target penetration did occur, when the target had a course mesh, and a finer mesh significantly affected the jet formation. A recommendation to explore this concept further was given.

Table of Contents

Abstract i
Table of Contents ii
Table of Figures iv
Table of Tables vi
Table of Equations vi
1 Introduction 1
2 Background Theory 1
2.1 Liner Collapse and Jet Formation 1
2.2 Stand-off Distance 3
3 Design Parameters of Military Shaped Charges 4
4 Modelling Shaped Charges 5
4.1 Finite Element Analysis 5
4.2 Material Models and Equations of State 5
4.2.1 Johnson Cook (JC) Material Model 6
4.2.2 Jones-Wilkins-Lee (JWL) Equation of State 6
4.2.3 Mie–Grüneisen Equation of State 6
5 Design of The Model and Analysis Parameters 7
5.1 The 2D Design 7
5.1.1 The 2D Mesh 10
5.2 Material Properties 12
6 2D Simulation 15
6.1 Design One Analysis 15
6.1.1 Design One Jet Formation Analysis 15
6.1.2 Design One Target Penetration Analysis 27
6.2 Design Two Analysis 36
6.2.1 Design Two Jet Formation Analysis 36
6.2.2 Design Two Target Penetration Analysis 47
7 3D Simulation 55
7.1 The 3D Model 55
7.1.1 The 3D Mesh 55
7.1.2 3D Adaptive Mesh 58
7.2 3D Analysis 58
7.2.1 3D Jet Formation Analysis 58

7.2.2 3D Target Penetration Analysis 67
7.2.2.1 Initial 3D Target Penetration Simulation Analysis 67
7.2.2.2 Second 3D Target Penetration Simulation Analysis 76
8 Conclusion 84
9 References 86

Table of Figures

Figure 2-1 – Cross Section of a Typical Shaped Charge Design with A Conical Liner [2]..... 1
Figure 2-2 – Liner Collapse of a Shaped Charge Highlighting the Detonation Wave Propagation, and Jet Formation [10] 2
Figure 2-3 - Schematic of the Standoff Distance for a Shaped Charge [1] 3
Figure 3-1 –Designs of Shaped Charges Showing a) A Small Apex Conical Shaped Charge and b) A Hemispherical Shape Charge Design [4] 4
Figure 4-1 - Simple Representation of 2D Meshing in Finite Element Analysis 5
Figure 5-1 - Assembled 2D Symmetrical Designs 7
Figure 5-2 - Design One Individual Component Detailed Sketches of a) The Casing, b) The High Explosive and c) The Liner. All Dimensions Shown in Meters. 8
Figure 5-3 - Design Two Individual Component Detailed Sketches of a) The Casing, b) The High Explosive and c) The Liner 9
Figure 5-4 - Target Sketch with Dimensions 10
Figure 5-5 - Design One Assembled 2D Mesh 11
Figure 5-6 - Design Two Assembled 2D Mesh 11
Figure 5-7 - Target 2D Mesh 12
Figure 6-1 - 2D_Design_One_Jet_Run Pressure Exerted from the Detonation Wave at a) $2.262x10^{-5}$s, b) $3.0014x10^{-5}$s, c) $4.0034x10^{-5}$s and d) $6.4008x10^{-5}$s 16
Figure 6-2 – 2D_Design_One_Jet_Run Pressure Exerted on the Apex of the Liner During the Start of the Liner Collapse at a) $3.0014x10^{-5}$s and b) $4.4003x10^{-5}$s 17
Figure 6-3 - 2D_Design_One_Jet_Run Compressive and Tensile Stresses from the Detonation Wave at a) $2.262x10^{-5}$s, b) $3.0014x10^{-5}$s, c) $4.003x10^{-5}$s and d) $6.4008x10^{-5}$s 18
Figure 6-4 - 2D_Design_One_Jet_Run Stress Exerted on the Apex of the Liner During the Start of the Liner Collapse at a) $3.0014x10^{-5}$s and b)$8.8002x10^{-5}$ s 19
Figure 6-5 - 2D_Design_One_Jet_Run Jet formation from Liner Collapse to Abortion 21
Figure 6-6 - 2D_Design_One_Jet_Run Full Jet at Point of Abortion 22
Figure 6-7 - 2D_Design_One_Jet_Run Full Jet at Point of Abortion with End Two Nodes Highlighted 22
Figure 6-8 - 2D_Design_One_Jet_Run Jet Formation with Realistic Jet Length Highlighted 23
Figure 6-9 - 2D_Design_One_Jet_Run Displacement Graph for Nodes 34 And 164 24
Figure 6-10 - 2D_Design_One_Jet_Run a) Velocity Graph During Jet Formation Highlighting b) Selected Nodes 25
Figure 6-11 - 2D_Design_One_Jet_Run a) Velocity Graph During Jet Formation Disregarding Node 34 with b) Selected Nodes 26
Figure 6-12 – 2D_Design_One_Target_Run Jet Formation Results 28
Figure 6-13 – 2D_Design_One_Target_Run Displacement Graph For Nodes Highlighted In Figure 6-12b 29
Figure 6-14- 2D_Design_One_Target_Run Initial Impact on The Target a) with The Liner Shown and b) without The Liner Shown 30
Figure 6-15 – 2D_Design_One_Target_Run Jet Penetration Depth at a) $3.06x10^{-4}$s, b) $3.14x10^{-4}$s, c) $3.26x10^{-4}$s, d) $3.40x10^{-4}$s, e) $4.82x10^{-4}$s and f) $4.99x10^{-4}$s 31
Figure 6-16 –2D_Design_One_Target_Run Target Element Deletion Due to Damage at a) $3.14x10^{-4}$s, and b) $3.40x10^{-4}$s, ... 32
Figure 6-17 – 2D_Design_One_Target_Run Final Penetration Depth 34

Figure 6-18 - 2D_Design_One_Target_Run a) Velocity Graph During Jet Formation and Target Penetration with b) Selected Nodes 35
Figure 6-19 - 2D_Design_Two_Jet_Run Pressure Exerted from the Detonation Wave at a) $2.262x10^{-5}$s, b) $3.0014x10^{-5}$s, c) $4.0014x10^{-5}$s and d) $6.4002x10^{-5}$s 37
Figure 6-20 – 2D_Design_Two_Jet_Run Pressure Exerted on Apex Of Liner During Start Of Liner Collapse At a) $3.0014x10^{-5}$s and b) $4.4006x10^{-5}$s 38
Figure 6-21 - 2D_Design_Two_Jet_Run Compressive and Tensile Stresses from the Detonation Wave at a) $2.262x10^{-5}$s, b) $3.0014x10^{-5}$s, c) $4.0014x10^{-5}$s and d) $6.4002x10^{-5}$s 40
Figure 6-22 - 2D_Design_Two_Jet_Run Stress Exerted on Apex of Liner During Start Of Liner Collapse At a) $3.0014x10^{-5}$s and b) $8.8001x10^{-5}$ s 41
Figure 6-23 -2D_Design_Two_Jet_Run Stress Exerted on Apex of Liner During Start of Liner Collapse At $9.2002x10^{-5}$ s 42
Figure 6-24 - 2D_Design_Two_Jet_Run Jet Formation from Liner Collapse to Point of Abortion .. 43
Figure 6-25 - Comparison of a) 2D_Design_One_Jet_Run and b) 2D_Design_Two_Jet_Run Jet Formation at Point of Abortion 44
Figure 6-26 - 2D_Design_Two_Jet_Run a) Node Displacement Graph for b) Selected Nodes..... 45
Figure 6-27 - 2D_Design_Two_Jet_Run a) Velocity Graph During Jet Formation Using b) Selected Nodes 46
Figure 6-28 – 2D_Design_Two_Target_Run Full Jet Formation 48
Figure 6-29 - 2D_Design_Two_Target_Run a) Displacement Graph with b) Selected Nodes 49
Figure 6-30- 2D_Design_Two_Target_Run Initial Impact on Target a) with the Liner shown and b) Without the Liner shown 50
Figure 6-31 – 2D_Design_Two_Target_Run Jet Penetration Depth at a) $3.06x10^{-4}$s, b) $3.14x10^{-4}$s, c) $3.64x10^{-4}$s, d) $4.02x10^{-4}$s, e) $4.16x10^{-4}$s and f) $6.50x10^{-4}$s 51
Figure 6-32 - Stress Comparison between 2D_Design_One_Target_Run and 2D_Design_Two_Target_Run 52
Figure 6-33 – 2D_Design_Two_Target_Run Final Penetration Depth 53
Figure 6-34 - 2D_Design_Two_Target_Run Jet Tip a) Velocity Graph for b) Selected Nodes 54
Figure 7-1 - Assembled 3D model of Design One 55
Figure 7-2 – The 3D Shaped Charge Design a) Assembled Mesh with b) The Partitions Highlighted 56
Figure 7-3 - The 3D Target Design a) Mesh with b) The Partitions Highlighted 57
Figure 7-4 - 3D Model - Standard Mesh - Excessively Distorted Nodes 58
Figure 7-5 - 3D_Design_Jet_Run Results – Pressure Exerted From the Detonation Wave at a)$1.9648x10^{-5}$s, b) $3.4048x10^{-5}$s, c) $4.6028x10^{-5}$s and d) $6.8005x10^{-5}$s 60
Figure 7-6 - 3D_Design_Jet_Run Results – Tensile and Compressive Stress Exerted From the Detonation Wave at a)$1.9648x10^{-5}$s, b) $3.4048x10^{-5}$s, c) $4.6028x10^{-5}$s and d) $6.8005x10^{-5}$s. 61
Figure 7-7 - 3D_Design_Jet_Run Apex Pressure at a) $2.8062x10^{-5}$s and b) $5.6018x10^{-5}$s 62
Figure 7-8 - 3D_Design_Jet_Run Compressive Stress at a) $3.4048x10^{-5}$s and b) $5.6018x10^{-5}$s ... 63
Figure 7-9 - 3D_Design_Jet_Run Jet Formation from Liner Collapse to Abortion 64
Figure 7-10 - 3D_Design_Jet_Run a) Displacement Graph with b) Selected Nodes 65
Figure 7-11 -3D_Design_Jet_Run a) Velocity Graph During Jet Formation with b) Selected Nodes 66
Figure 7-12 - Initial Target 3D mesh 67
Figure 7-13 - 3D_Design_Target_Run_1 Jet Formation from Liner Collapse to Point of Abortion . 68
Figure 7-14 - 3D_Design_Target_Run_1 a) Displacement Graph with b) Selected Nodes 69
Figure 7-15 - 3D_Design_Target_Run_1 a) Velocity Graph with b) Selected Nodes 70

Figure 7-16 - 3D_Design_Target_Run_1 Initial Target element deletion at 2.78x10^{-4}s. 71
Figure 7-17 -- 3D_Design_Target_Run_1 Progression in Shear Stress at a) 2.72x10^{-4}s, b) 2.78x10^{-4}s, c) 2.96x10^{-4}s and d) 3.04x10^{-4} 72
Figure 7-18 - 3D_Design_Target_Run_1 Penetration Progression in Max Principle at a) 2.72x10^{-4}s, b) 2.78x10^{-4}s, c) 2.96x10^{-4}s and d) 3.04x10^{-4}s 73
Figure 7-19 - 3D_Design_Target_Run_1 Representation of Shear Stress Radiating Towards the Edge of the Target 74
Figure 7-20 - 3D_Design_Target_Run_1 Penetration Depth 75
Figure 7-21 – 3D Target Finer Mesh Detailed View 76
Figure 7-22 - 3D_Design_Target_Run_2 Jet Formation from Liner Collapse to Point of Abortion . 77
Figure 7-23 - 3D_Design_Target_Run_2 a) Displacement Graph with b) Selected Nodes 78
Figure 7-24 - 3D_Design_Target_Run_2 a) Jet Velocity Graph with b) Selected Nodes 79
Figure 7-25 - 3D_Design_Target_Run_2 Liner Pressure at a) 2.8191x10^{-5}s, b) 3.4123x10^{-5}s, and c) 5.8909x10^{-5}s 81
Figure 7-26 - 3D_Design_Target_Run_2 Max Principal Stress at a) 2.8191x10^{-5}s, b) 3.4123x10^{-5}s, and c) 5.8909x10^{-5}s 82
Figure 7-27 - 3D_Design_Target_Run_2 Shear stress at a) 3.4123x10^{-5}s, and b) 5.8909x10^{-5}s ... 83
Figure 7-28 - 3D_Design_Target_Run_2 Target Interaction 84

Table of Tables

Table 5-1 – Material Models and EOS Used in Models 13
Table 5-2 - AISI 1045 Steel Material Properties [9, 16, 17, 18] 13
Table 5-3 - OFHC Copper Material Properties [19, 20] 14
Table 5-4 - Comp B Material Properties [14, 21] 14

Table of Equations

4-1 6
4-2 6
4-3 6

1 Introduction

Shaped charges are used in both the Defence and Civilian sectors for cutting and penetrating targets. Their design can impact their overall performance and can be tailored depending on the desired use. This report analyses the jet formation and penetration capability of two shaped charge designs, using the Finite Element Analysis (FEA) software Abaqus with the teaching license. Specifically, the focus is on comparing the effect of a constant thickness liner and a gradual thickness liner. The evaluation of both designs was conducted initially in 2D, with one design taken forward for 3D simulation and analysis.

2 Background Theory

A shaped charge is an explosive device used across the Defence and Civilian sectors to cut or penetrate targets in the air, on land or underwater [1]. A typical shaped charge is shown in Figure 2-1 [2] and consists of a cylinder of explosive, a lined cavity at one end and a detonator at the other. Depending on the desired effect, the lined cavity may be conical, hemispherical, elliptical, trumpeted, or any symmetrical shape [1, 3]. The liner consists of a thin layer of metal, alloy, plastic, or any ductile material which may form a jet under the appropriate conditions [1, 3, 4, 5, 6].

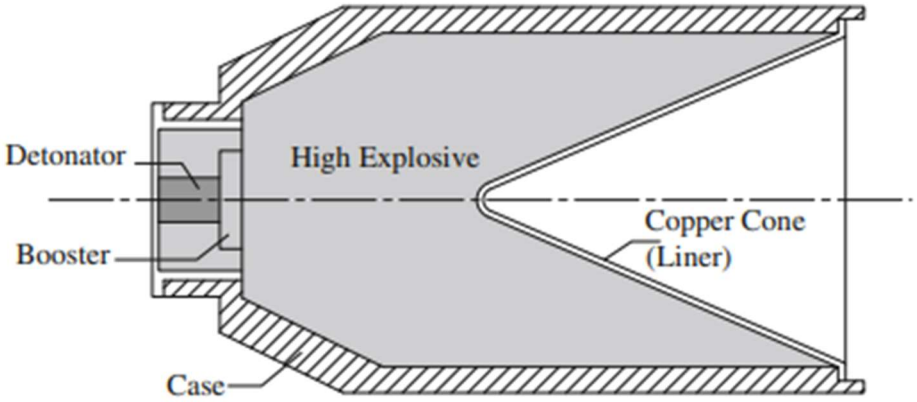


Figure 2-1 – Cross Section of a Typical Shaped Charge Design with A Conical Liner [2]

During the detonation process, a spherical wave propagates through the explosive material producing high pressure and energy. Due to the shape of the liner, the detonation products are focused on the apex, producing a concentrated localised force. When positioned against or above a metal target, this directional force enables the shaped charge to penetrate further compared to a cylinder of explosive of the same height and diameter, where more explosive material would be present. This is known as the Munroe effect [1, 3, 4, 7].

2.1 Liner Collapse and Jet Formation

There are two main theories which describe the shaped charge jet formation: the steady state theory developed by Birkoff et al [4, 8]; and the unsteady state theory developed by Pugh et al [4, 8]. The steady state theory assumes a continuous, uniform jet formation whereas the unsteady

state theory accounts for material imperfections, variations in explosive detonation and instabilities in the jet formation.

The high pressure exerted on the apex of the liner, generated from the explosive material, has been shown to be in the range of 20 – 2,000 GPa [7, 9]. At this range materials behave like an inviscid incompressible fluid [7, 8, 9] meaning the mechanical strength becomes negligible in comparison to the applied pressure. The pressure causes the liner to collapse from its apex, towards a central axis until a hypervelocity jet is formed [6], as shown in Figure 2-2 [10]. A second, slower jet where the majority of a conical liners mass is located [9], is also formed. This is referred to as the 'slug.'

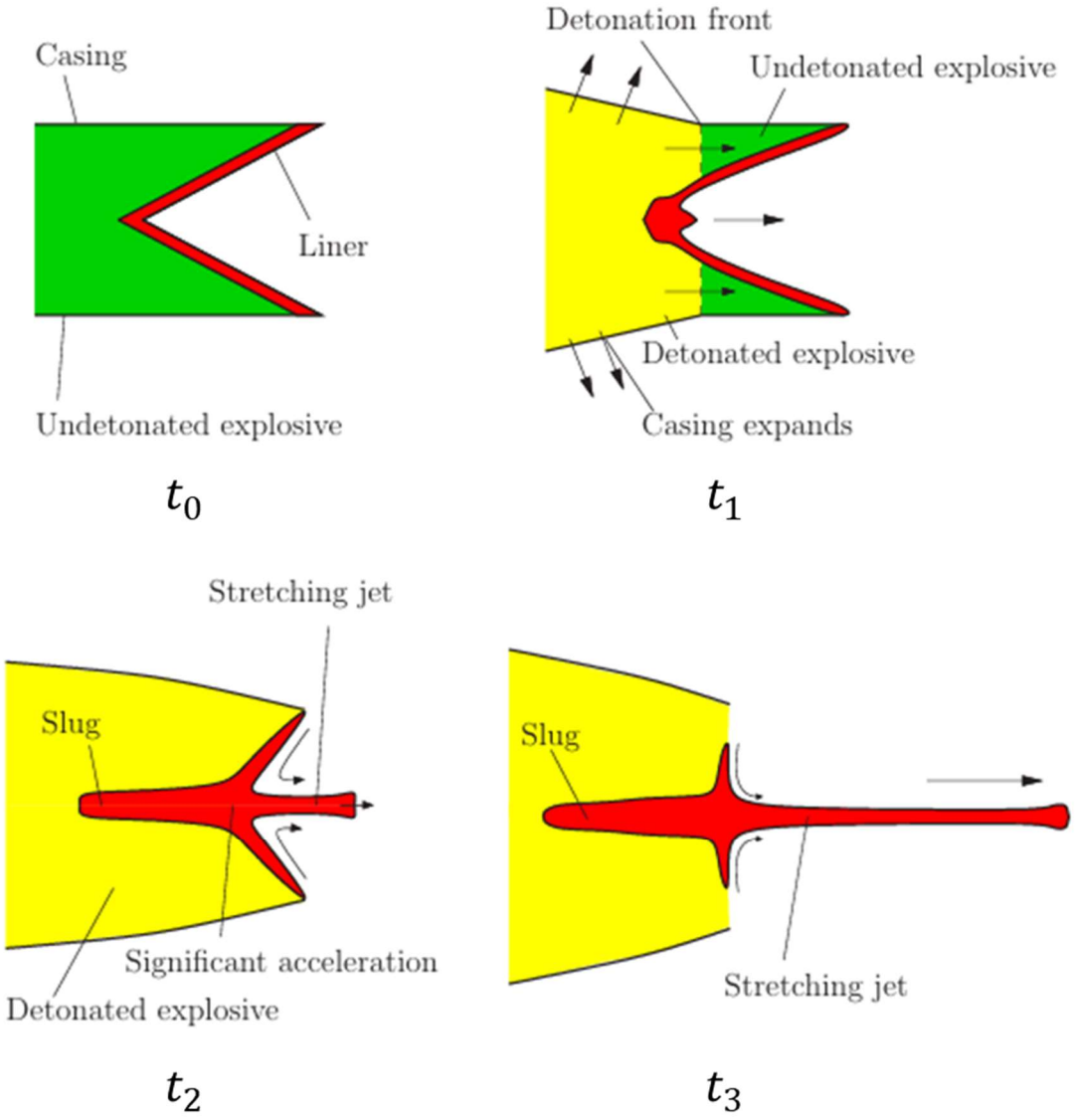


Figure 2-2 – Liner Collapse of a Shaped Charge Highlighting the Detonation Wave Propagation, and Jet Formation [10]

2.2 Stand-off Distance

The standoff distance is the distance between the base of a shaped charge and its intended target, illustrated in Figure 2-3 [1]. It is an important consideration in shape charge design as it significantly affects the penetration capability of the jet [2, 4, 9].

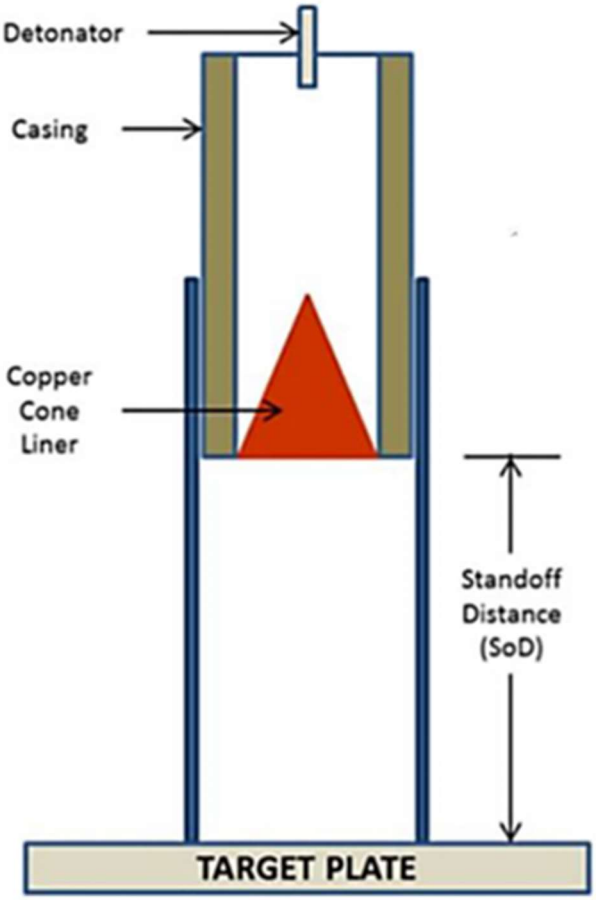


Figure 2-3 - Schematic of the Standoff Distance for a Shaped Charge [1]

A jet is not formed instantaneously and takes a set distance and time to stretch and form. If the distance is too short, the jet would not be fully established, and the penetration capability would be reduced. If the distance is too large there is a possibility that the jet would continue to stretch, eventually leading to particulation and break up, or resulting in the loss of its penetration capability [2, 3, 11]

The optimum distance is typically 2-8 times the cone diameter of the shaped charge [11] allowing the jet sufficient time to form while maximizing the penetrative effect [2, 4].

3 Design Parameters of Military Shaped Charges

The primary objective of a Military shaped charge is to achieve maximum penetration, with the design and material properties selected based on the desired application.

The liner is the most critical element [4] as the shape and size affects the jet formation and the penetrative power. For example, shaped charges with a apex angle of less than 100° [1, 4], illustrated in Figure 3-1a [4], produce high velocity jets capable of deep penetration [11]; whereas, hemispherical liners, as in Figure 3-1b [4], produce wider jets with a lower tip velocity for larger craters [11].

The diameter of the liner directly relates to the jet's length and penetration potential [4], with a larger liner producing a larger jet with enhanced penetration power. The wall thickness of the liner is typically between 1-4% of the diameter [4], however this depends on the shape, material and desired characteristics. A thicker liner will have a greater mass, providing more penetration capability but will have a shorter break up time.

The explosive material is another key consideration, with military designs prioritising materials with high detonation velocities and high pressures to maximise the energy imparted on the liner during its collapse. Composition B, HMX, RDX and Octol are commonly used [1, 4].

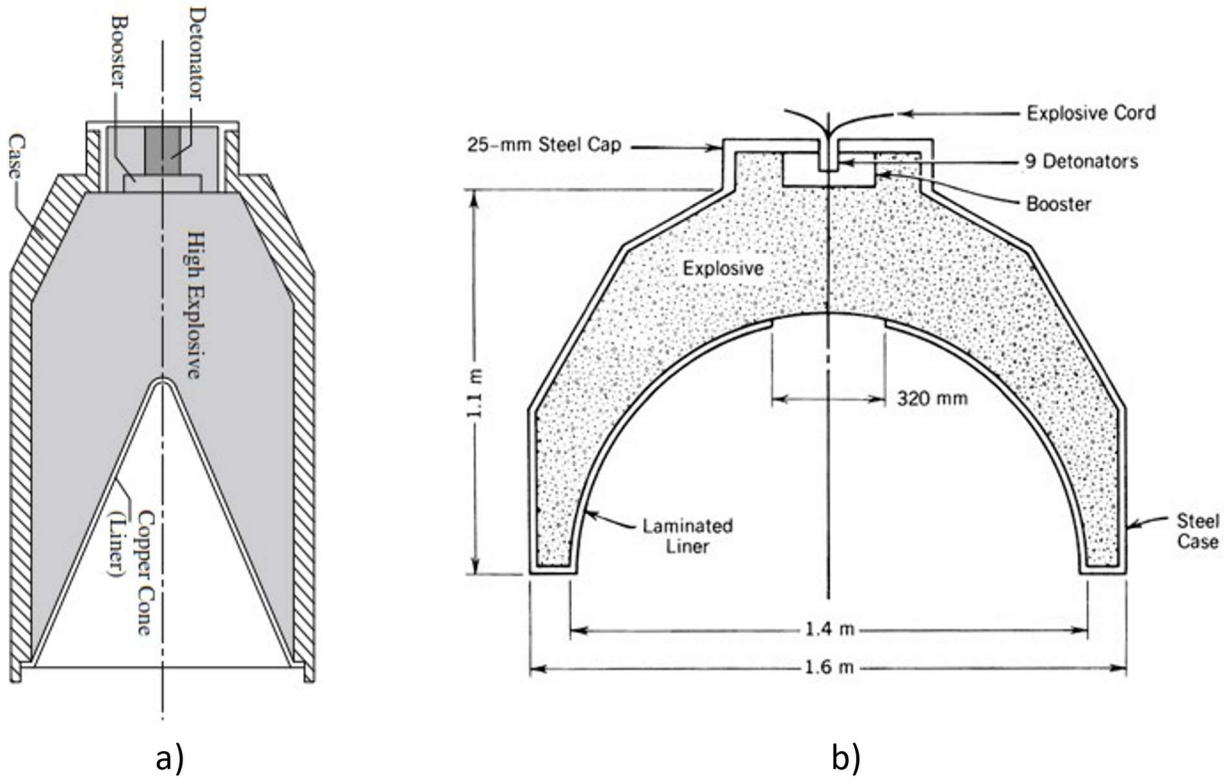


Figure 3-1 –Designs of Shaped Charges Showing a) A Small Apex Conical Shaped Charge and b) A Hemispherical Shape Charge Design [4]

4 Modelling Shaped Charges

4.1 Finite Element Analysis

Finite Element Analysis (FEA) enables the analysis of the performance of shaped charges to aid with design optimisation. FEA is the computational simulation of a physical component by dividing large systems into smaller parts called finite elements, also known as a mesh. A mesh typically consists of triangles or quadrilaterals in 2D and tetrahedra or hexahedra in 3D, depending on the desired analysis. This is illustrated in Figure 4-1 which shows a basic 2D shape. The interconnecting points are called nodes, and their behaviour is determined by a mathematical technique called the Finite Element Method (FEM) [12]. Utilising this concept, FEA predicts how an entire system will respond under different conditions.

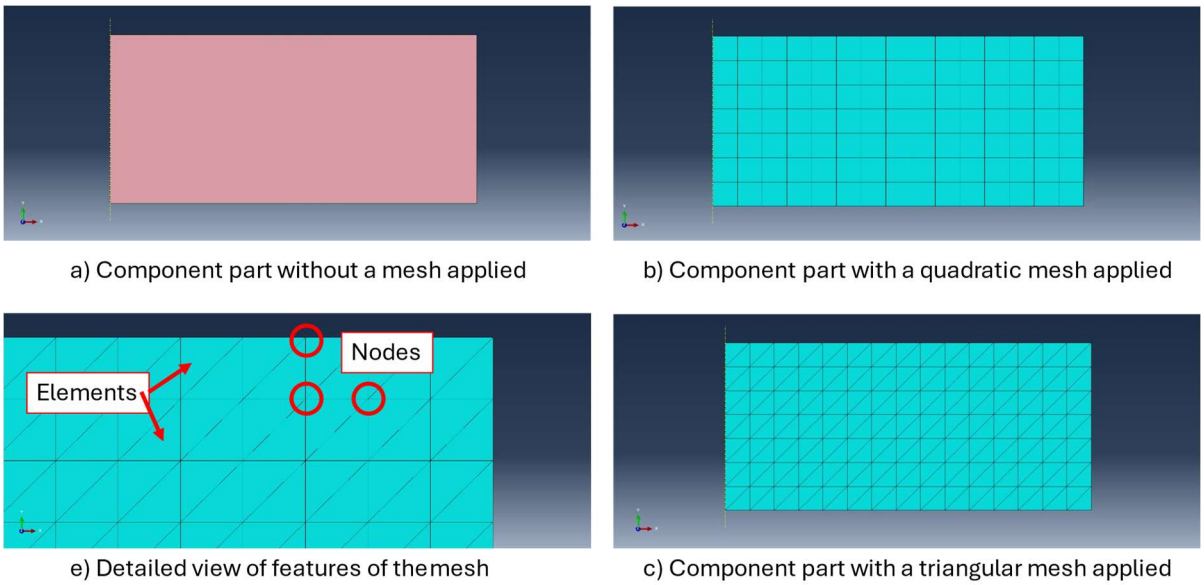


Figure 4-1 - Simple Representation of 2D Meshing in Finite Element Analysis

In the analysis of shaped charges, FEA can simulate the detonation process and the resulting high-velocity jet, to provide an insight on the jet's velocity, shape, and penetration performance. The process involves:

1. Creating a detailed mesh of the shaped charge.
2. Defining the material properties of the components; including the density and strength of the material.
3. Assigning the boundary conditions and constraints.
4. Running the simulation to enable analysis of the jet formation.

4.2 Material Models and Equations of State

The material properties assigned to components during FEA are crucial for a successful calculation as they determine how a component will behave during a simulation. Consideration should also be given to using the appropriate material model and Equation of State (EOS). The models and EOS used in this report are:

- Johnson-Cook (JC) Material Model

- Jones-Wilkins-Lee (JWL) Equation of State
- Mie–Grüneisen Equation of State

4.2.1 Johnson Cook (JC) Material Model

The Johnson-Cook (JC) material model is used to predict the flow behaviours, high strain rates, and deformation of materials, while material damage is forecasted with the JC failure model. Stress and strain interactions are represented in the model [13] with the flow stress equation shown in 4-1.

$$\sigma = (A + B\varepsilon^{n})(1 + C\ln\dot{\varepsilon}^{*})(1 - T^{*m}) \qquad 4\text{-}1$$

Where:

σ is the equivalent stress

ε is the equivalent strain

$\dot{\varepsilon}^{*}$ is the dimensionless strain rate

$T^{*}$is the homologous temperature

A, B, C, m are the Johnston-Cook material constants

4.2.2 Jones-Wilkins-Lee (JWL) Equation of State

The JWL EOS is widely used to describe the relationship between pressure, temperature and volume of detonation products from explosive materials [14]. It is essential for determining how explosives interact with surrounding materials. It is commonly expressed with pressure as the subject [14] as presented in 4-2.

$$P = A\left(1 - \frac{\omega}{R_1 V}\right)e^{-R_1 V} + B\left(1 - \frac{\omega}{R_2 V}\right)e^{-R_2 V} + \frac{\omega E}{V} \qquad 4\text{-}2$$

Where:

P is the pressure

V is the specific volume

E is the internal energy

A, B, R_1, R_2, ω are material constants

4.2.3 Mie–Grüneisen Equation of State

The Mie–Grüneisen EOS relates the pressure, volume and internal energy of a solid under shock compression, where pressure is a linear function of internal energy [15]. The EOS is crucial for modelling materials in high pressure environments as seen in shaped charges. It can be expressed as:

$$P - P_0 = \frac{\Gamma}{V}(e - e_0) \qquad 4\text{-}3$$

Where:

P is the pressure

V is the volume

e is the internal energy

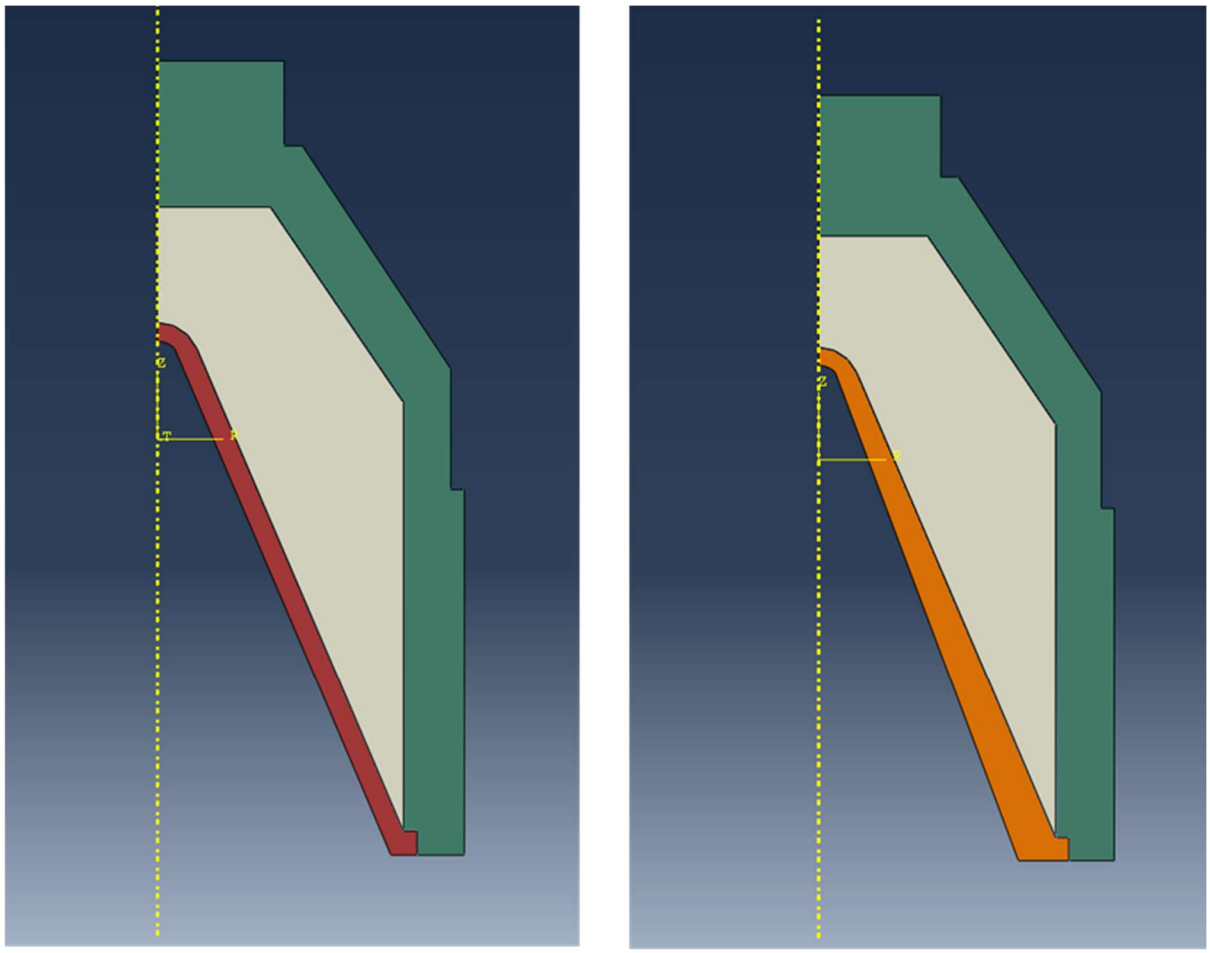
Γ is the Grüneisen parameter

5 Design of The Model and Analysis Parameters

This report studies how variation in the shaped charge design affects the jet formation and its overall penetration capability. The primary focus is on how a liner with gradual thickness compares with a liner of constant thickness. The computer simulation software ABAQUS in standard/explicit mode was used to model the jet formation.

5.1 The 2D Design

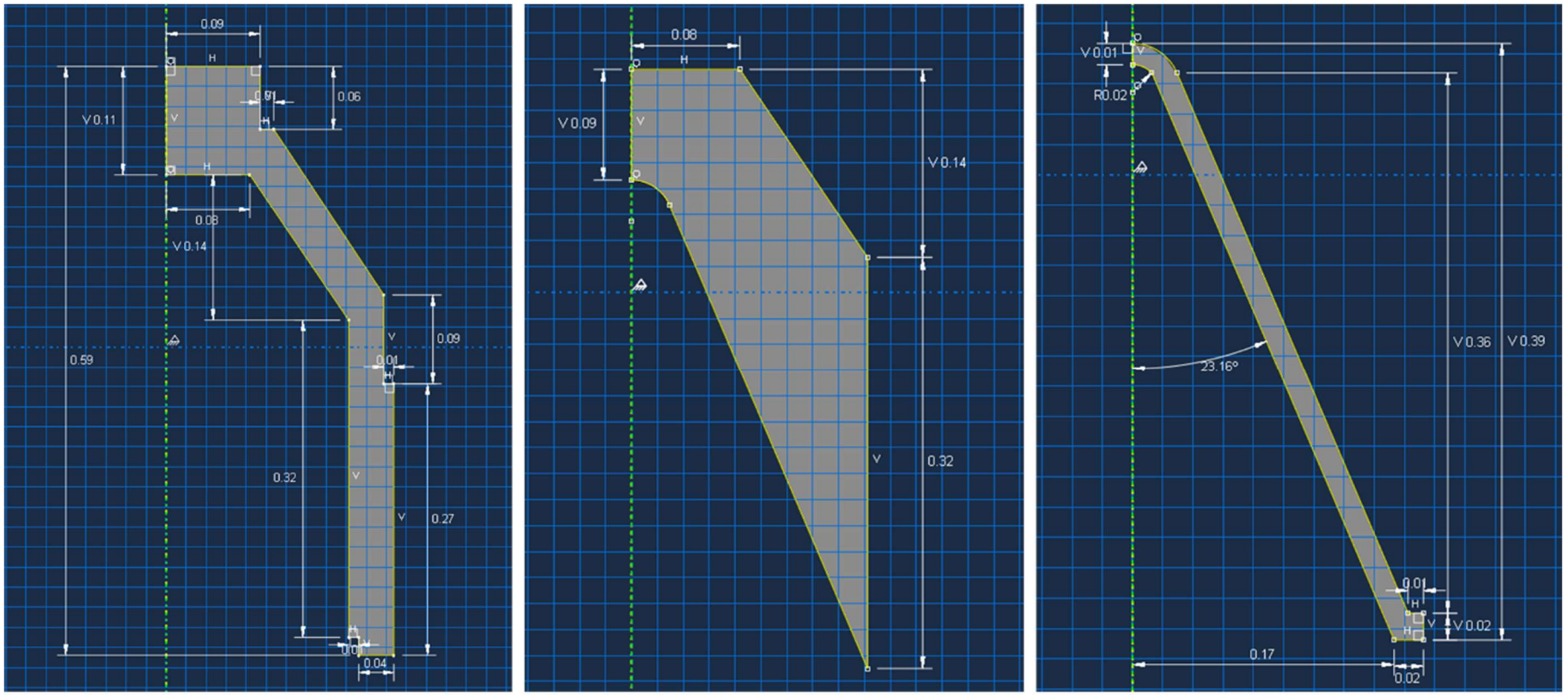
The design was based on the generic shaped charge shown in Figure 2-1. Initially it was drawn in 2D as a symmetrical shape comprised of three components: the casing, the explosive and the liner. Figure 5-1a shows Design One with a constant thickness liner of 0.02m, with Figure 5-1b showcasing Design Two with a gradual thickness liner of 0.02m at the apex, increasing to 0.03m at the base. The corresponding sketched are shown in Figure 5-2 and Figure 5-3 respectively.



a) Design 1 – Constant Liner

b) Design 2 – Variable Liner

Figure 5-1 - Assembled 2D Symmetrical Designs

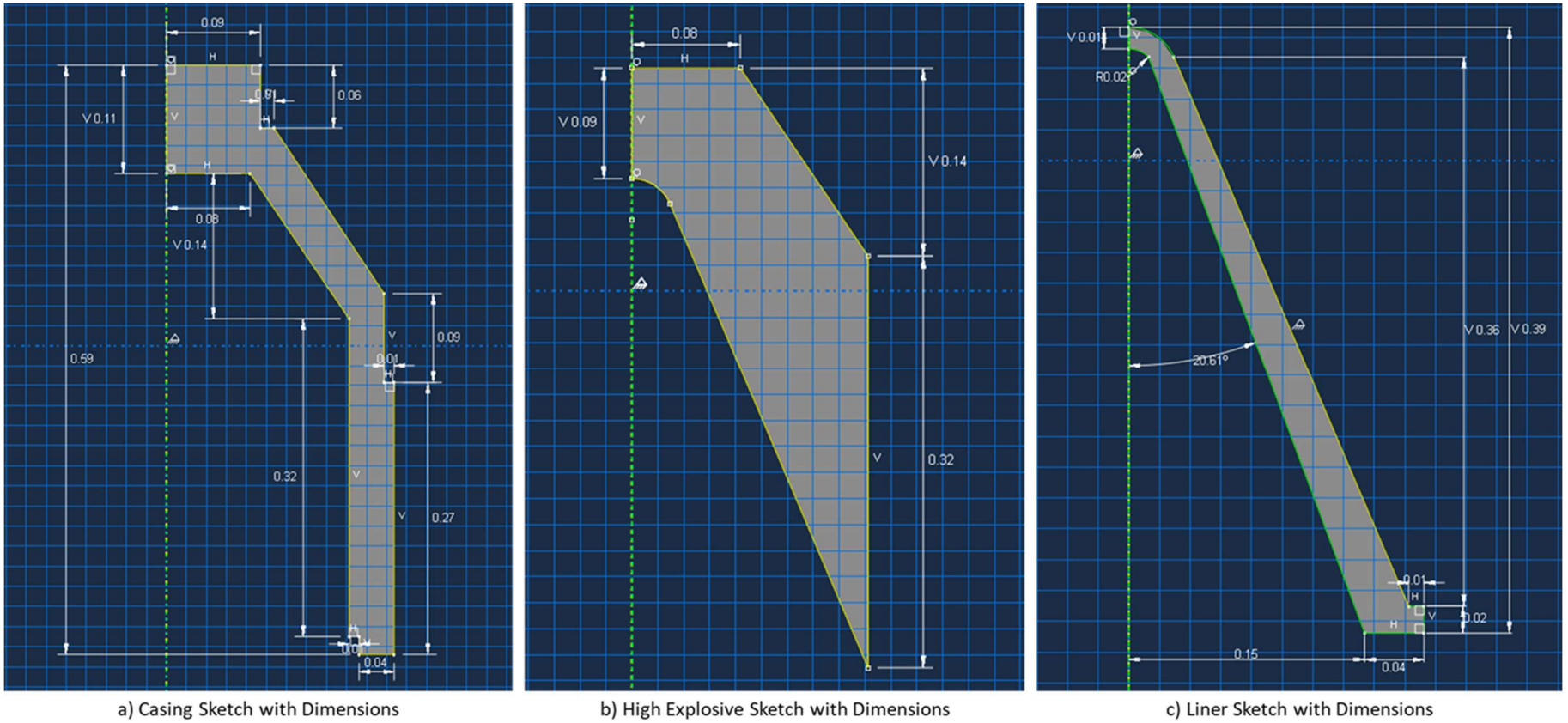


a) Casing Sketch with Dimensions

b) High Explosive Sketch with Dimensions

c) Liner Sketch with Dimensions

Figure 5-2 - Design One Individual Component Detailed Sketches of a) The Casing, b) The High Explosive and c) The Liner. All Dimensions Shown in Meters.



a) Casing Sketch with Dimensions

b) High Explosive Sketch with Dimensions

c) Liner Sketch with Dimensions

Figure 5-3 - Design Two Individual Component Detailed Sketches of a) The Casing, b) The High Explosive and c) The Liner

To aid with the analysis of the two designs, the shaped charge was directed above a rectangular target, with a stand-off distance of 1m. The dimensions of the target are presented in Figure 5-4.

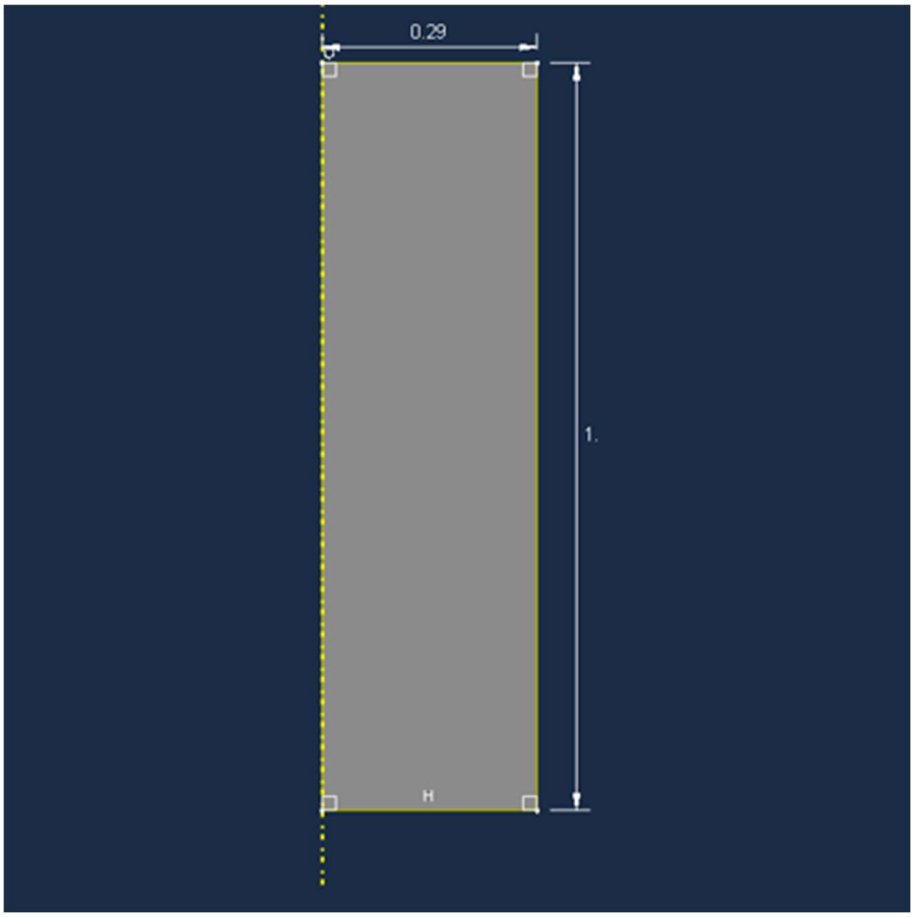
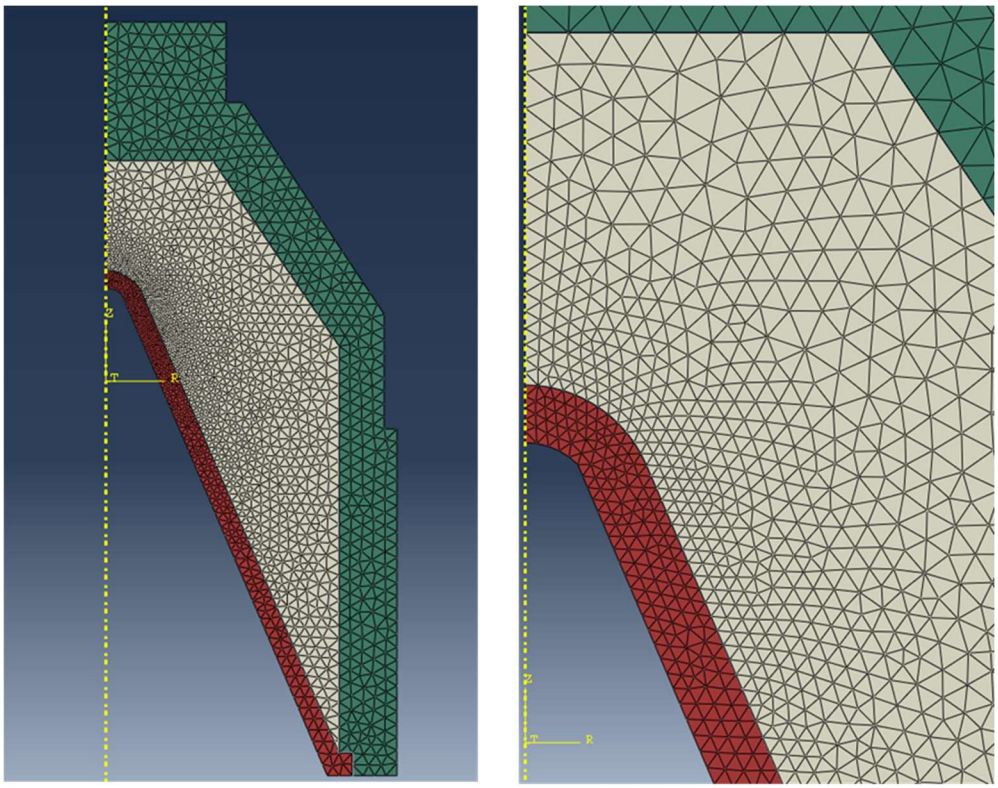


Figure 5-4 - Target Sketch with Dimensions

5.1.1 The 2D Mesh

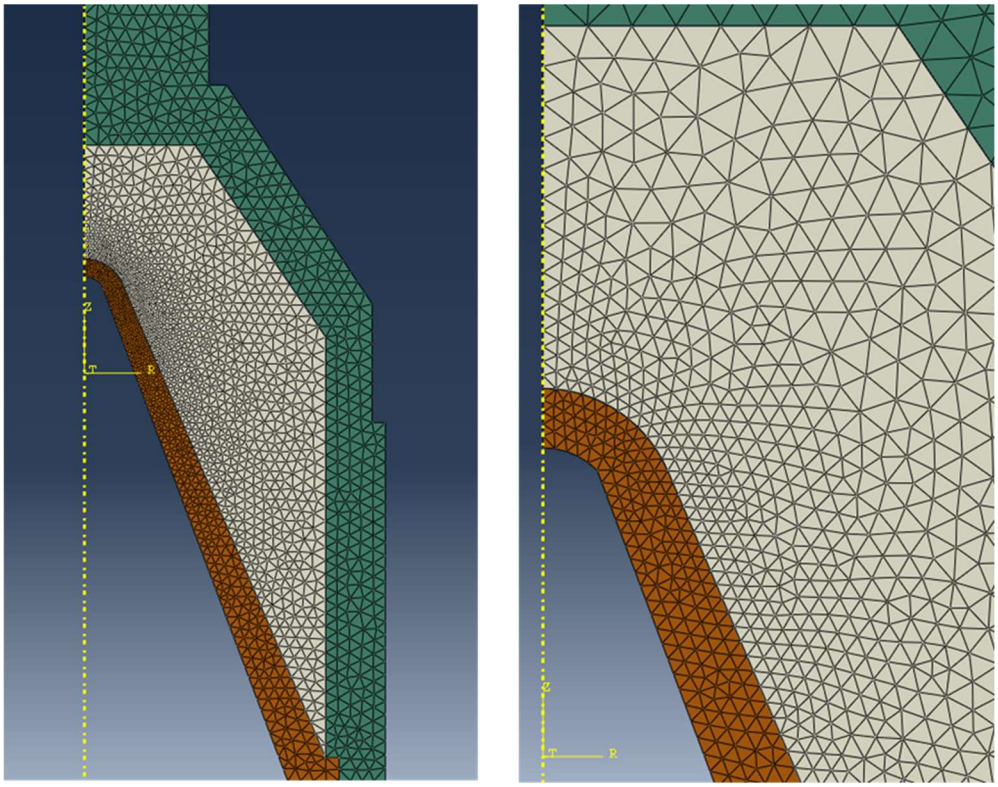
As discussed in Section 4, the attributed of the mesh for each component is crucial for Finite Element Analysis (FEA). The 2D mesh for each design can be seen in Figure 5-5 and Figure 5-6.

Due to the complexity and shape of the designs these meshes are formed of triangular elements. In this instance, the use of a quadratic mesh would not be appropriate due to the curvature of the design. With the focus of the analysis being on the formation of the jet, which is produced from the liner, a finer mesh is used at its apex. This allows a more detailed analysis to be undertaken during the liner collapse. To provide an accurate simulation, the mesh is graduated with an increasing density from the apex to the casing.



a) Design 1 - Assembled Mesh b) Design 1 – Detailed View of Mesh

Figure 5-5 - Design One Assembled 2D Mesh



a) Design 2 - Assembled Mesh b) Design 2– Detailed View of Mesh

Figure 5-6 - Design Two Assembled 2D Mesh

The mesh for the target is illustrated in Figure 5-7. As the jet formation occurs along the central axis of a shaped charge, a denser mesh was applied along the centre of the target, increasing in size towards the external edge of the shape.

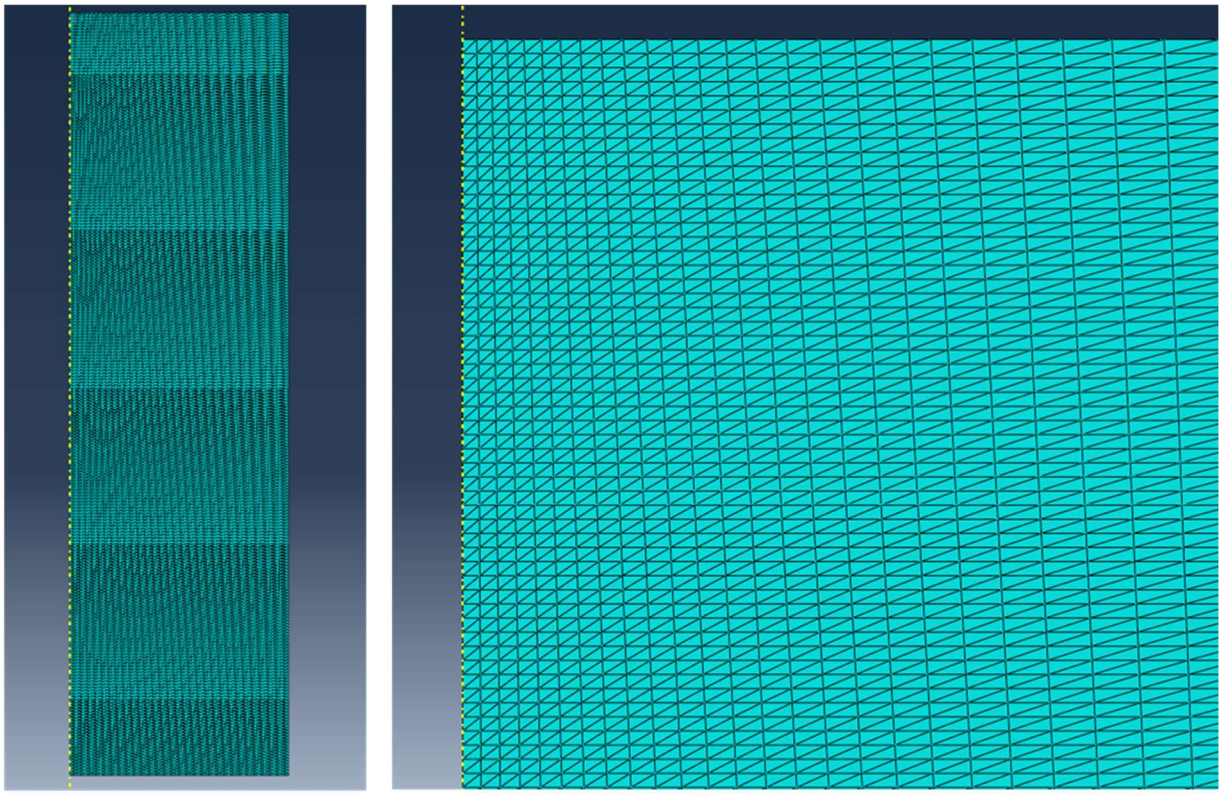


Figure 5-7 - Target 2D Mesh

5.2 Material Properties

The material properties allocated were chosen for their performance characteristics and application in current in-service Military shaped charges.

The materials with the appropriate material model and EOS used for each component are listed in Table 5-1**Error! Not a valid bookmark self-reference.**, with the parameters used for each model listed in Table 5-2-Table 5-4 [9, 14, 16, 17, 18, 19, 20, 21]

Table 5-1 – Material Models and EOS Used in Models

COMPONENT	MATERIAL	MATERIAL MODELS AND EOS
Casing	AISI 1045 Steel	Johnston Cook Plastic Model
High explosive	Composition B	JWL EOS
Liner	OFHC Copper	Johnston Cook Plastic Model
		Mie- Grüneisen EOS
Target	AISI 1045 Steel	Johnson Cook Plastic Model
		Johnson Cook Damage Model
		Mie- Grüneisen EOS

Table 5-2 - AISI 1045 Steel Material Properties [9, 16, 17, 18]

Material properties	**Symbol**	**AISI 1045 Steel**
Density	ρ (kgm^{-3})	7850
Young's modulus	E (GPa)	210
Poisson's ratio	v	0.3
Johnston Cook Plastic		
Material properties	**Symbol**	**AISI 1045 Steel**
JC yield strength	A (MPa)	553
JC hardening coefficient	B (MPa)	600
JC strain hardening exponent	N	0.234
JC strain rate constant	C	0.013
JC softening exponent	M	1
Melting temperature	Tm (K)	1733
Transition temperature	T (K)	293
Reference Strain Rate	ε_0	1
Johnston Cook (JC) Damage		
Material properties	**Symbol**	**AISI 1045 Steel**
JC damage constant	d1	0.05
JC damage constant	d2	4.22
JC damage constant	d3	-2.73
JC damage constant	d4	0.0018
JC damage constant	d5	0.55
Melting temperature	Tm (K)	1733
Transition temperature	T (K)	293

Table 5-3 - OFHC Copper Material Properties [19, 20]

Material properties	Symbol	OFHC Copper
Density	ρ (kgm^{-3})	3930
Shear modulus	G (GPa)	45
Johnston Cook Plastic		
Material properties	**Symbol**	**OFHC Copper**
JC yield strength	A (MPa)	89.7
JC hardening coefficient	B (MPa)	292
JC strain hardening exponent	N	0.31
JC strain rate constant	C	0.025
JC softening exponent	M	1.09
Melting temperature	Tm (K)	1381
Transition temperature	T (K)	293
Reference Strain Rate	ε_0	1
Mie–Grüneisen Equation of State		
Material properties	**Symbol**	**OFHC Copper**
Shock Velocity	c_0	3940
Slope Shock Velocity Coefficient	S_1	1.489
Grüneisen coefficient	Γ_0	1.99

Table 5-4 - Comp B Material Properties [14, 21]

Jones-Wilkins-Lee (JWL) Equation of State		
Material properties	**Symbol**	**Comp B**
Density	ρ (kgm^{-3})	1717
Velocity of Detonation	D (ms^{-1})	7980
JWL Constant	A (MPa)	554.79
JWL Constant	B (MPa)	30.73
JWL Constant	R_1	4.53
JWL Constant	R_2	1.98
JWL Constant	ω	0.32
Pre-Detonation Bulk Modulus	K (GPa)	4.3437
Detonation Energy Density	(Jm^{-3})	$8.525x10^6$

6 2D Simulation

The simulations of the two designs were set up to run for $1x10^{-3}$s with an output of 500 frames, to enable a detailed analysis of the liner collapse and jet formation. The simulations were completed with 2D models; however, some results have been presented in a 3D form aid with the analysis.

Initially the simulations were conducted without the metal target to allow analysis on the jet formation. To provide performance comparison between the two designs a second simulation with a metal target was undertaken. Aside from the metal target, the parameters of the simulation were identical. The jet was formed in the same manner, with respect to pressure build up from the explosive material and the compression of the liner during its collapse.

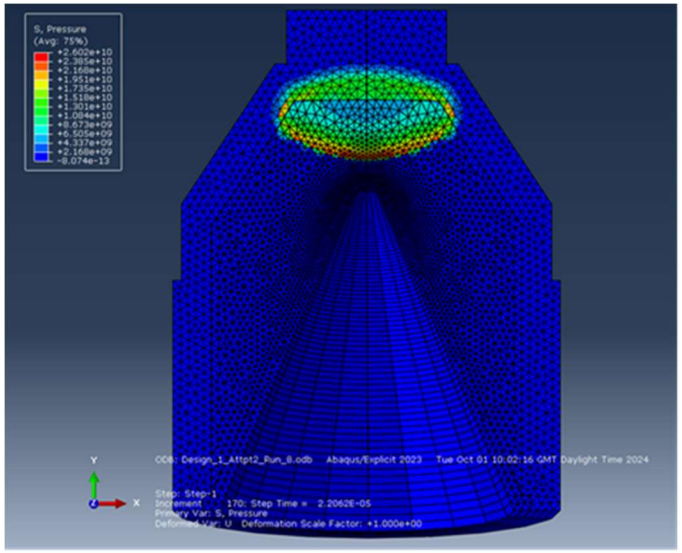
The target had the Johnston Cook Damage model applied to simulate the potential damage from the jet impact, these values are provided in Table 5-3. An equation of state was also applied due to the expected high pressures exerted onto the target. To further support the analysis, and to enable the simulation to run as long as possible, element deletion was also applied to the target mesh. Element deletion would occur when the material fails due to complete loss of load carrying capability and or the loss of material integrity [22].

6.1 Design One Analysis

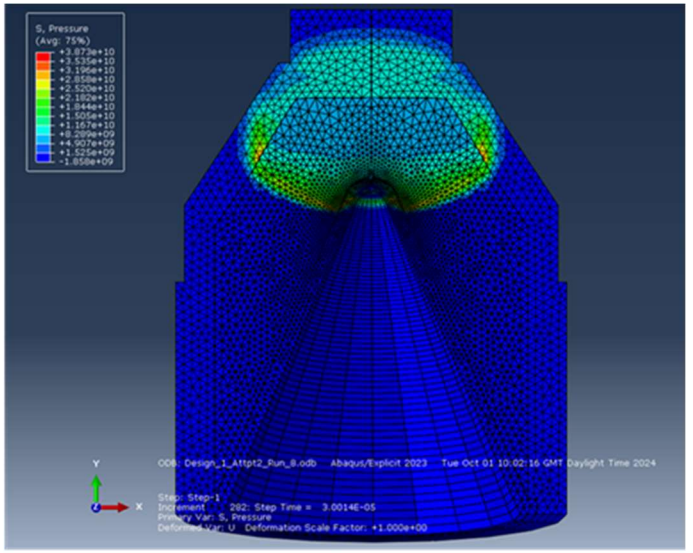
6.1.1 Design One Jet Formation Analysis

Design One's initial simulation (2D_Design_One_Jet_Run) aborted before completion at $3.8977x10^{-4}$s with an output of 194 frames, this was due to one excessively distorted element in the metal casing. This indicates that the elements became distorted to the point they no longer represented a mathematically possible triangular shape causing the simulation to break down [23]. Applying the JC damage parameters for the material and allowing deletion of damaged nodes may have allowed the simulation to run longer. This would not affect the jet formation, as once the detonation wave has progressed through the liner, the casing is not required for the formation of the jet.

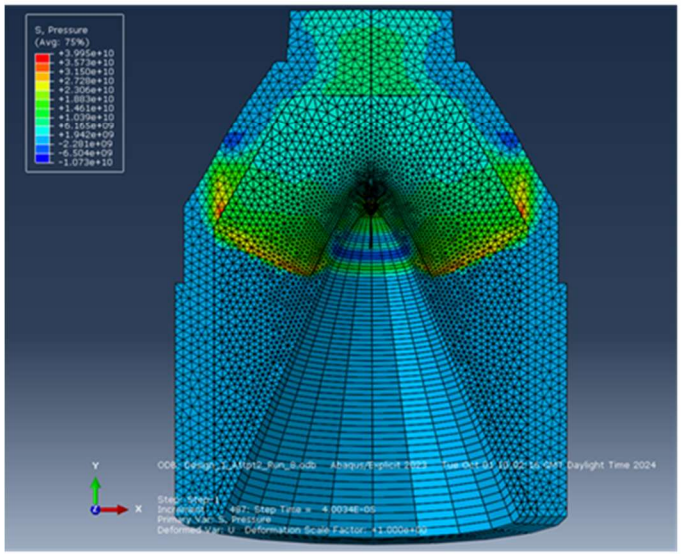
Figure 6-1 shows the progression of the detonation wave through the explosive material and the pressure exerted on the apex of the liner during the start of its collapse. The liner initially collapses from the bottom of the apex where the pressure is in the region of 20 GPa with some elements exceeding 50 GPa; illustrated by the green and red colouring in Figure 6-2 which has the liner isolated to aid analysis. The high pressure is at first targeting the sides of the liner rather than the top, this could be the result of a higher volume of explosive present at the side of the liner compared to the top.



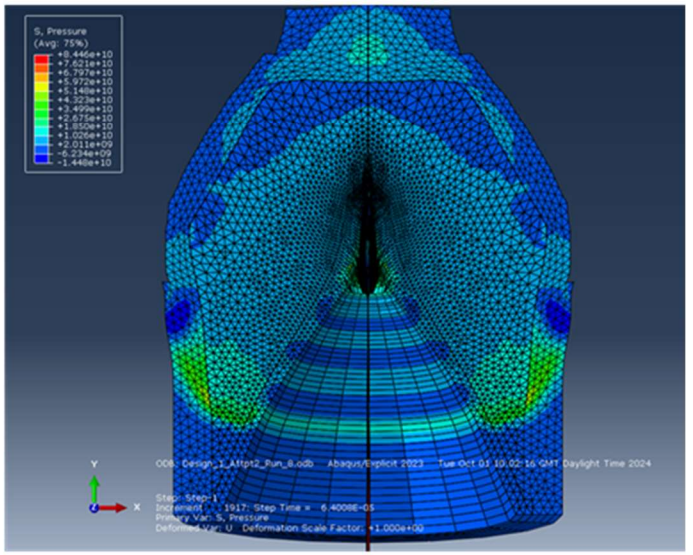
a) Step 11, time = 2.2062×10^{-5}s



b) Step 15, time = 3.0014×10^{-5}s

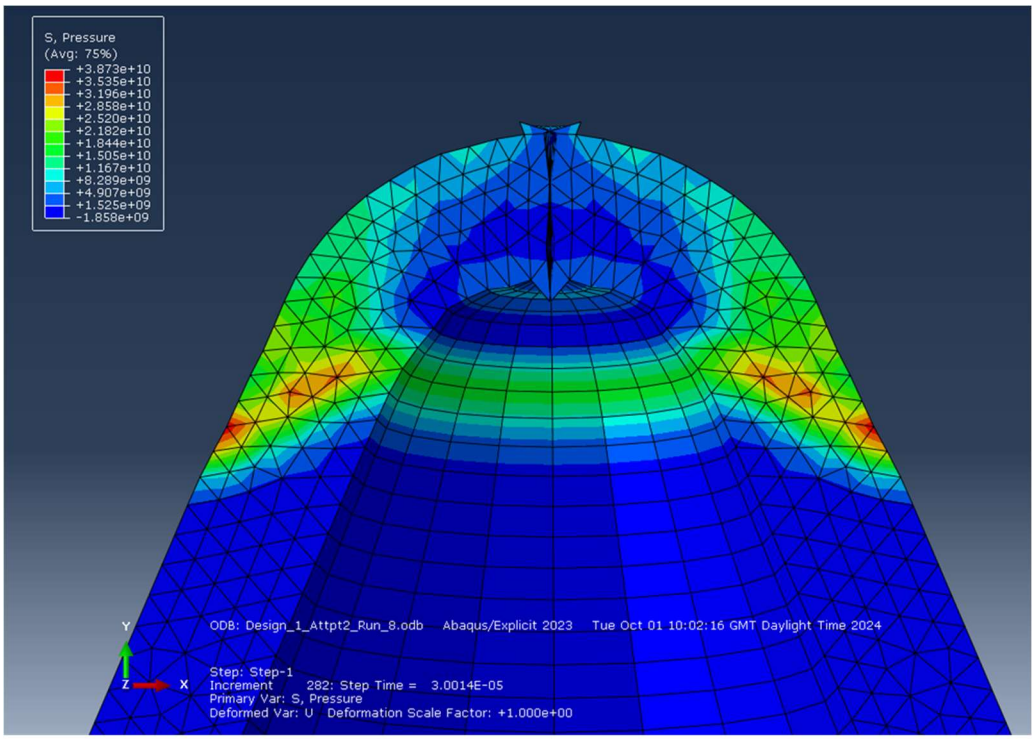


c) Step 20, time = 4.0034×10^{-5}s

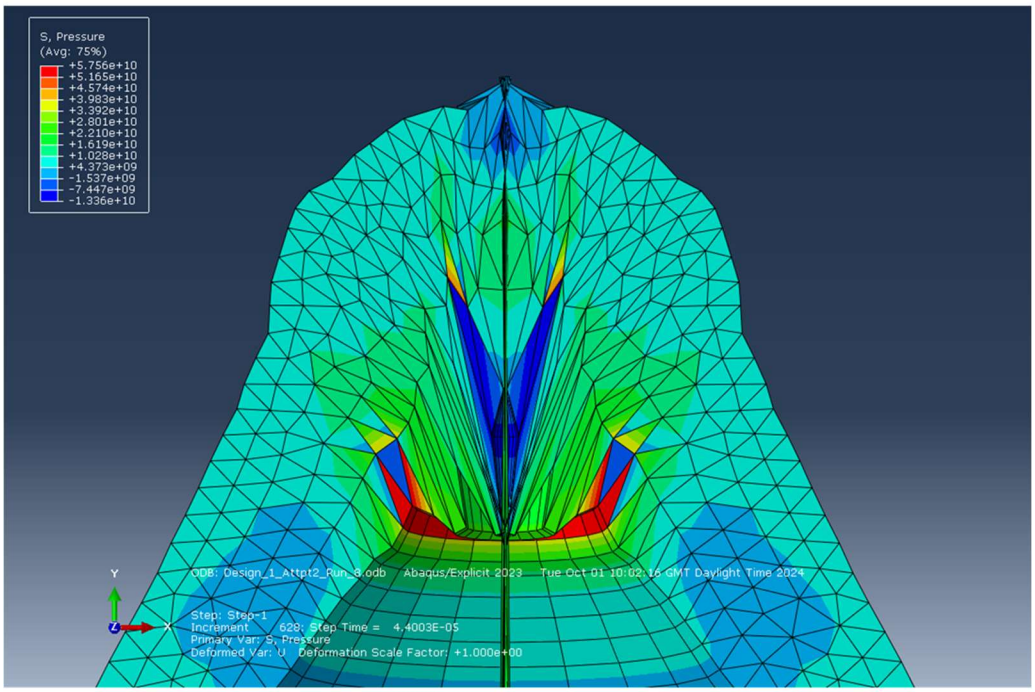


d) Step 32, time = 6.4008×10^{-5}s

Figure 6-1 - 2D_Design_One_Jet_Run Pressure Exerted from the Detonation Wave at a) 2.262×10^{-5}s, b) 3.0014×10^{-5}s, c) 4.0034×10^{-5}s and d) 6.4008×10^{-5}s



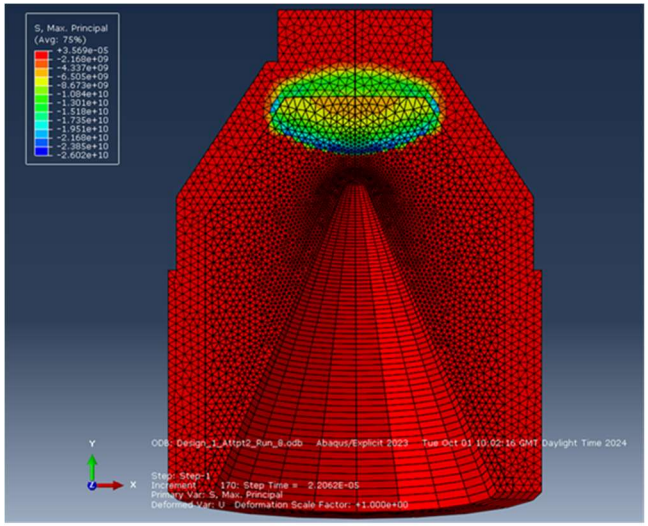
a) Frame 15, time = 3.0014×10^{-5}s



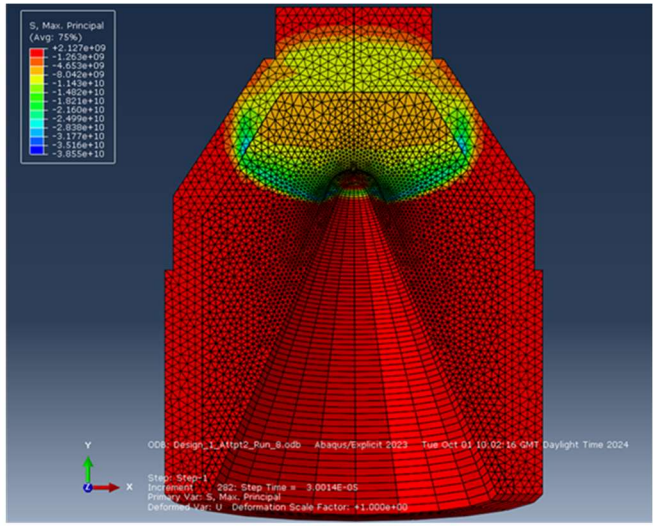
b) Frame 22, time = 4.4003×10^{-5}s

Figure 6-2 – 2D_Design_One_Jet_Run Pressure Exerted on the Apex of the Liner During the Start of the Liner Collapse at a) 3.0014×10^{-5}s and b) 4.4003×10^{-5}s

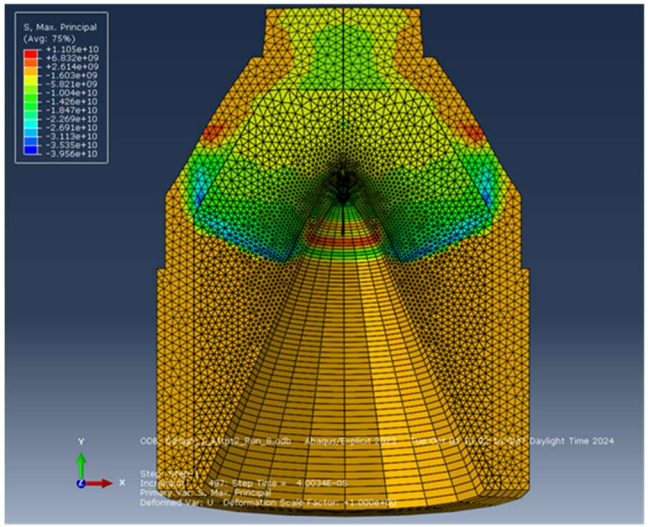
From the results presented in Figure 6-3, it can be seen as the detonation wave progresses through the shaped charge the material in front of the wave is being compressed. This is shown by the blue and green areas representing the negative stress values which indicate compressive stress. As the wave travels past the apex of the liner, it continues to be compressed during the collapse as highlighted in Figure 6-4 by the orange, yellow and green areas.



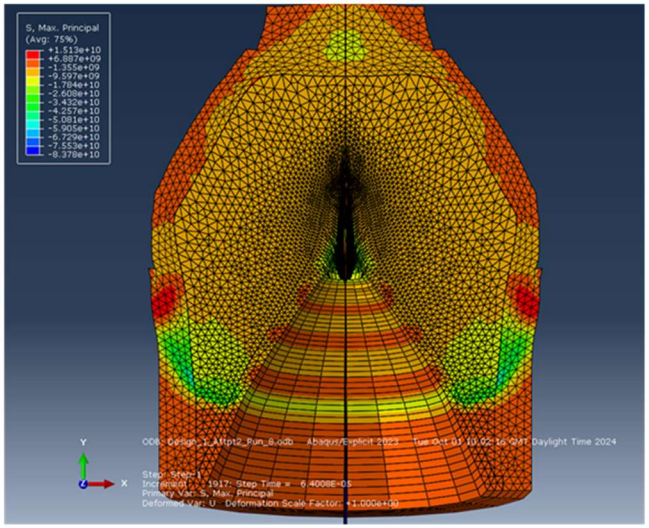
a) Step 11, time = 2.2062×10^{-5}s



b) Step 15, time = 3.0014×10^{-5}s

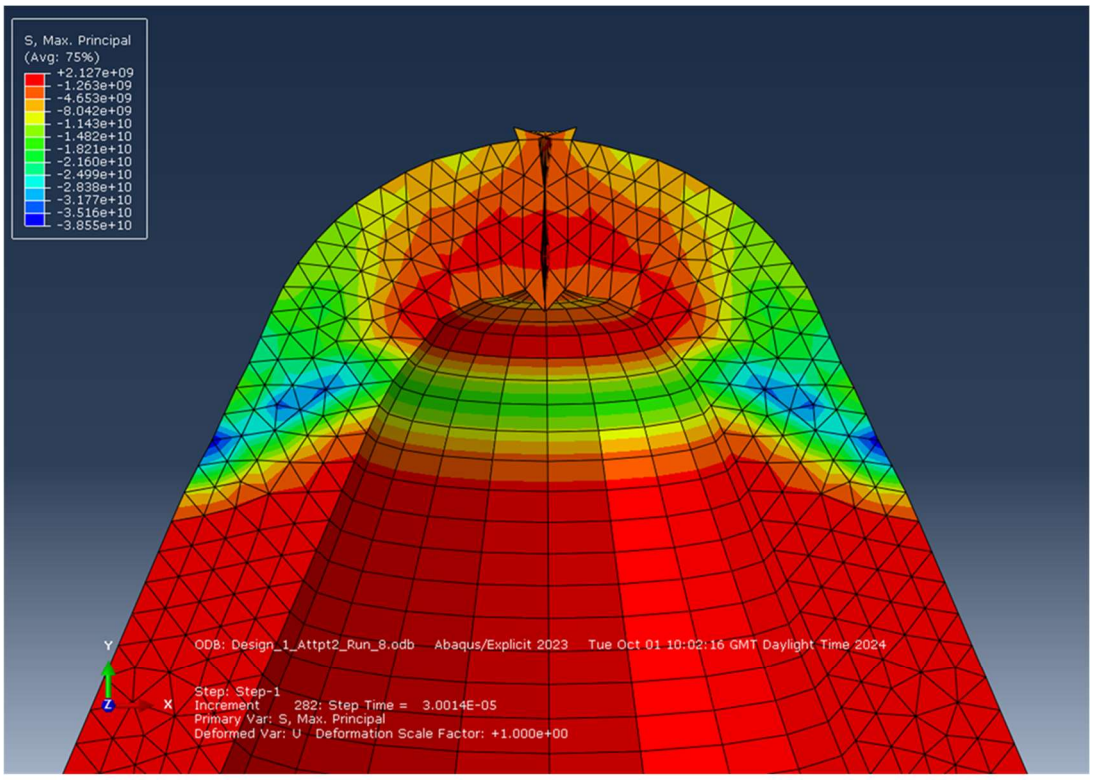


c) Step 20, time = 4.0034×10^{-5}s

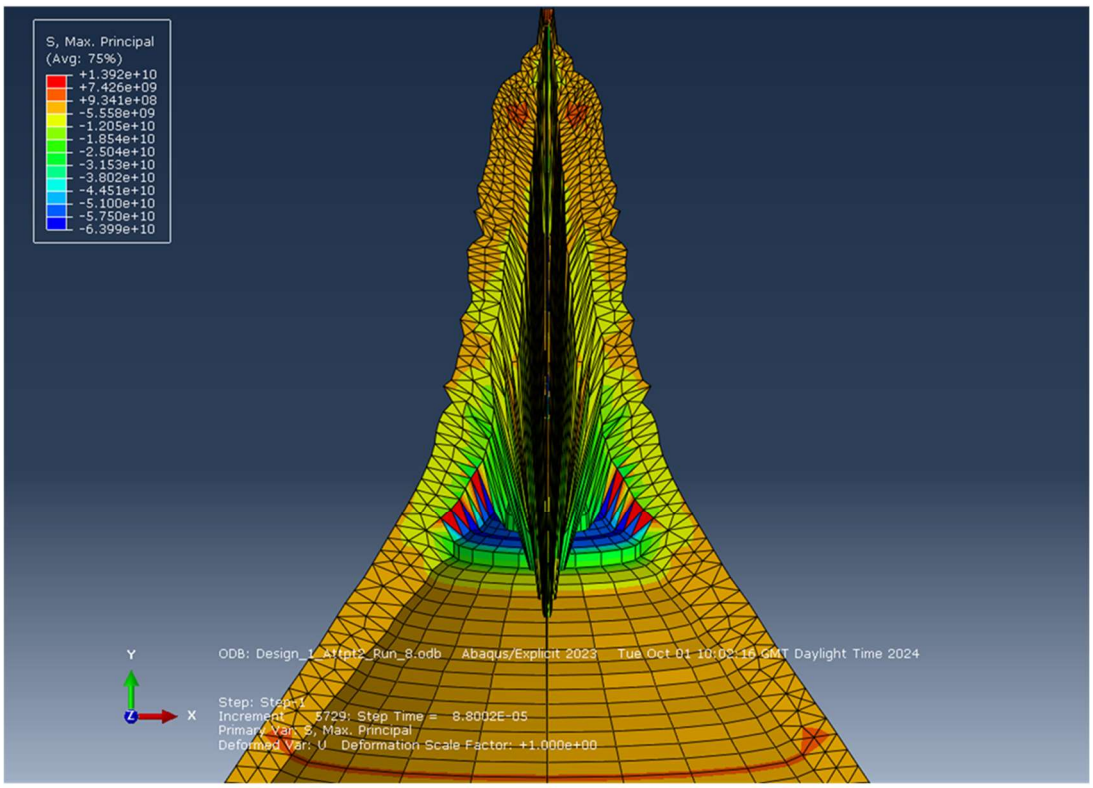


d) Step 32, time = 6.4008×10^{-5}s

Figure 6-3 - 2D_Design_One_Jet_Run Compressive and Tensile Stresses from the Detonation Wave at a) 2.262×10^{-5}s, b) 3.0014×10^{-5}s, c) 4.003×10^{-5}s and d) 6.4008×10^{-5}s



a) Frame 15, time = 3.0014×10^{-5}s



b) Frame 44, time = 8.8002×10^{-5}s

Figure 6-4 - 2D_Design_One_Jet_Run Stress Exerted on the Apex of the Liner During the Start of the Liner Collapse at a) 3.0014x10 $^{-5}$s and b)8.8002x10 $^{-5}$ s

Figure 6-5 illustrates the full jet formation from liner collapse to the simulation aborting. As time progresses the jet is continuously compressed which ends at the point of abortion were the jet is

in the region of 8-9m in length. The full extent of the jet is shown in Figure 6-6, however, as can be seen in Figure 6-7 there is a significant distance between the last two nodes in the jet. It can be hypothesised that the end node (node 34) could be an anomaly in the simulation. If we disregard this node from the analysis, the jet is approximately 2m in length. This jet formation is represented in Figure 6-8, with Figure 6-9 showing the displacement graph of nodes 34 and 164.

How the velocity increased during the jet formation is presented in Figure 6-10. The obscurity in the graph is from node 34 showing an unrealistic velocity of 50kms^{-1}. Figure 6-11 is the velocity graph for the remaining nodes showing an average jet tip velocity of 4kms $^{-1}$.

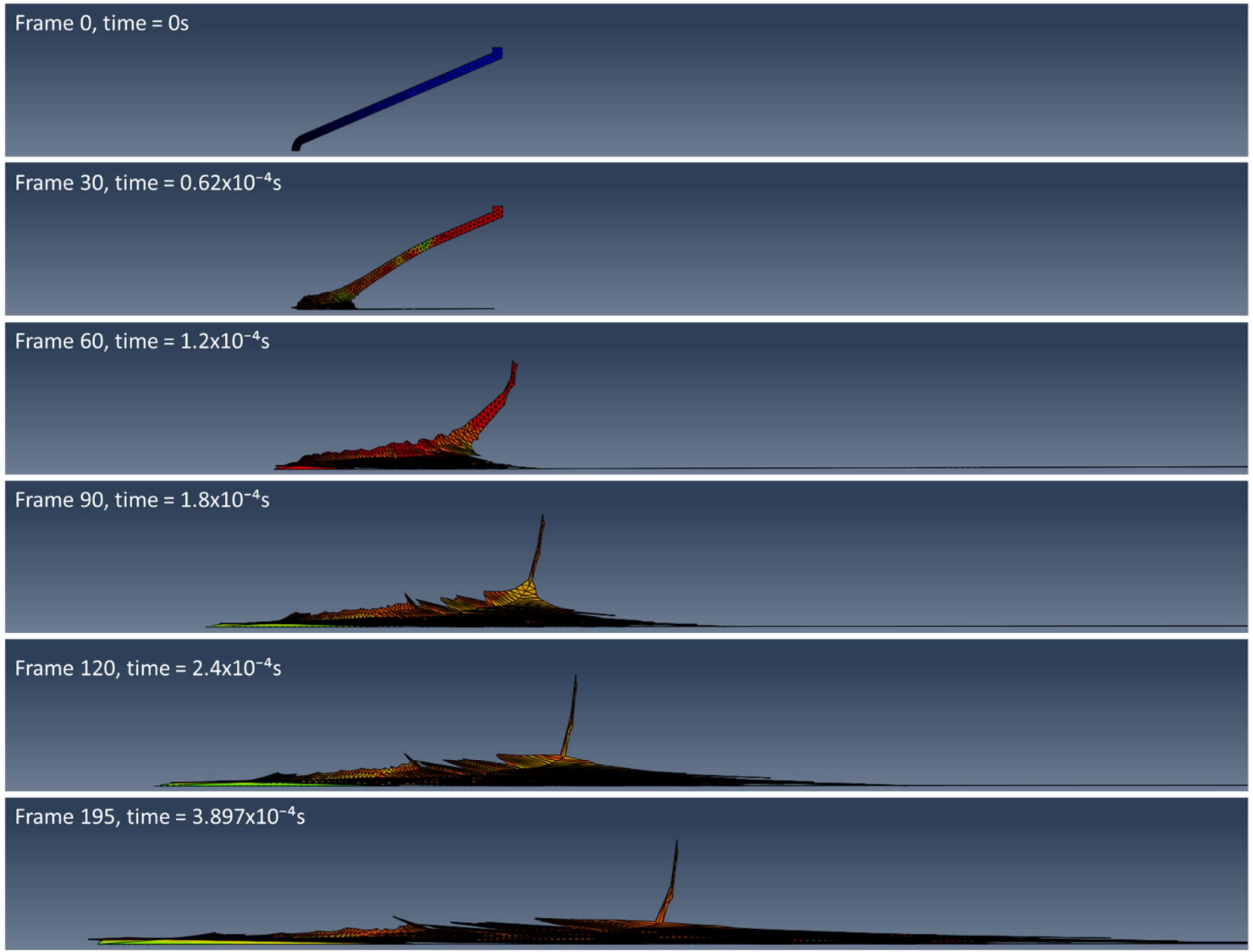


Figure 6-5 - 2D_Design_One_Jet_Run Jet formation from Liner Collapse to Abortion

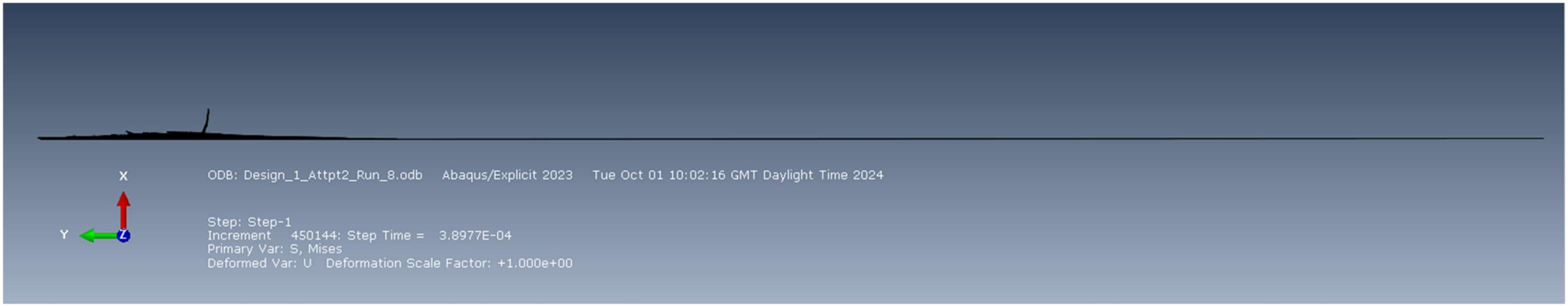


Figure 6-6 - 2D_Design_One_Jet_Run Full Jet at Point of Abortion

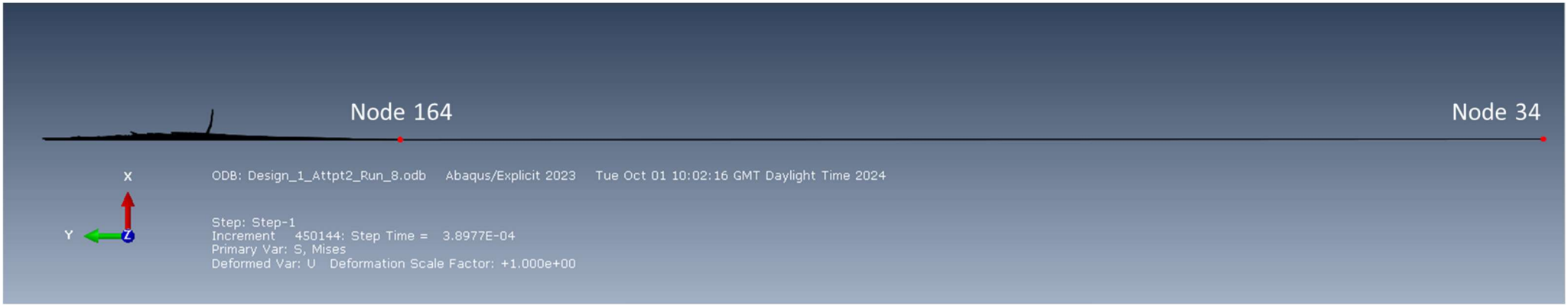


Figure 6-7 - 2D_Design_One_Jet_Run Full Jet at Point of Abortion with End Two Nodes Highlighted

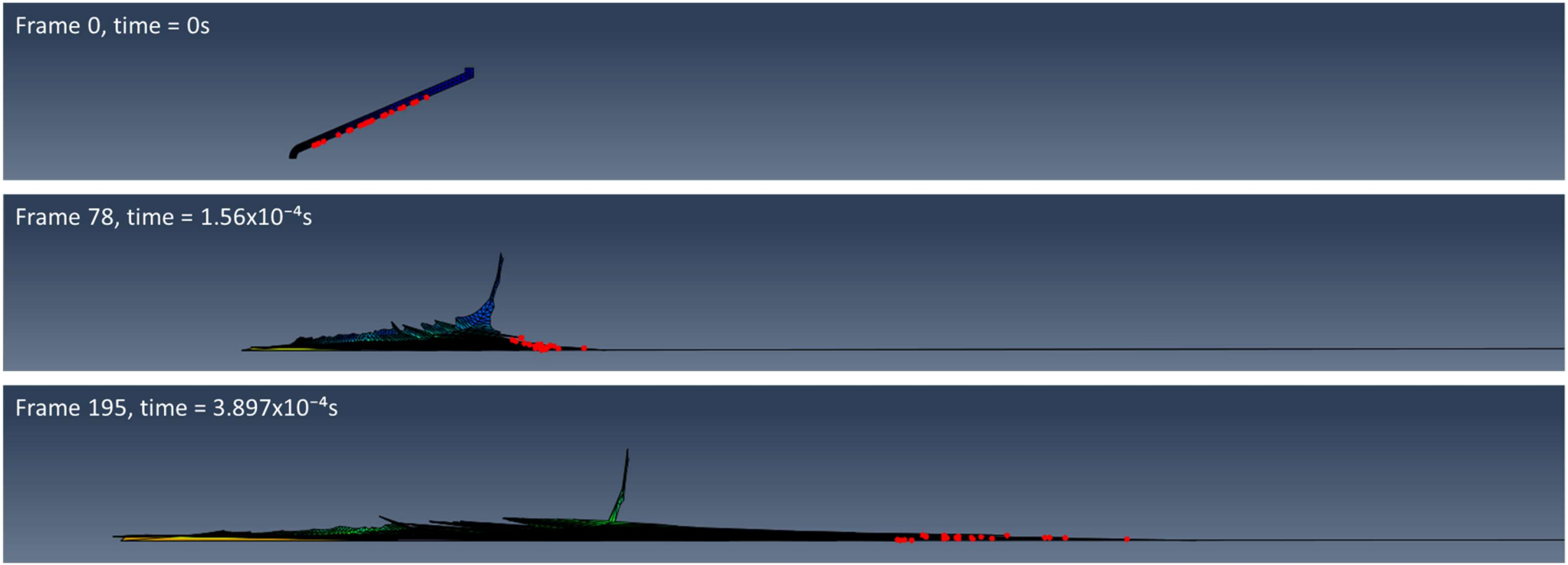


Figure 6-8 - 2D_Design_One_Jet_Run Jet Formation with Realistic Jet Length Highlighted

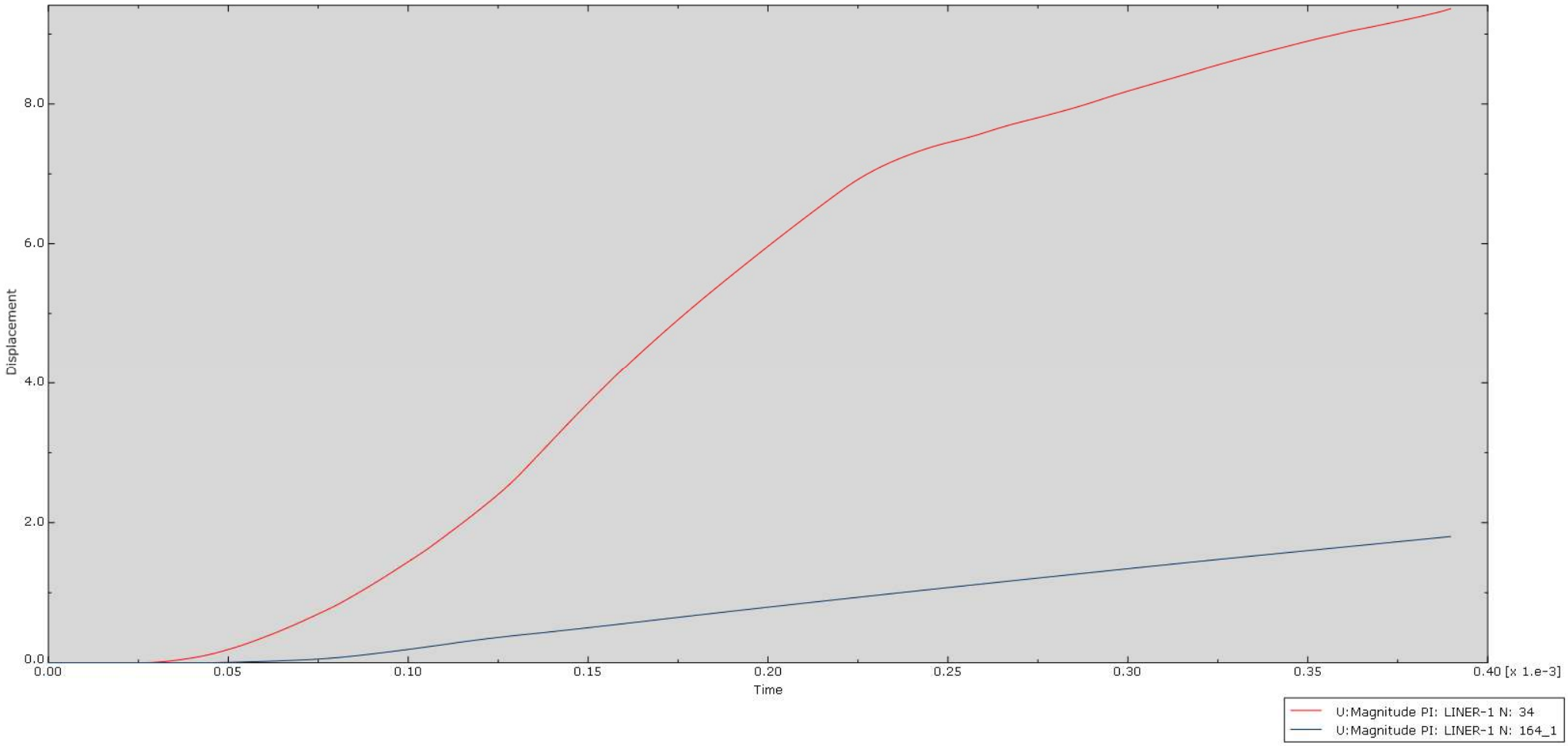
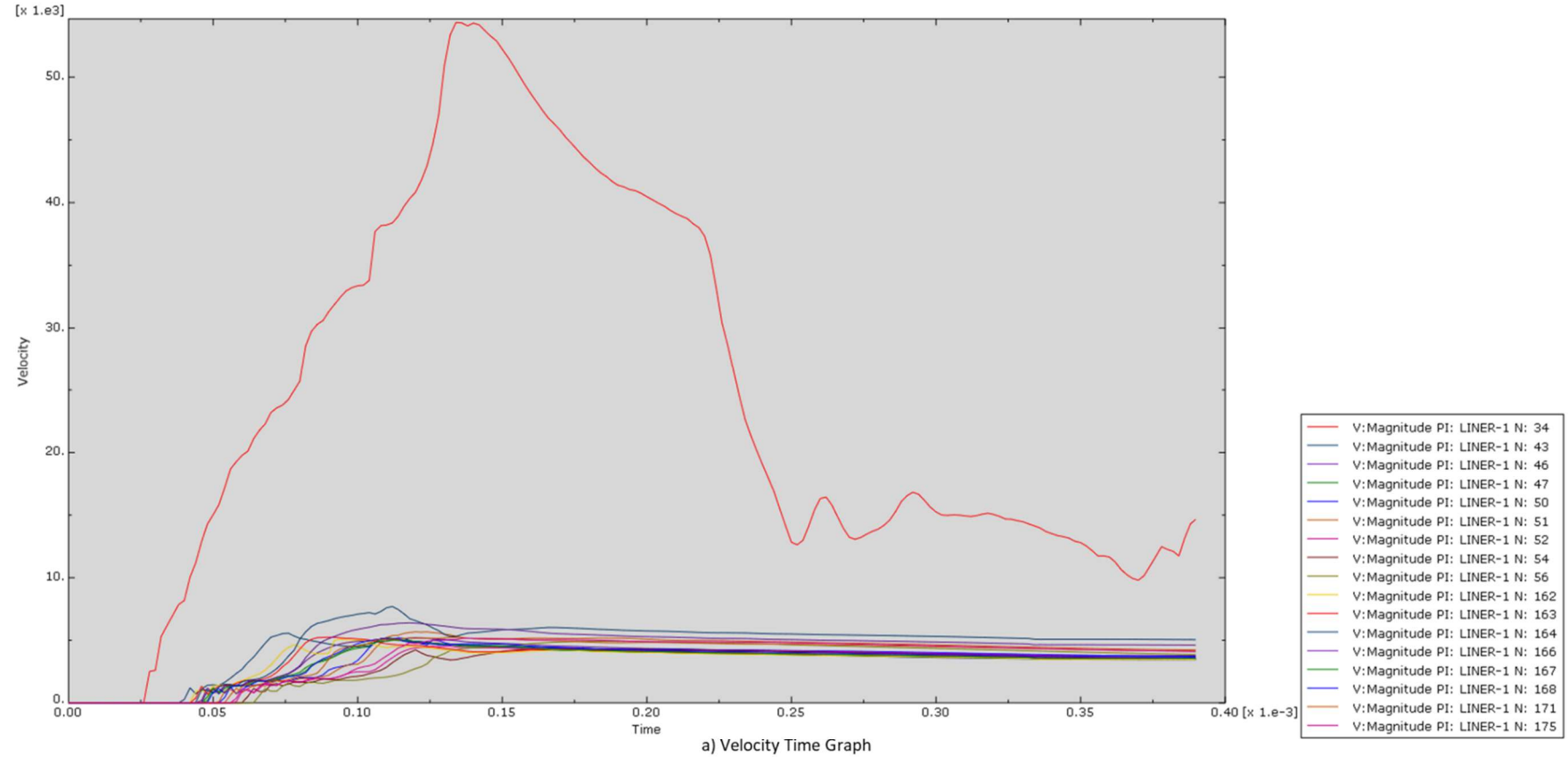
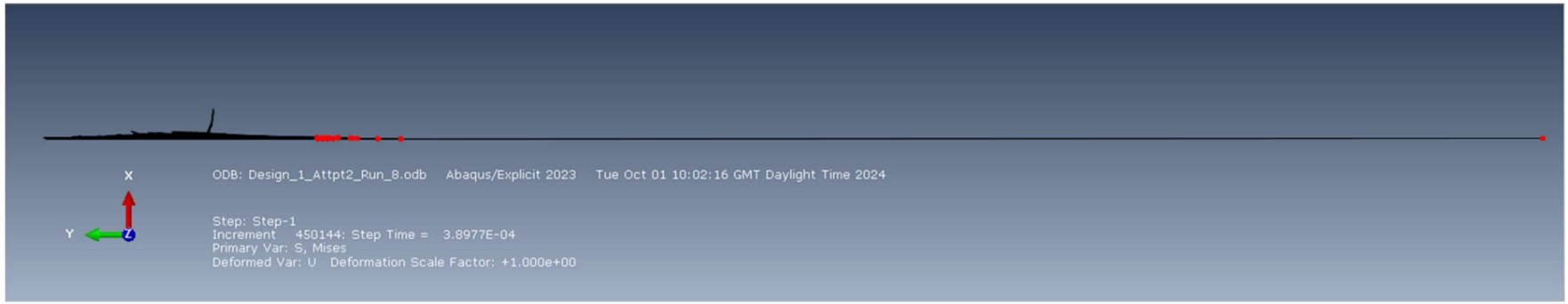


Figure 6-9 - 2D_Design_One_Jet_Run Displacement Graph for Nodes 34 And 164



a) Velocity Time Graph



b) Selected node for Velocity Time Graph

Figure 6-10 - 2D_Design_One_Jet_Run a) Velocity Graph During Jet Formation Highlighting b) Selected Nodes

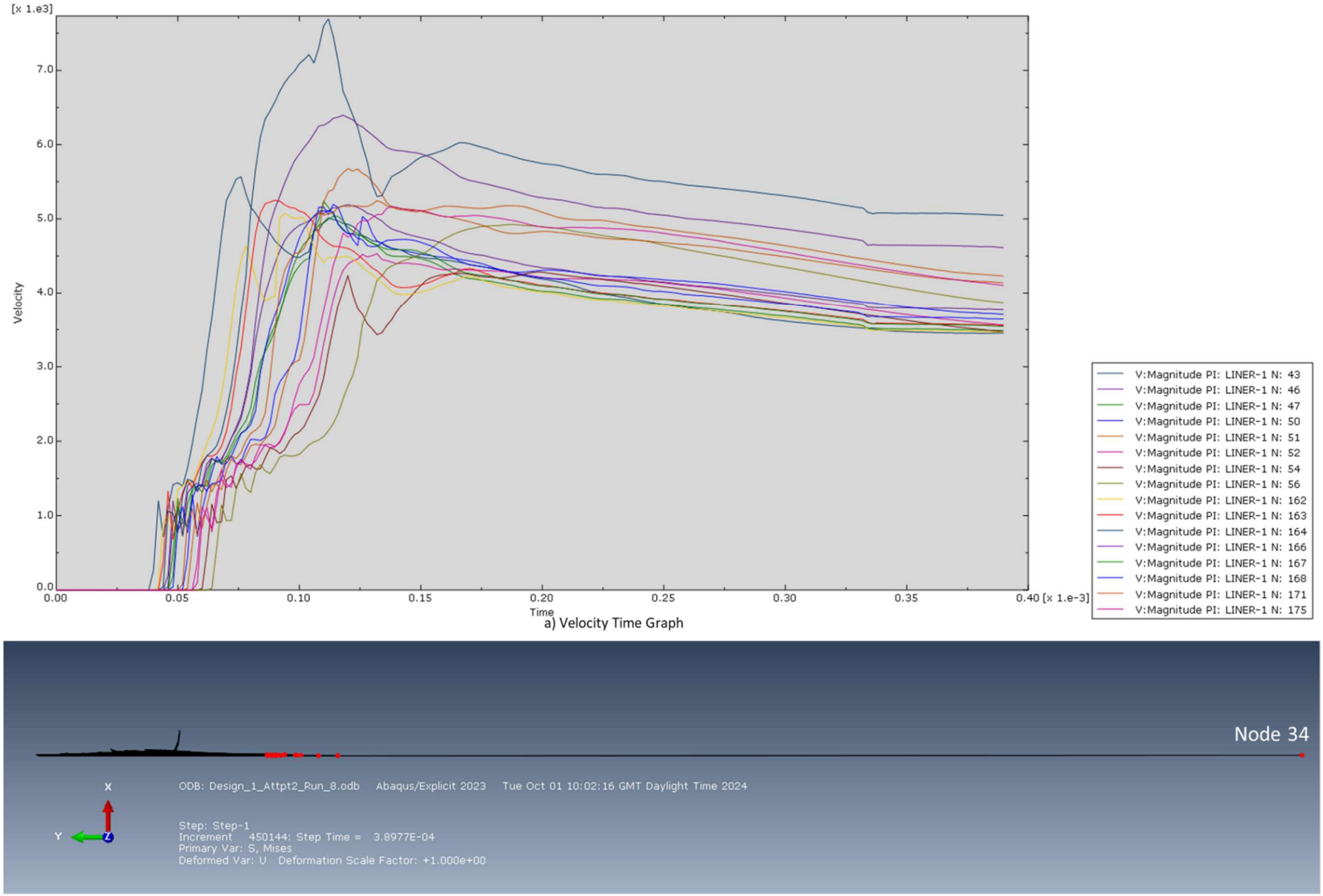
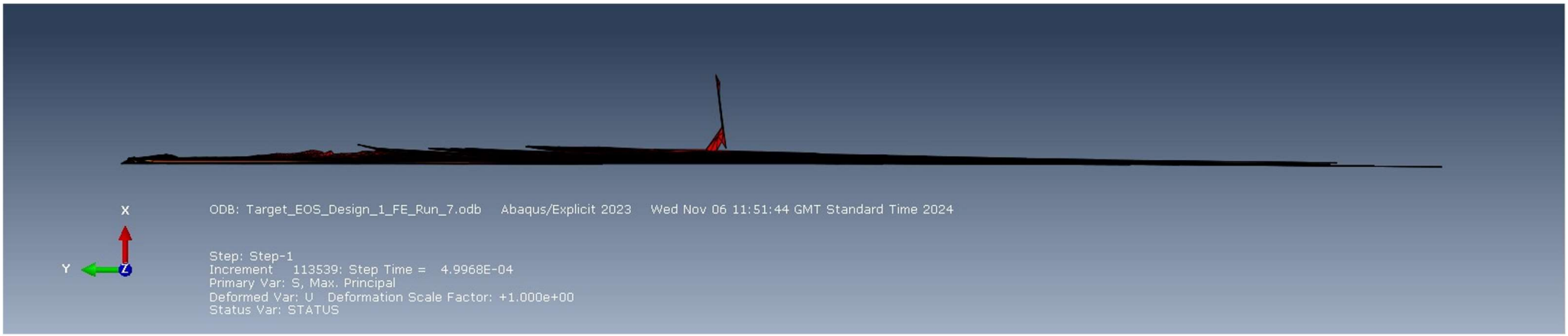


Figure 6-11 - 2D_Design_One_Jet_Run a) Velocity Graph During Jet Formation Disregarding Node 34 with b) Selected Nodes

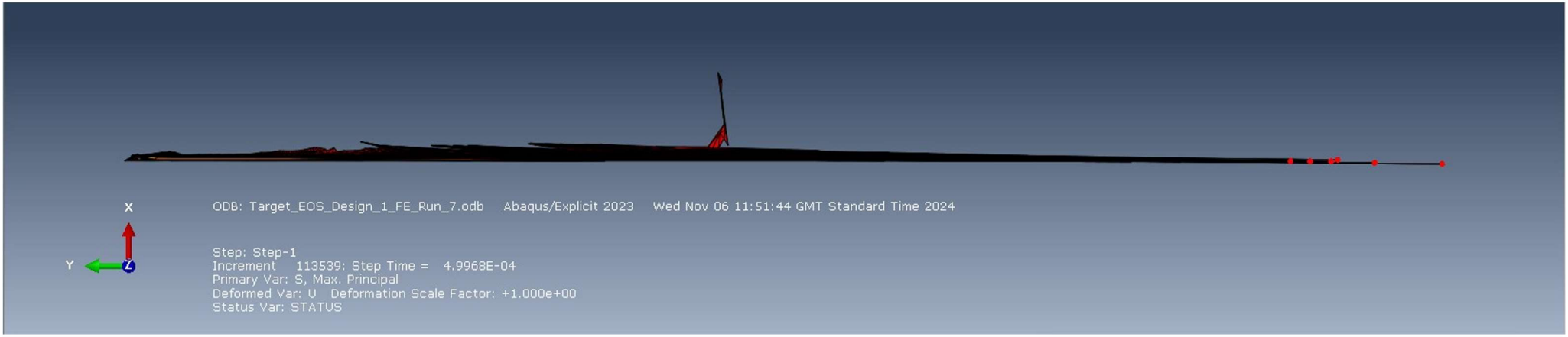
6.1.2 Design One Target Penetration Analysis

Design One's penetration simulation (2D_Design_One_Target_Run) aborted before completion at 4.9968×10^{-4}s with an output of 250 frames. Given though this simulation ran longer, the abortion was caused again by an excessively distorted element in the casing.

The jet formation in Figure 6-12, has no abnormal node displacement in the jet, which supports the hypothesis that node 34 in the previous simulation was a potential anomaly. Discounting the target, the jet length is approximately 2-2.5m, the graph in Figure 6-13 represents the nodes shows the displacement over time of the nodes as highlighted in Figure 6-12b.



a) 2D_Design_One_Target_Run Jet Formation



a)) 2D_Design_One_Target_Run Jet Formation with End Nodes Highlighted

Figure 6-12 – 2D_Design_One_Target_Run Jet Formation Results

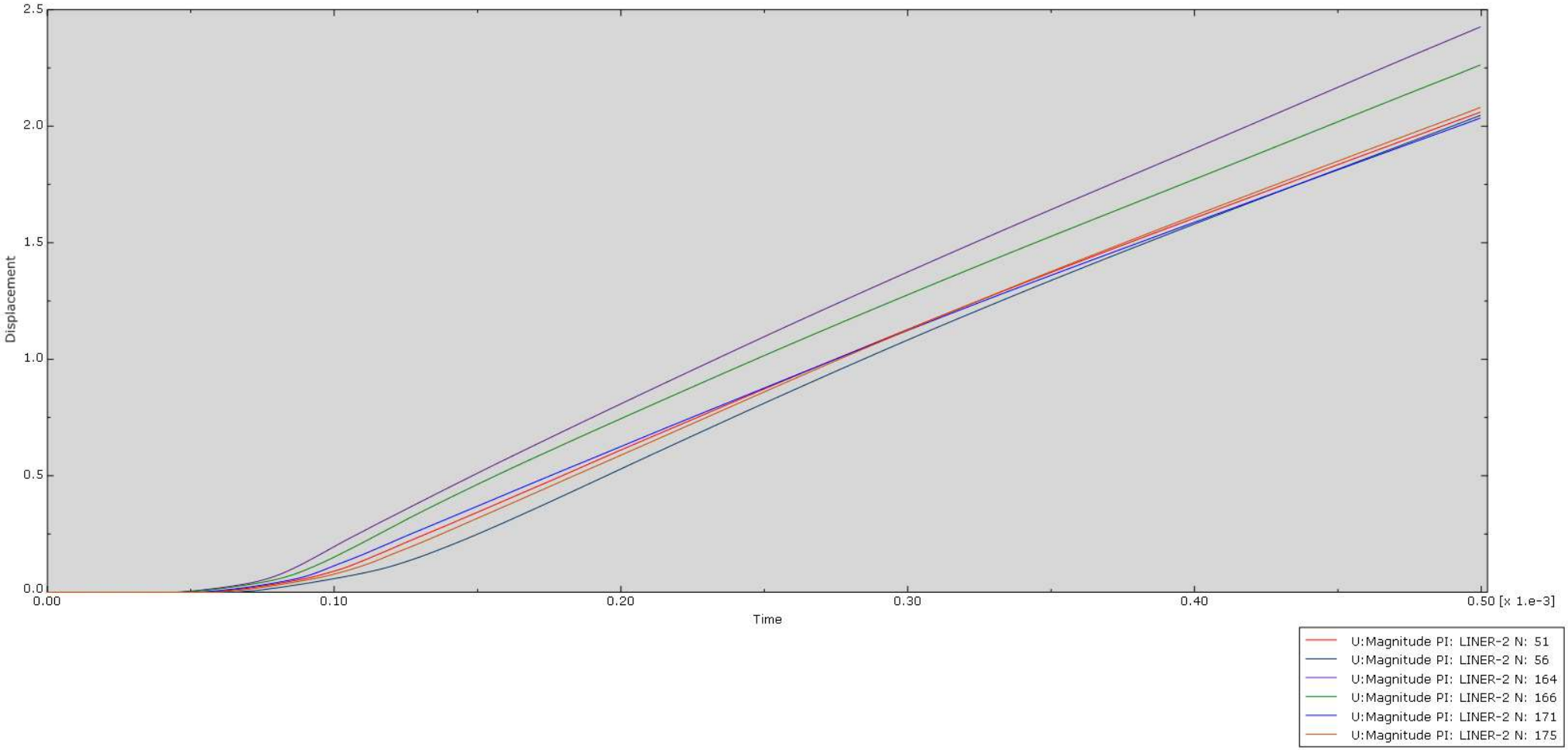


Figure 6-13 – 2D_Design_One_Target_Run Displacement Graph For Nodes Highlighted In Figure 6-12b

The liner impacts the target and starts to penetrate at 3.06×10^{-4}s, this initial penetration is presented in Figure 6-14a. It can be seen that part of the liner has breached the numerical axis of the design, therefore bypassing the target. The breach could be a result of an error in the boundary conditions set or element distortion. Figure 6-14b shows the same impact with the target isolated.

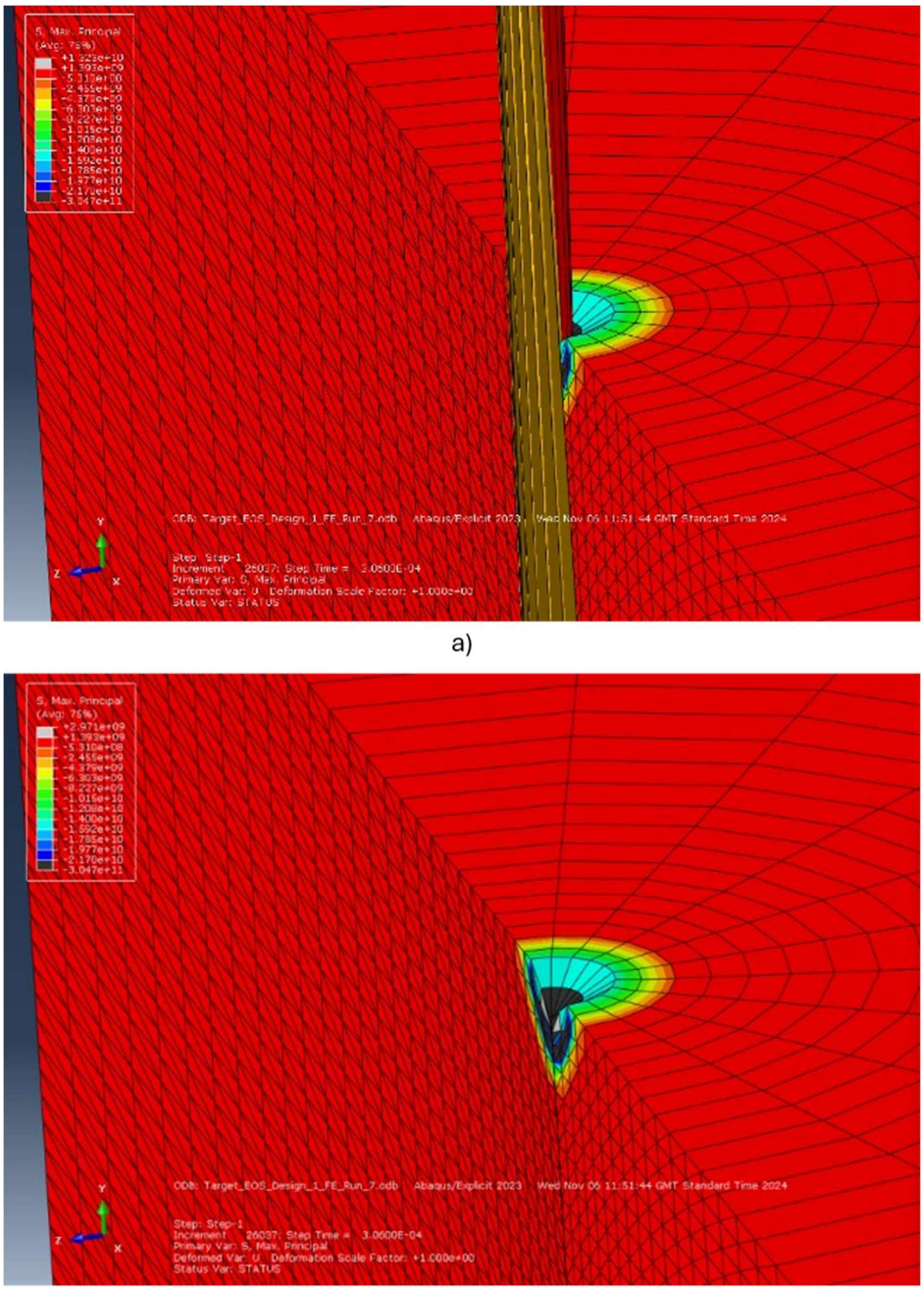


Figure 6-14- 2D_Design_One_Target_Run Initial Impact on The Target a) with The Liner Shown and b) without The Liner Shown

How the liner penetrates the target from the initial contact to the simulation aborting is presented in Figure 6-15. The liner has been removed to provide an improved visual of the penetration depth. It can be shown there is a compression wave travelling ahead of the liner by the yellow and green curve, exerting a stress in the region of 6-7GPa. In Figure 6-15c, Figure 6-15d and Figure 6-16, there is

evidence of a tensile stress in the material as the wider section of the jet penetrates the target, this is in the region of 2GPa and highlighted by the red colouring.

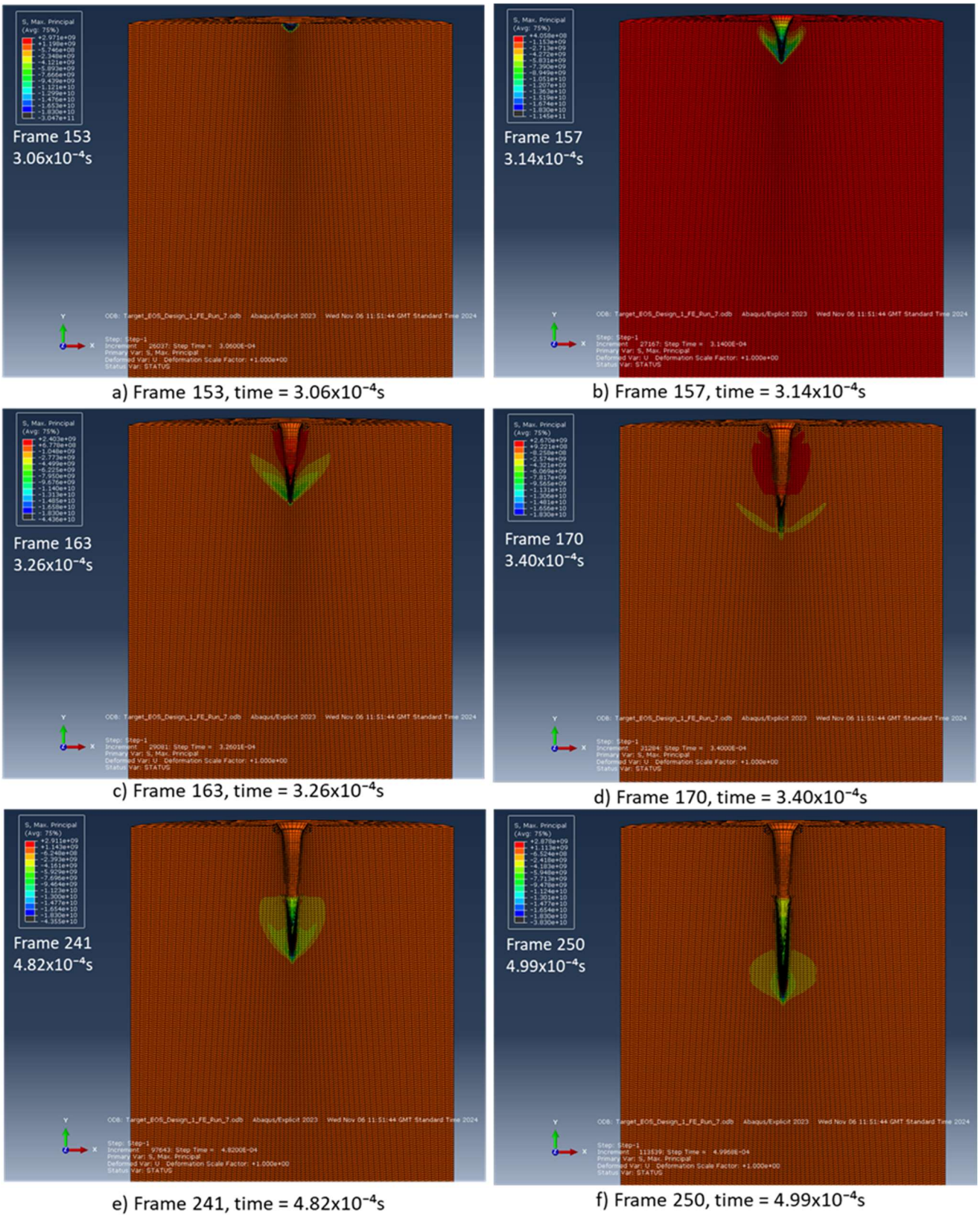
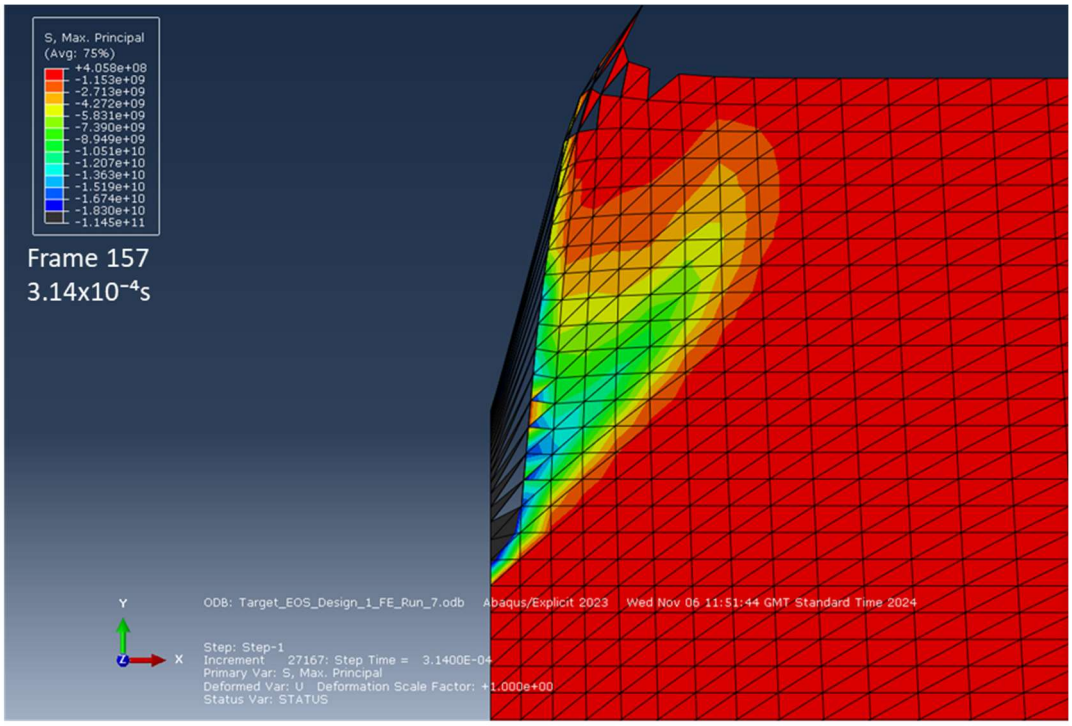
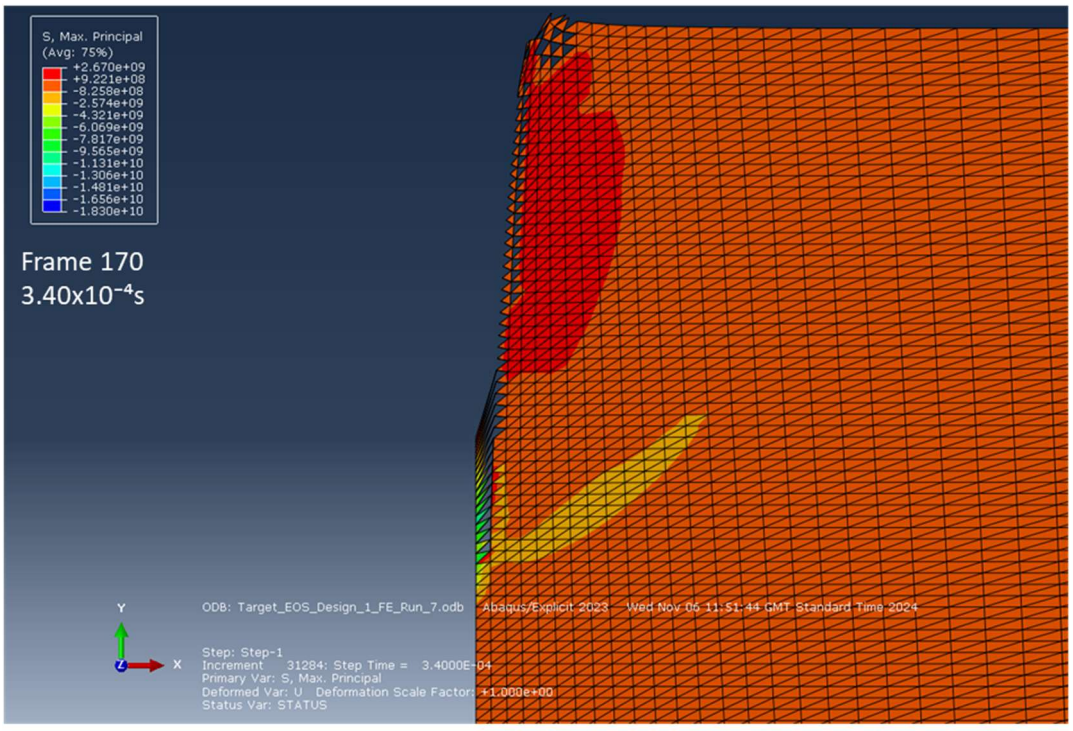


Figure 6-15 – 2D_Design_One_Target_Run Jet Penetration Depth at a) 3.06x10 $^{-4}$s, b) 3.14x10 $^{-4}$s, c) 3.26x10 $^{-4}$s, d) 3.40x10 $^{-4}$s, e) 4.82x10 $^{-4}$s and f) 4.99x10 $^{-4}$s

During penetration, the target undergoes significant material failure illustrated by the deleted elements in Figure 6-16. This deletion indicates that fragmentation or peeling would be expected in a physical application.



a) Frame 157, time = $3.14x10^{-4}$s



b) Frame 170, time = $3.40x10^{-4}$s

Figure 6-16 –2D_Design_One_Target_Run Target Element Deletion Due to Damage at a) 3.14x10 $^{-4}$s, and b) 3.40x10 $^{-4}$s,

At the point of abortion, the liner has penetrated the target and impacted damage to a depth of 0.3m, this is highlighted in Figure 6-17. The jet is traveling at an average velocity of 5kms $^{-1}$, as shown in Figure 6-18, this is the same average velocity as the jet without a target. This implies the target has had a negligible effect in the tip velocity, which would have been expected due to energy loss to the target during penetration.

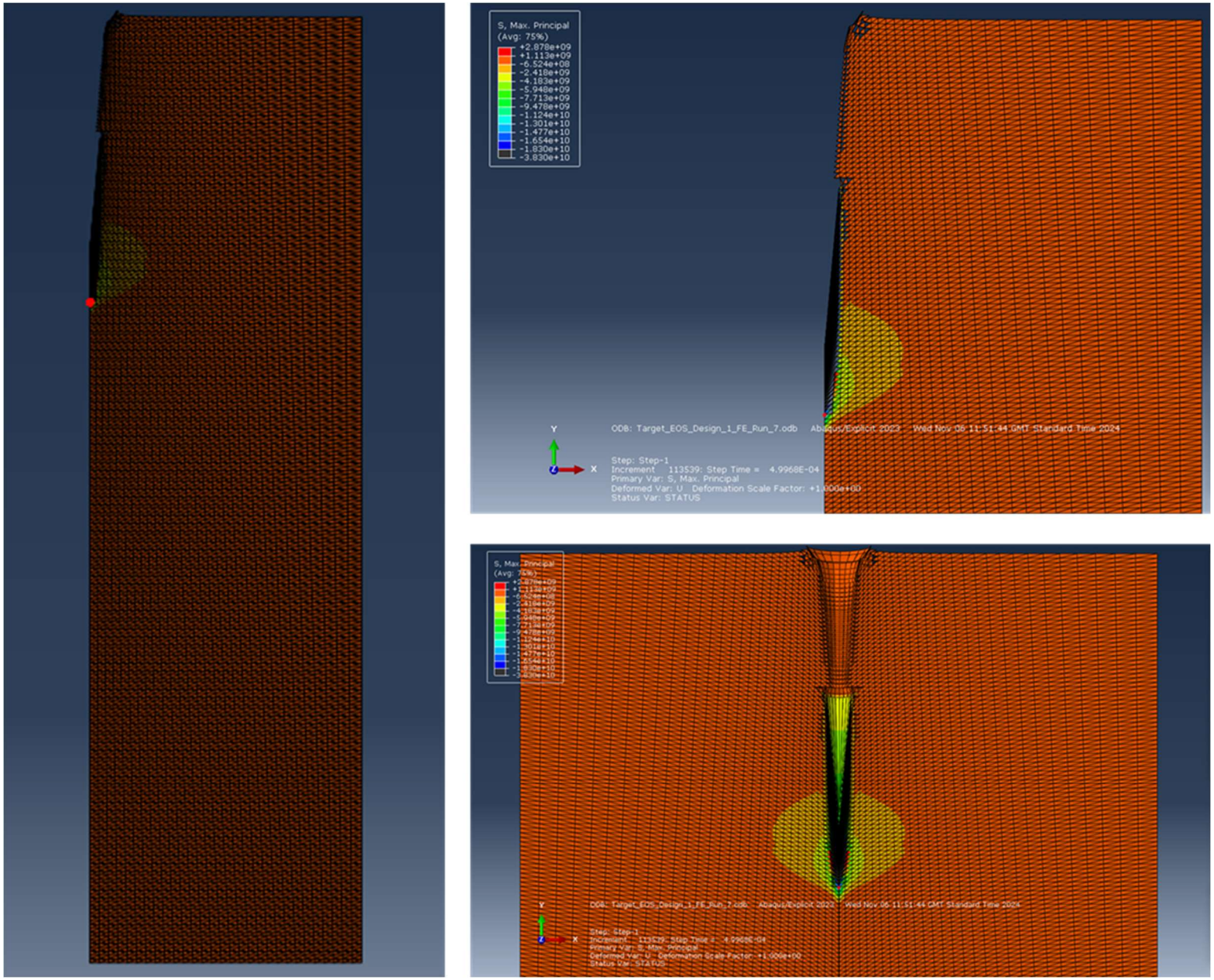
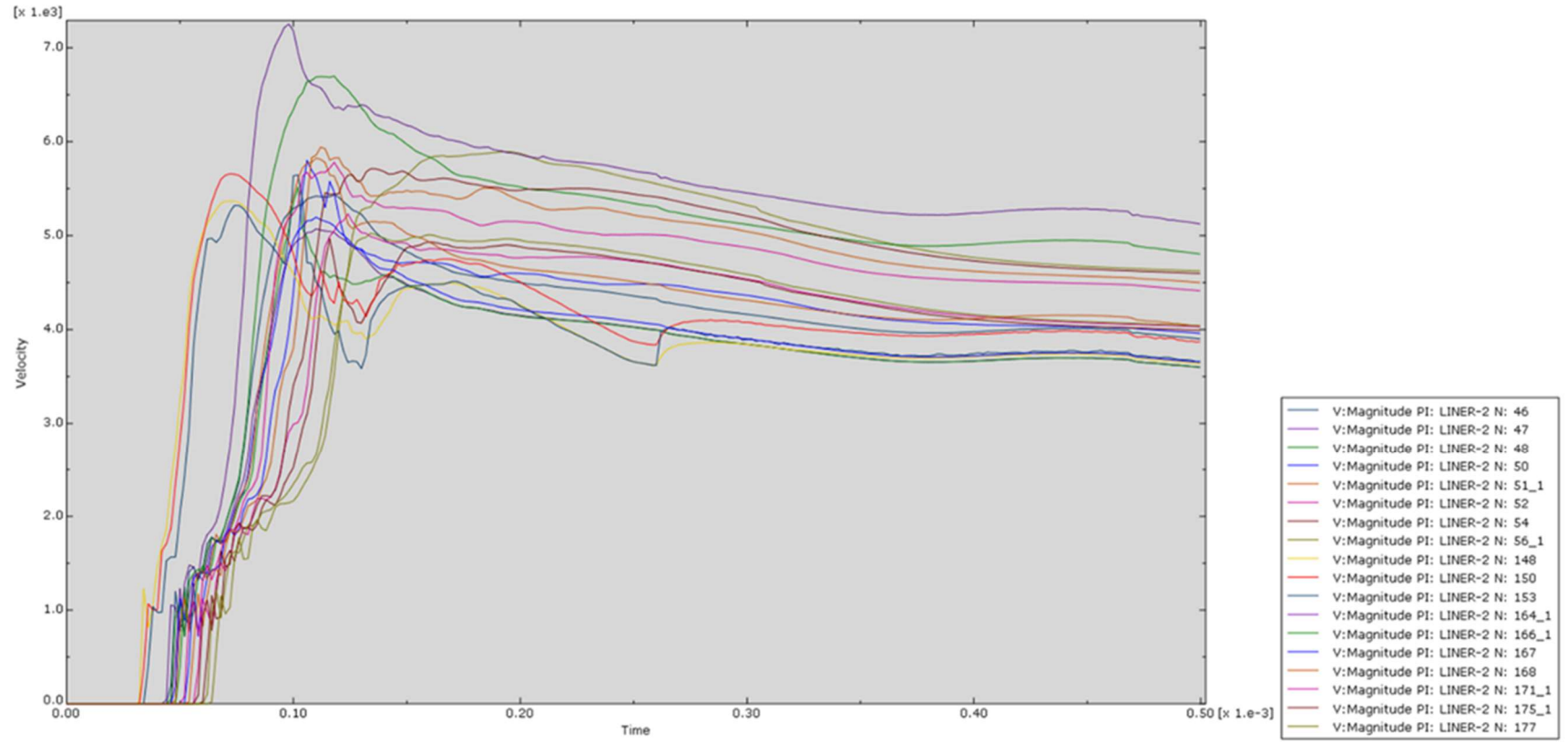
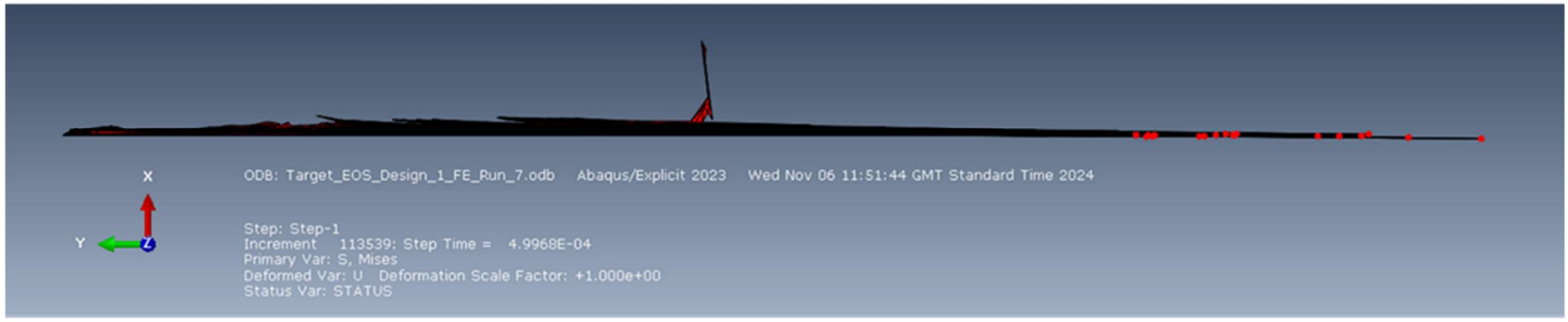


Figure 6-17 – 2D_Design_One_Target_Run Final Penetration Depth



a) Velocity Time Graph



b) Selected node for Velocity Time Graph

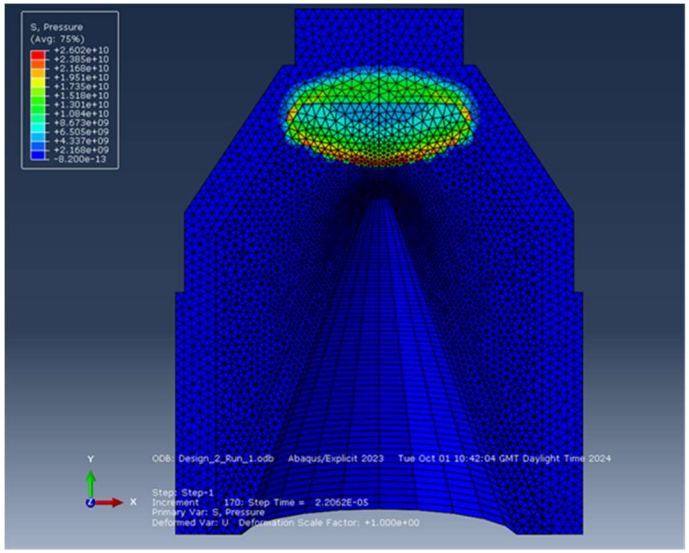
Figure 6-18 - 2D_Design_One_Target_Run a) Velocity Graph During Jet Formation and Target Penetration with b) Selected Nodes

6.2 Design Two Analysis

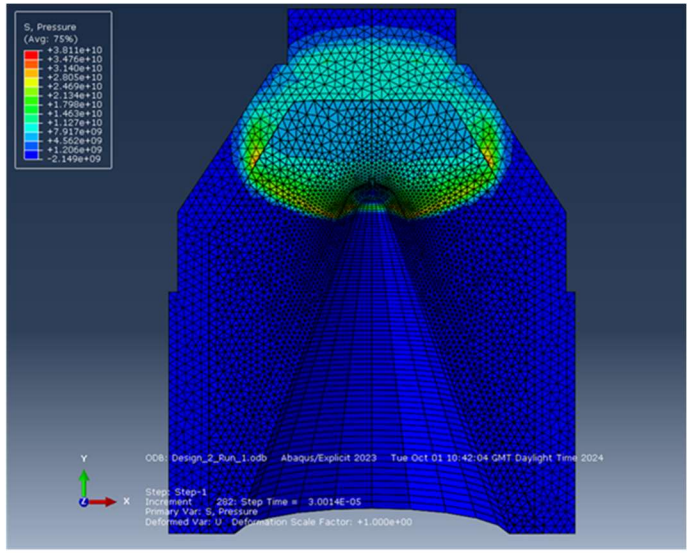
6.2.1 Design Two Jet Formation Analysis

Design Two's initial simulation (2D_Design_Two_Jet_Run) aborted before completion at $3.6443x10^{-4}$s with an output of 183 frames, due to one excessively distorted element in the metal casing. This is comparable to Design One (2D_Design_One_Jet_Run), as the distorted element was in a similar location and Design Two aborted only $0.2x10^{-4}$s before Design One.

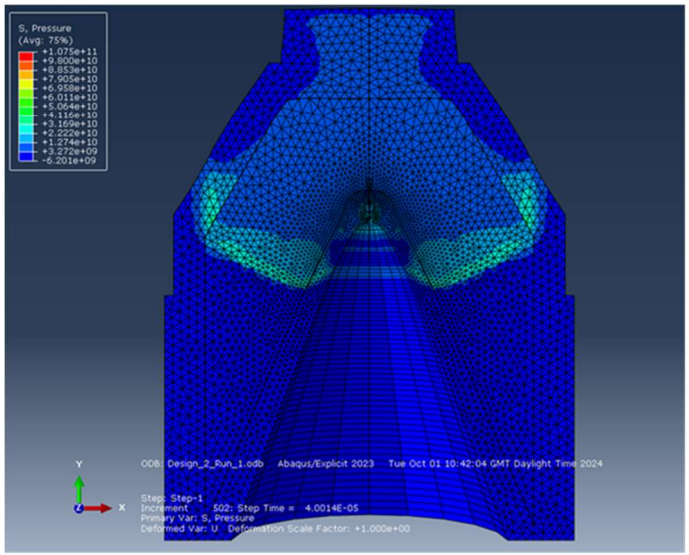
The detonation wave progression, shown in Figure 6-19, is similar to that in 2D_Design_One_Jet_Run. This was expected as there was no change in the material properties used nor to the amount of explosive present, the only change is the thickness of the liners base. Isolating the liner in Figure 6-20, it can be shown, that similar to 2D_Design_One_Jet_Run, the pressure is initially exerted onto the sides of the liner rather than the top. As the wave progresses it is exerting the same level of pressure of approximately 20GPa onto the bottom of the liner's apex at during its collapse, however the pressure does not reach the same high levels as in 2D_Design_One_Jet_Run.



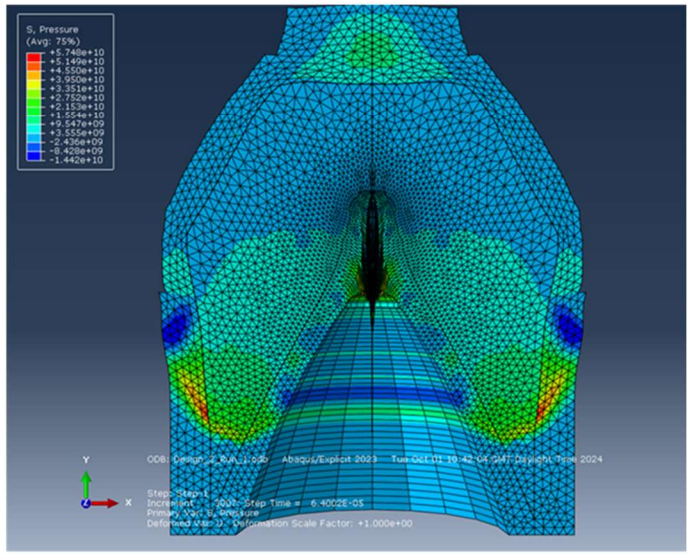
a) Step 11, time = 2.2062×10^{-5}s



b) Step 15, time = 3.0014×10^{-5}s

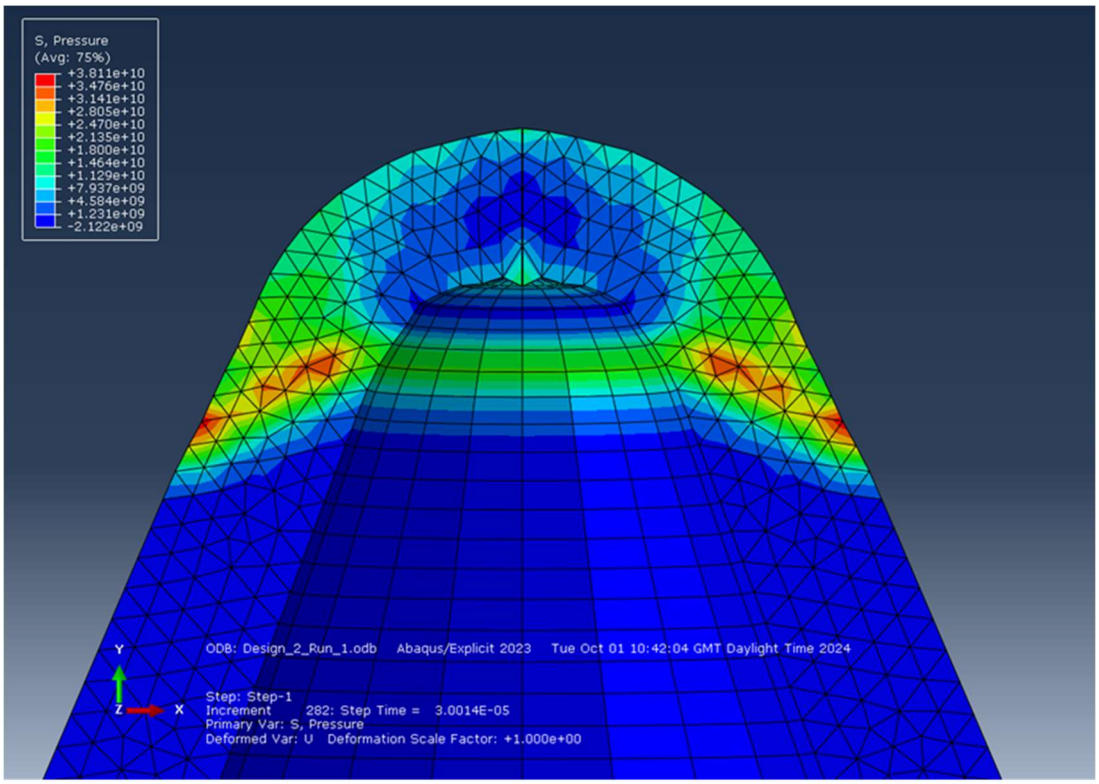


c) Step 20, time = 4.0014×10^{-5}s

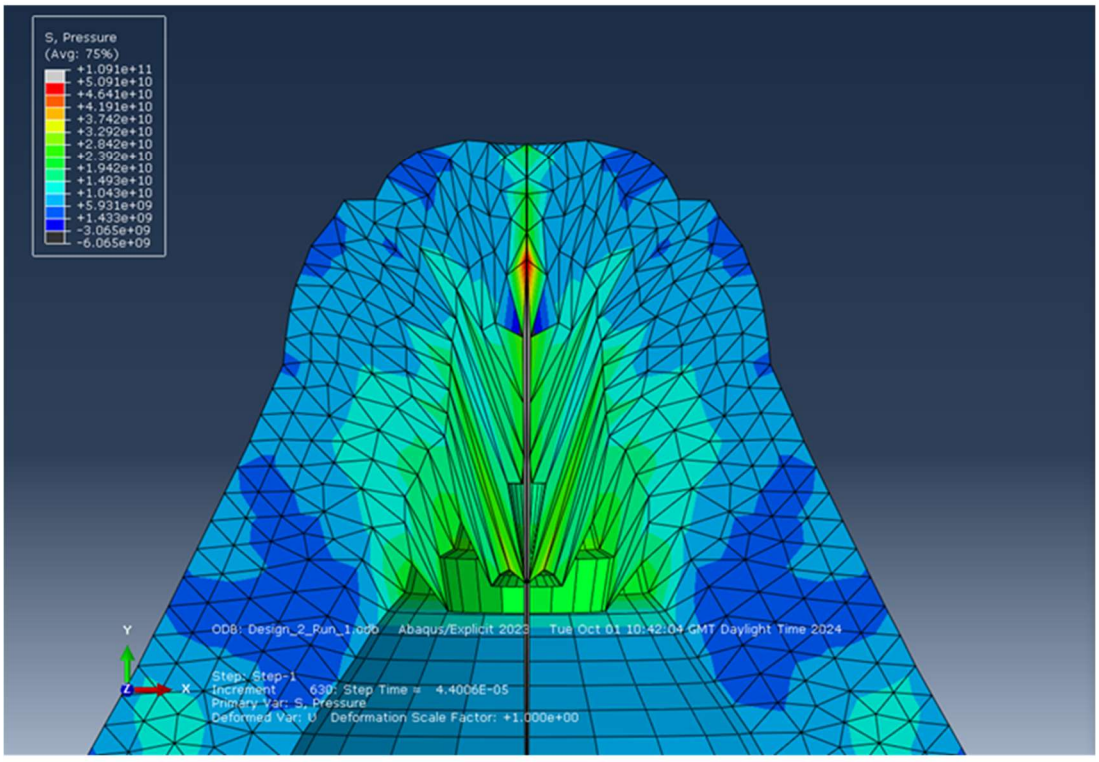


d) Step 32, time = 6.4002×10^{-5}s

Figure 6-19 - 2D_Design_Two_Jet_Run Pressure Exerted from the Detonation Wave at a) 2.262×10^{-5}s, b) 3.0014×10^{-5}s, c) 4.0014×10^{-5}s and d) 6.4002×10^{-5}s



a) Frame 15, time = 3.0014×10^{-5}s

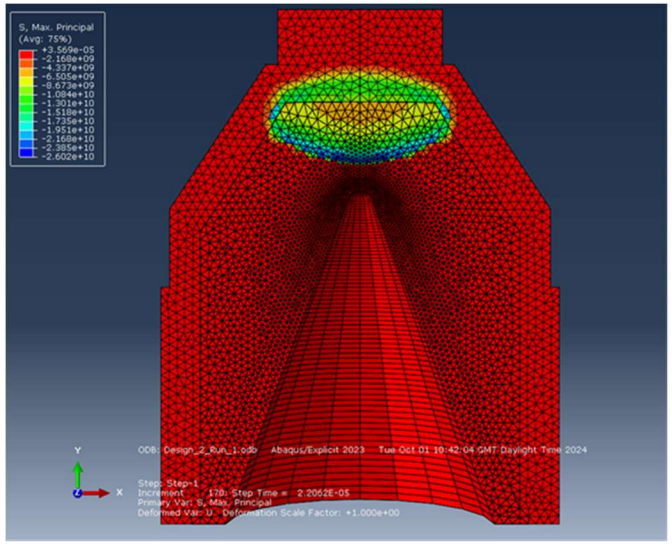


b) Frame 22, time = 4.4006×10^{-5}s

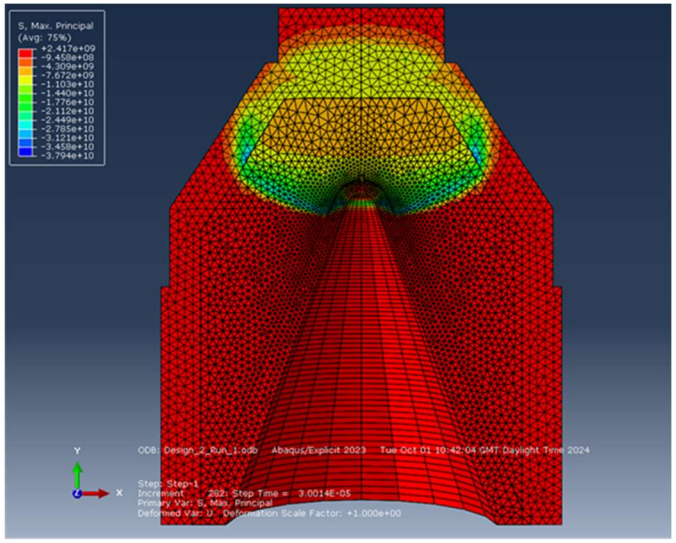
Figure 6-20 – 2D_Design_Two_Jet_Run Pressure Exerted on Apex Of Liner During Start Of Liner Collapse At a) 3.0014×10^{-5}s and b) 4.4006×10^{-5}s

Similar to 2D_Design_One_Jet_Run, as the detonation wave progresses through the shaped charge, the material in front of the wave is being compressed. This is illustrated in Figure 6-21, with the blue and green colours representing the negative stress values. The liner collapse is

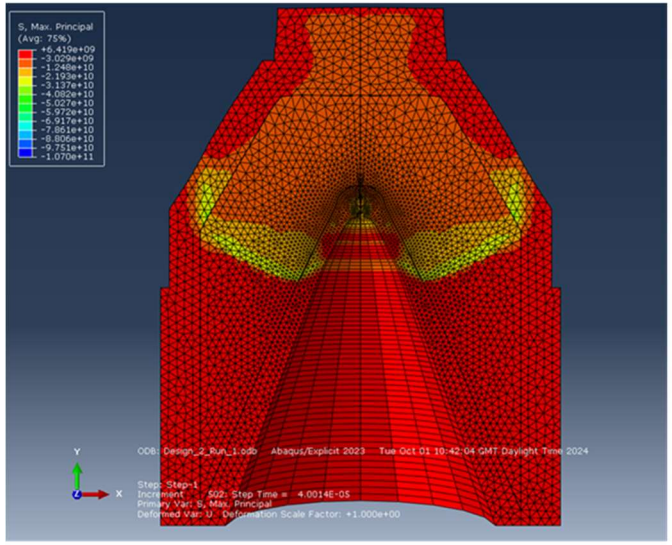
comparatively slower than that of 2D_Design_One_Jet_Run. At $8.8x10^{-5}$s (Figure 6-22) 2D_Design_Two_Jet_Run has experienced less stress due to compression, with the outer edge in the region of 4GPa and the inner edge only reaching 30GPa. The liner starts to reach comparable stresses of near 60GPa at $9.2\ x10^{-5}$s as illustrated in Figure 6-23.



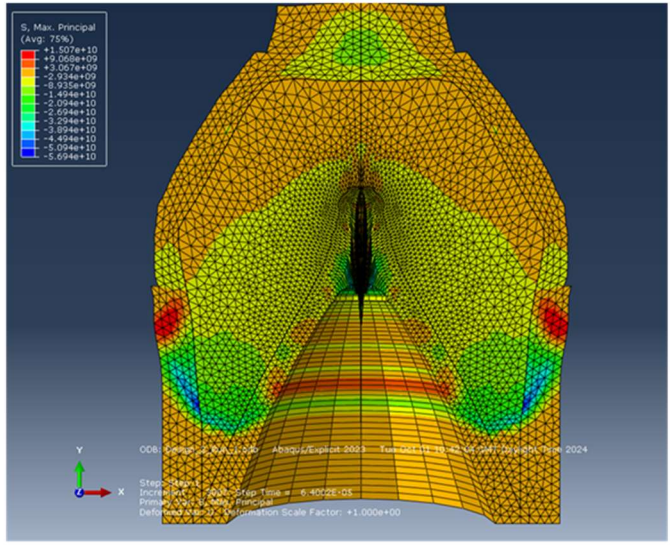
a) Step 11, time = 2.2062×10^{-5}s



b) Step 15, time = 3.0014×10^{-5}s

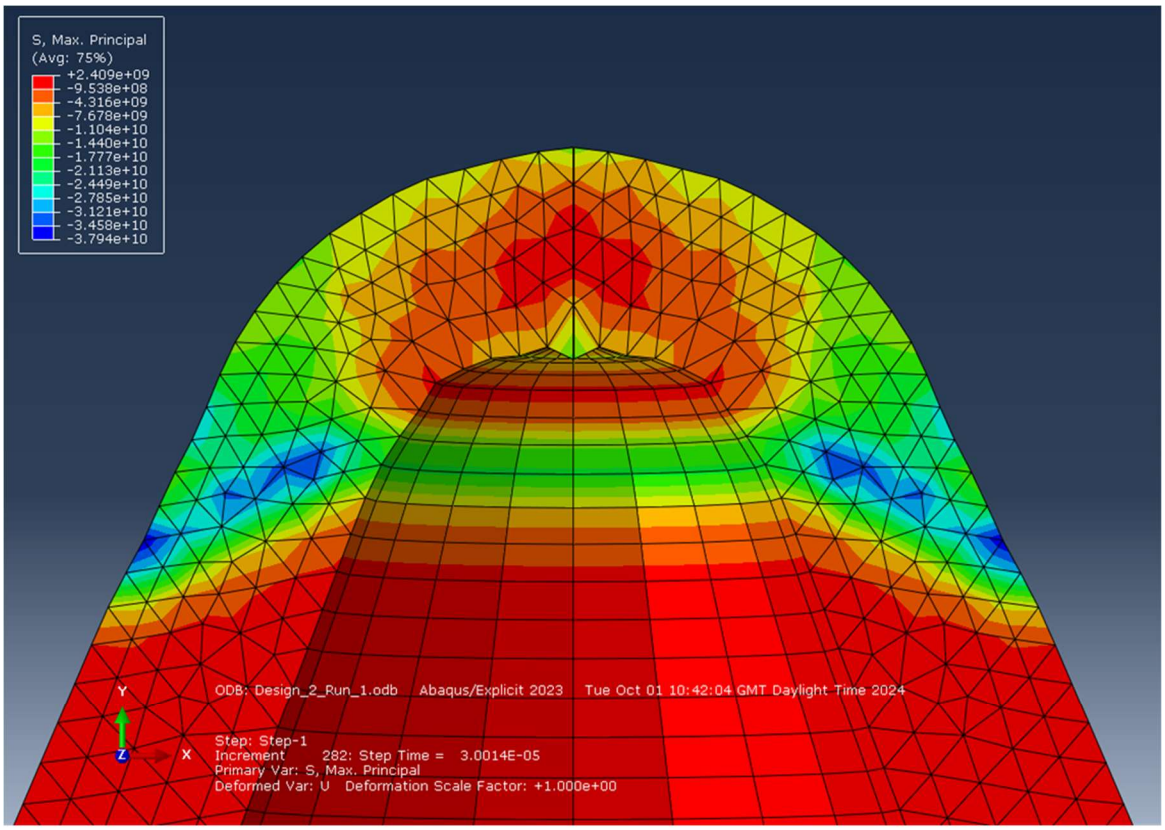


c) Step 20, time = 4.0014×10^{-5}s

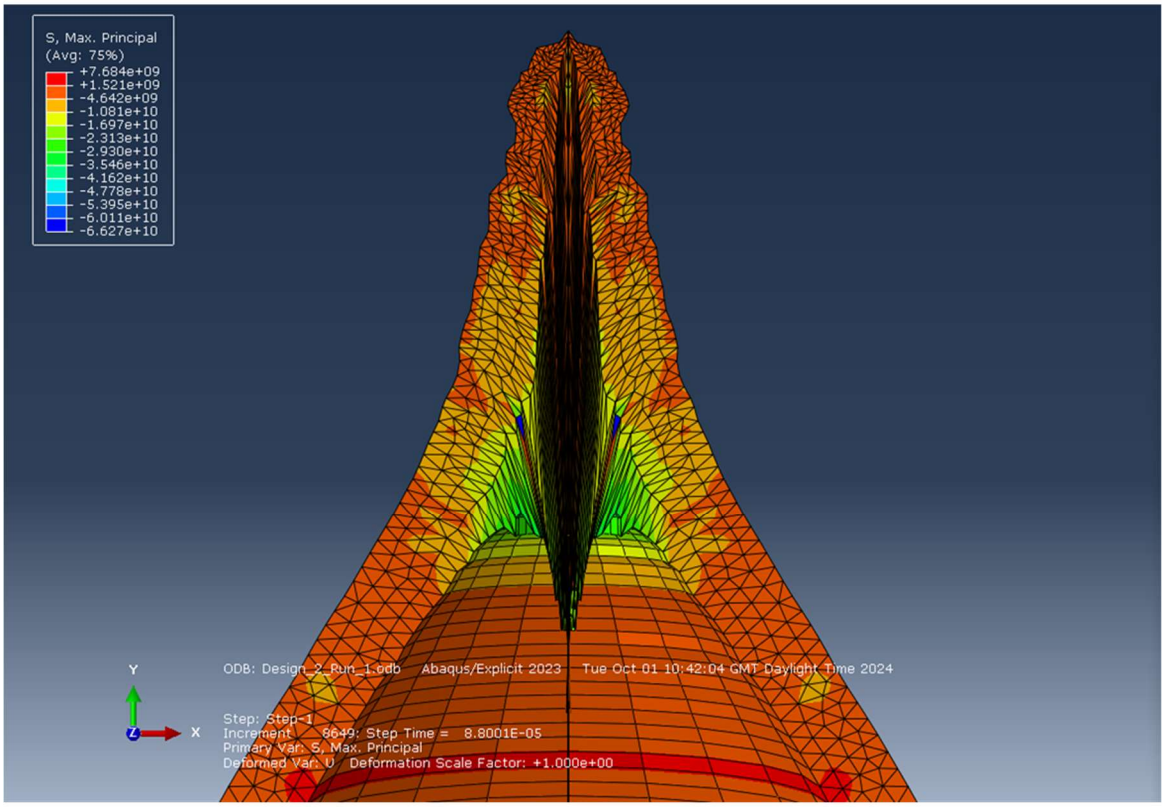


d) Step 32, time = 6.4002×10^{-5}s

Figure 6-21 - 2D_Design_Two_Jet_Run Compressive and Tensile Stresses from the Detonation Wave at a) 2.262×10^{-5}s, b) 3.0014×10^{-5}s, c) 4.0014×10^{-5}s and d) 6.4002×10^{-5}s



a) Frame 15, time = 3.0014×10^{-5}s



b) Frame 44, time = 8.8001×10^{-5}s

Figure 6-22 - 2D_Design_Two_Jet_Run Stress Exerted on Apex of Liner During Start Of Liner Collapse At a) 3.0014×10^{-5}s and b) 8.8001×10^{-5} s

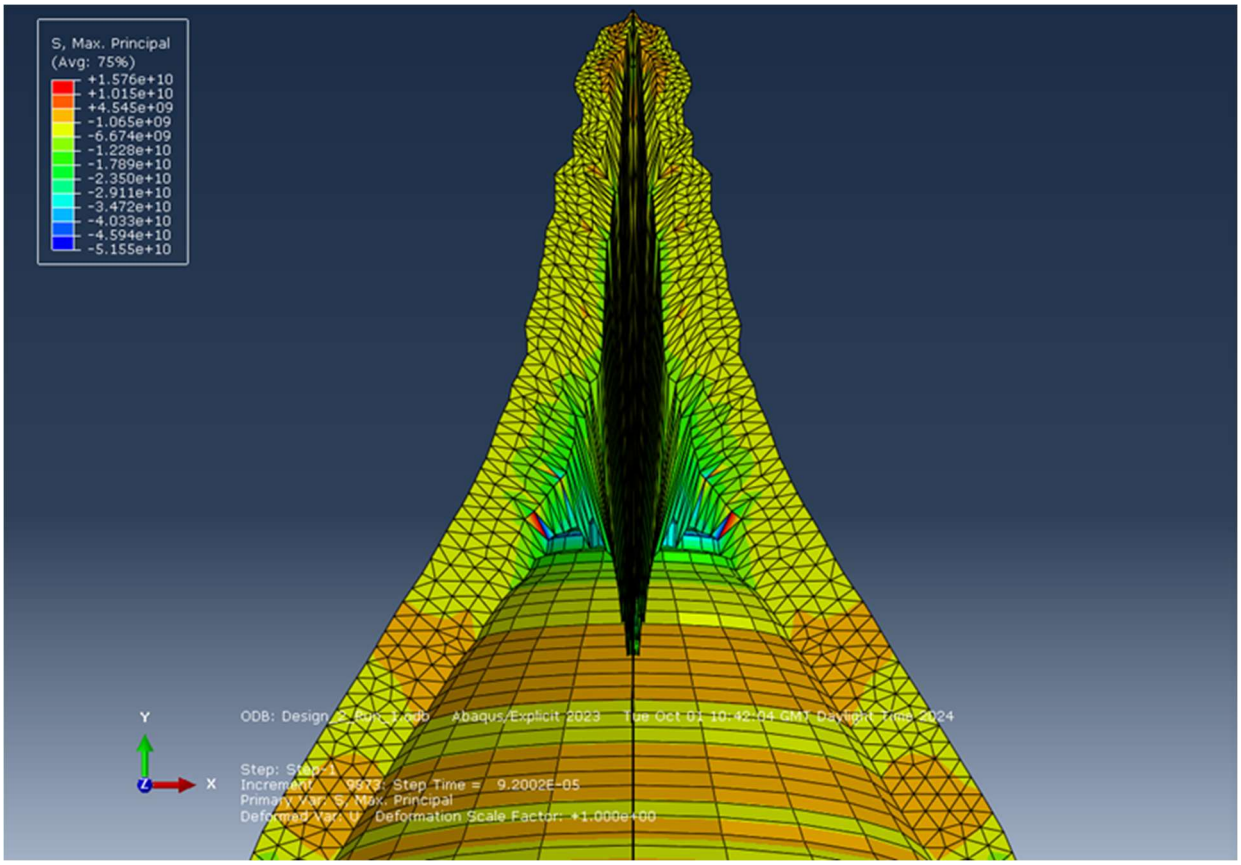


Figure 6-23 -2D_Design_Two_Jet_Run Stress Exerted on Apex of Liner During Start of Liner Collapse At $9.2002x10^{-5}$ s

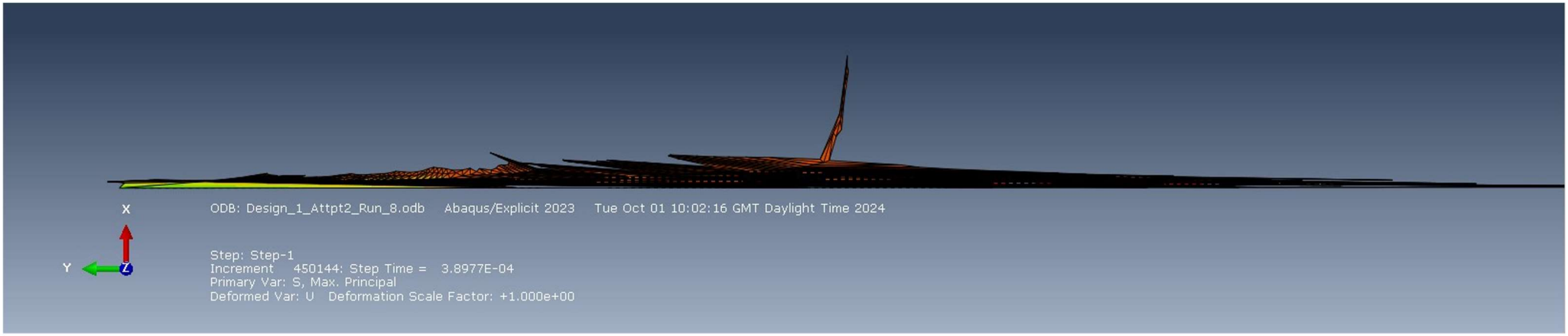
The full jet formation for 2D_Design_Two_Jet_Run is shown in Figure 6-24, with a comparison to 2D_Design_One_Jet_Run's jet length at point of abortion in Figure 6-25, highlighting the difference in jet formation between both designs. It can be seen that the skirt of the jet is thicker compared to 2D_Design_One_Jet_Run, this was due to the liner in 2D_Design_Two_Jet_Run having more material mass at the base. This is in line with the expected result.

At the point of abortion, the jet is approximately 1.5m in length, as evidenced by the displacement graph in Figure 6-26. This is shorter than the jet length of 2D_Design_One_Jet_Run, at its point of abortion.

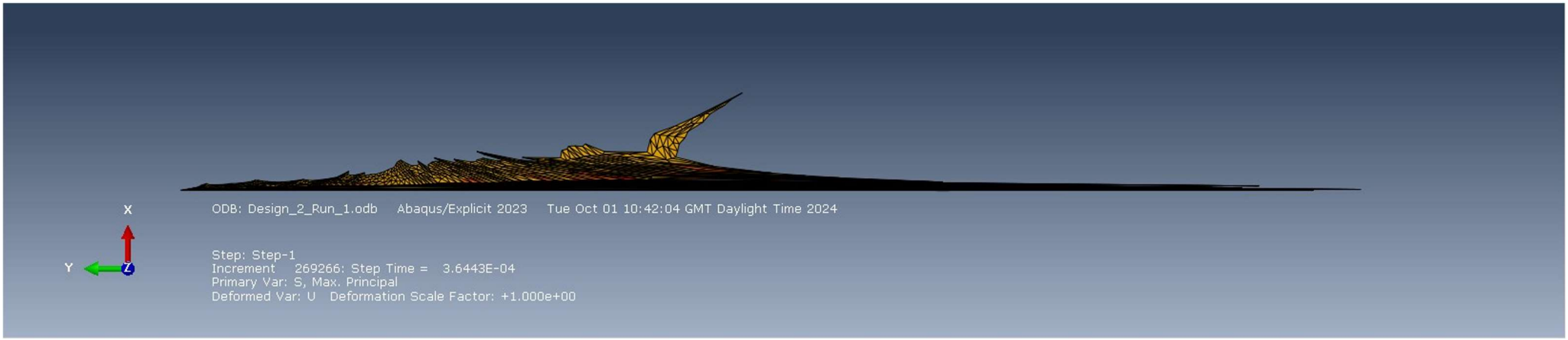
The jet's tip travelled at an average velocity of $4kms^{-1}$. The graph in Figure 6-27 shows how the velocity of selected nodes varied during the jet formation. While the average velocity is the same as 2D_Design_One_Jet_Run, the rate of change is more consistent with 2D_Design_Two_Jet_Run.



Figure 6-24 - 2D_Design_Two_Jet_Run Jet Formation from Liner Collapse to Point of Abortion

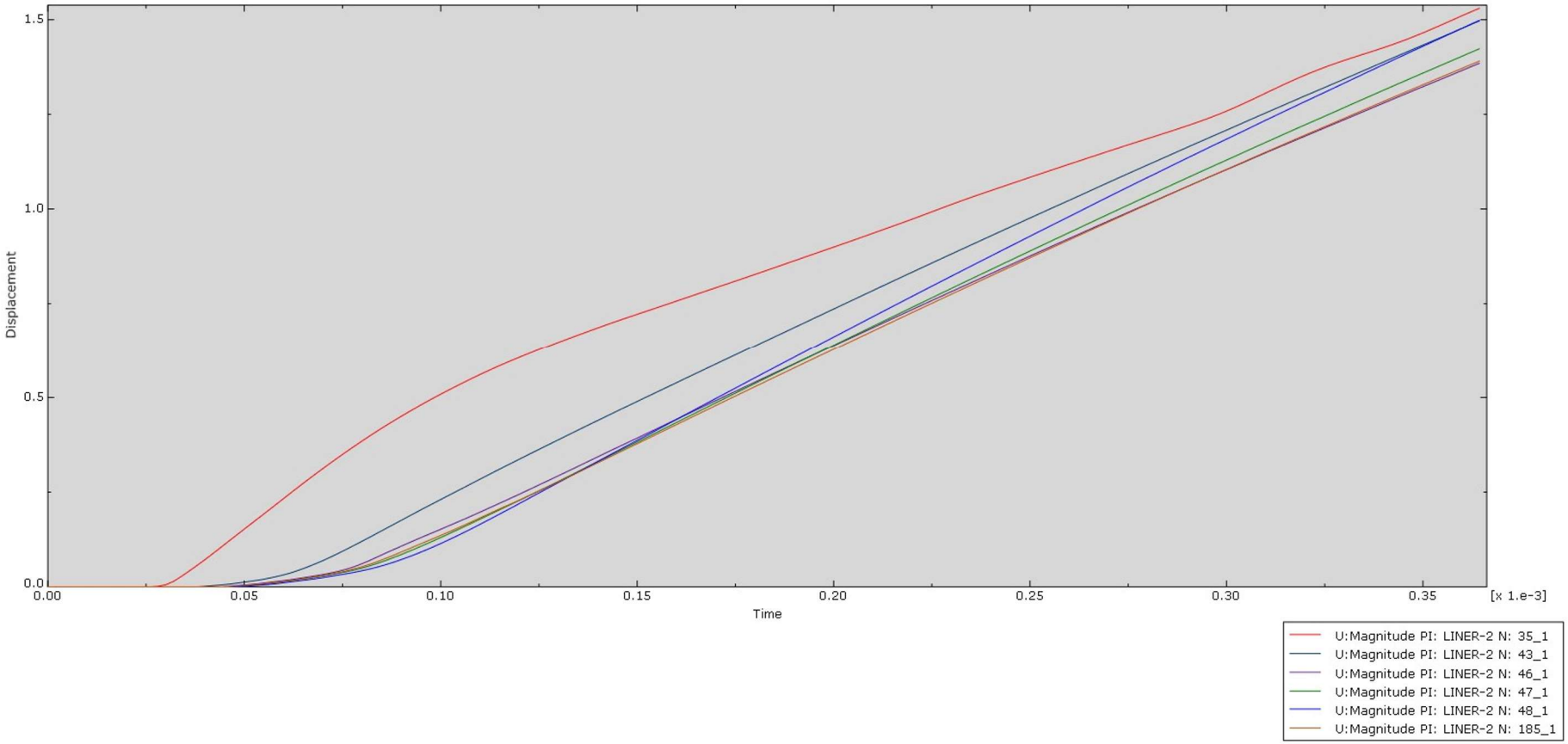


a) 2D_Design_One_Jet_Run - Frame 195, time = 3.8977×10^{-4}s



b) 2D_Design_Two_Jet_Run - Frame 183, time = 3.6413×10^{-4}s

Figure 6-25 - Comparison of a) 2D_Design_One_Jet_Run and b) 2D_Design_Two_Jet_Run Jet Formation at Point of Abortion



a) Displacement Graph



b) Selected nodes for Displacement Graph

Figure 6-26 - 2D_Design_Two_Jet_Run a) Node Displacement Graph for b) Selected Nodes

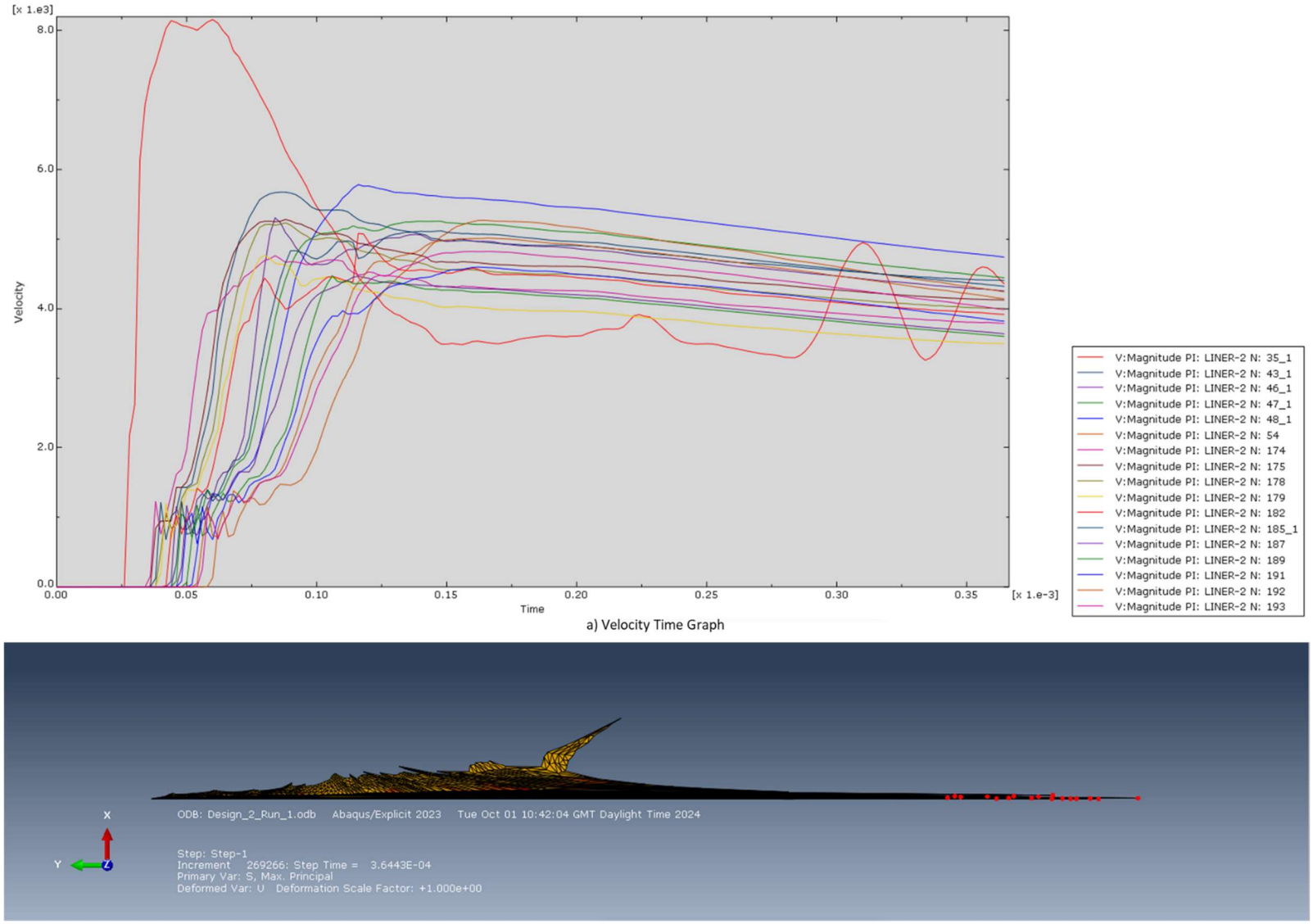


Figure 6-27 - 2D_Design_Two_Jet_Run a) Velocity Graph During Jet Formation Using b) Selected Nodes

6.2.2 Design Two Target Penetration Analysis

Design Two's penetration simulation (2D_Design_Two_Target_Run) aborted before completion at $6.5008x10^{-4}$s with an output of 358 frames due to an excessively distorted element in the metal casing. While the jet formation process is comparable, this simulation ran $30x10^{-3}$s longer than 2D_Design_Two_Jet_Run, and $20x10^{-3}$s longer than 2D_Design_One_Target_Run.

At the point of abortion, illustrated in Figure 6-28, the jet is approximately 2.5-3m long. This is evident by the selected nodes in the liner, as represented in Figure 6-29.

The liner impacts the target at $3.00x10^{-4}$s, with the initial penetration shown in Figure 6-30. Although it penetrated at a similar time frame as 2D_Design_One_Target_Run, the pressure and the stress exerted onto the material is greater in 2D_Design_Two_Target_Run, in the range of 200-400GPa.

How the liner penetrated the target, from the initial contact to point of abortion is given in Figure 6-31, with the liner removed to aid with the visual representation. The increased mass in the liner, results in a greater force exerted on the target increasing the stress by a factor of 10, compared to 2D_Design_One_Target_Run. This is demonstrated in Figure 6-32.

At the point of abortion, the liner has penetrated and impacted damage to a depth of 0.54m as highlighted in Figure 6-33, 0.24m further than 2D_Design_One_Target_Run. From the velocity time graph in Figure 6-34, it is evident that the jet tip for the gradual liner travelled at an initial velocity of $6kms^{-1}$ and decreases to approximately $5kms^{-1}$ when it impacts the liner. Comparing this with 2D_Design_One_Target_Run there is a clearer indication of when the jet decreases in velocity during the target penetration.

The average velocity during 2D_Design_Two_Target_Run is faster than 2D_Design_Two_Jet_Run, combining this with the fact the penetration simulation ran longer in an unexpected way, it appears adding a target has impacted the computing of the model.

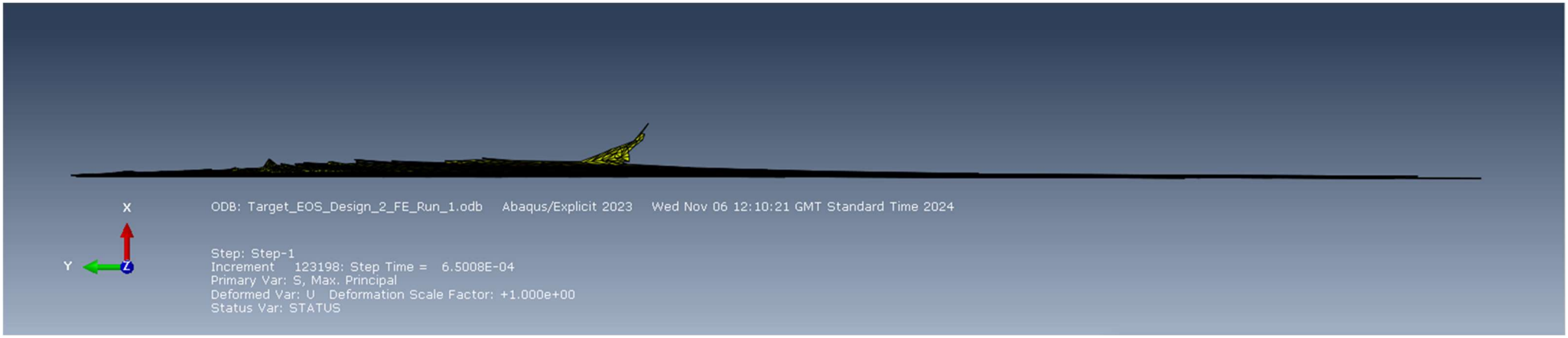
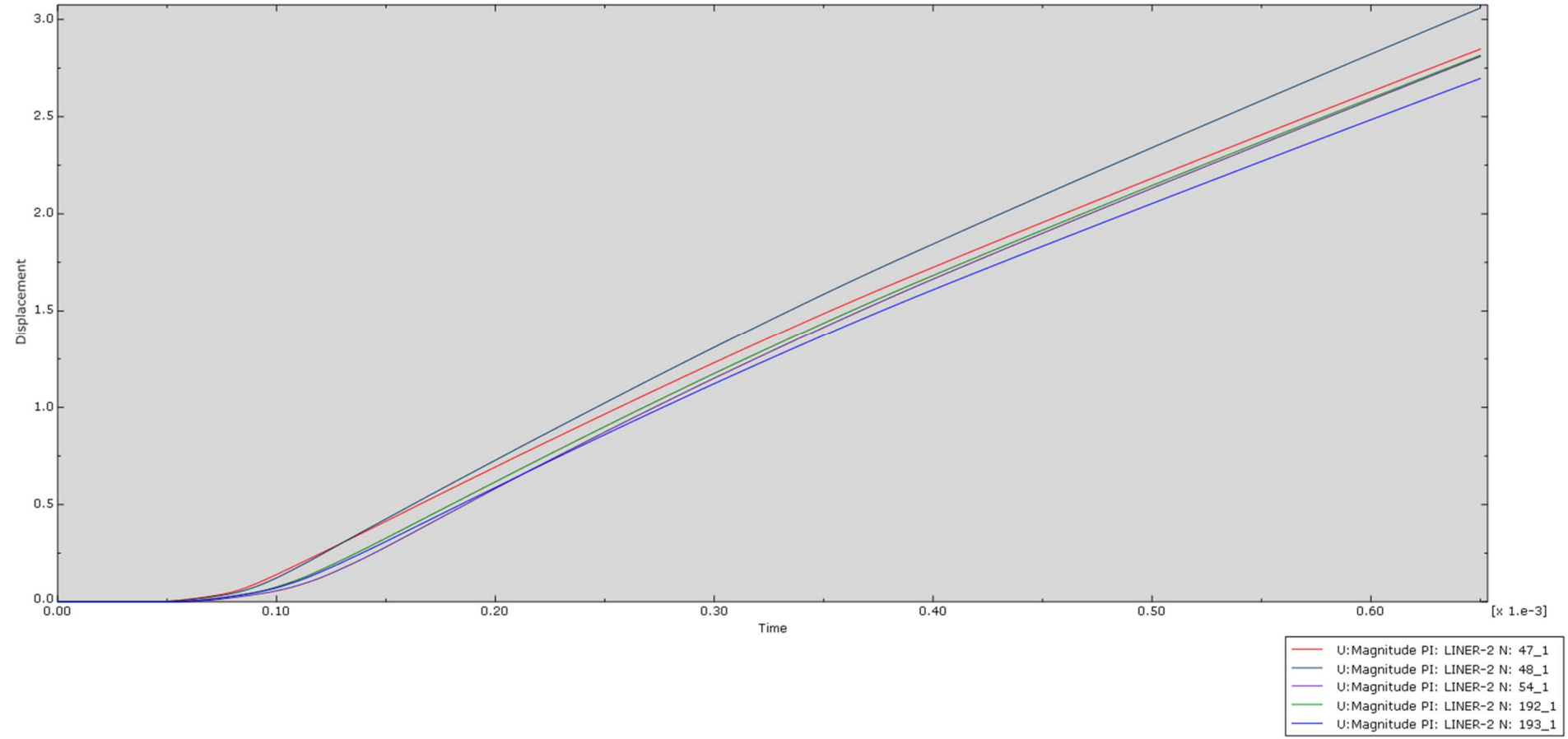


Figure 6-28 – 2D_Design_Two_Target_Run Full Jet Formation

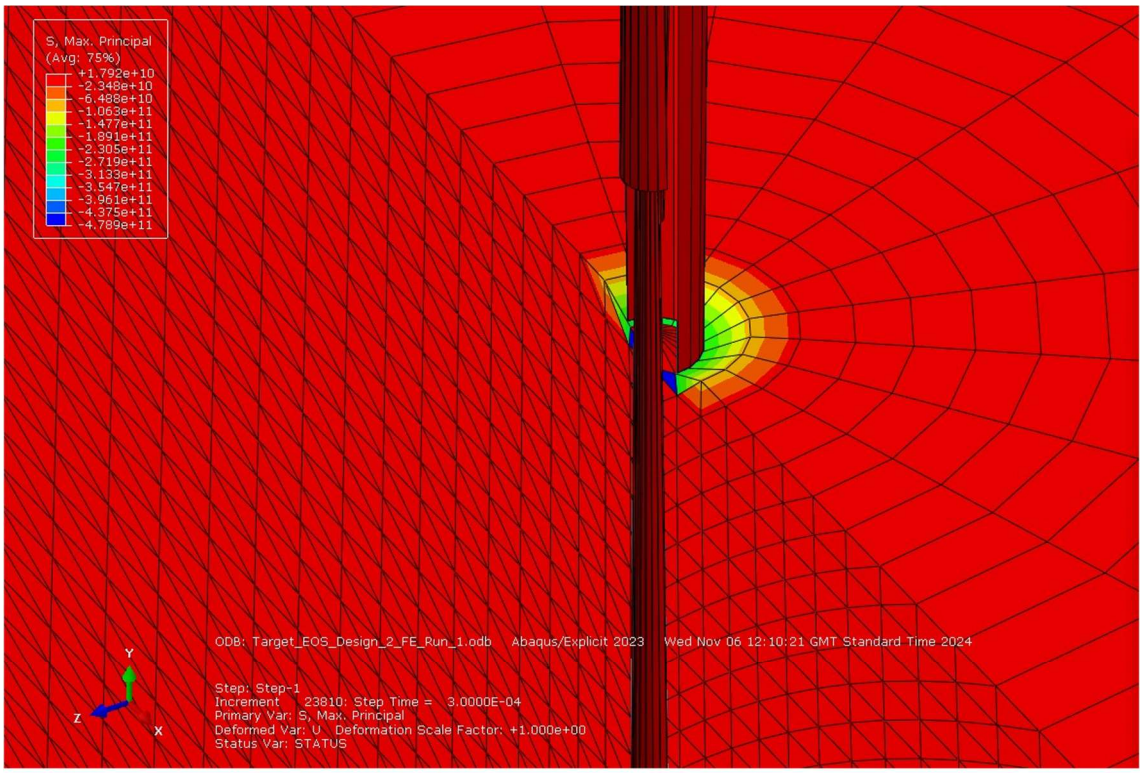


a) Displacement Time Graph

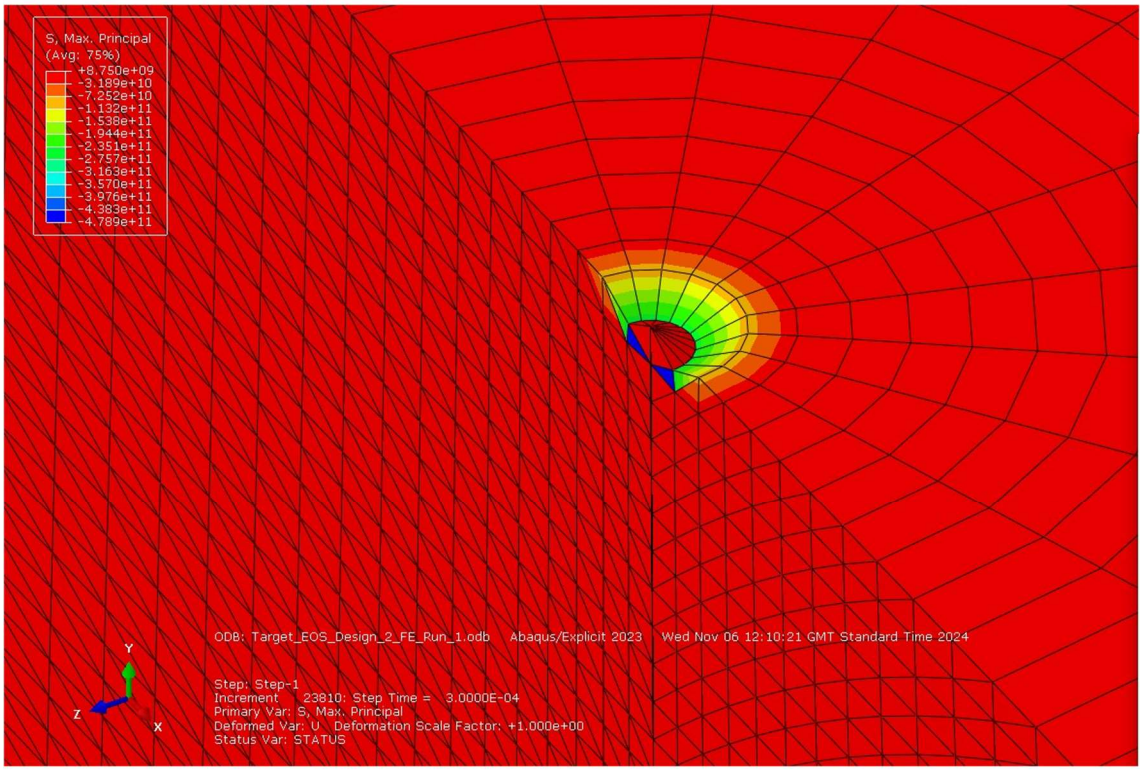


b) Selected nodes for Displacement Time Graph

Figure 6-29 - 2D_Design_Two_Target_Run a) Displacement Graph with b) Selected Nodes



a)



b)

Figure 6-30- 2D_Design_Two_Target_Run Initial Impact on Target a) with the Liner shown and b) Without the Liner shown

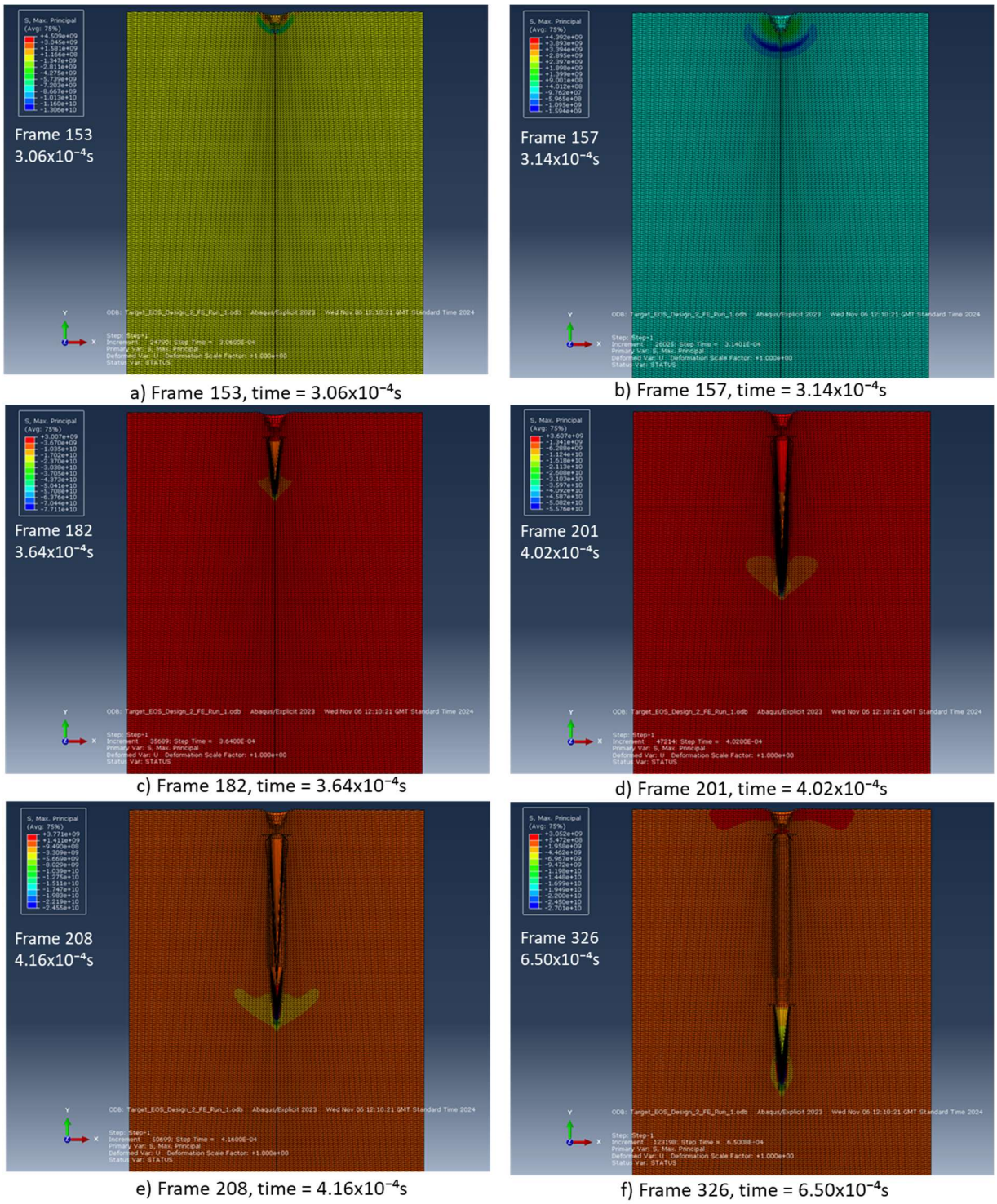
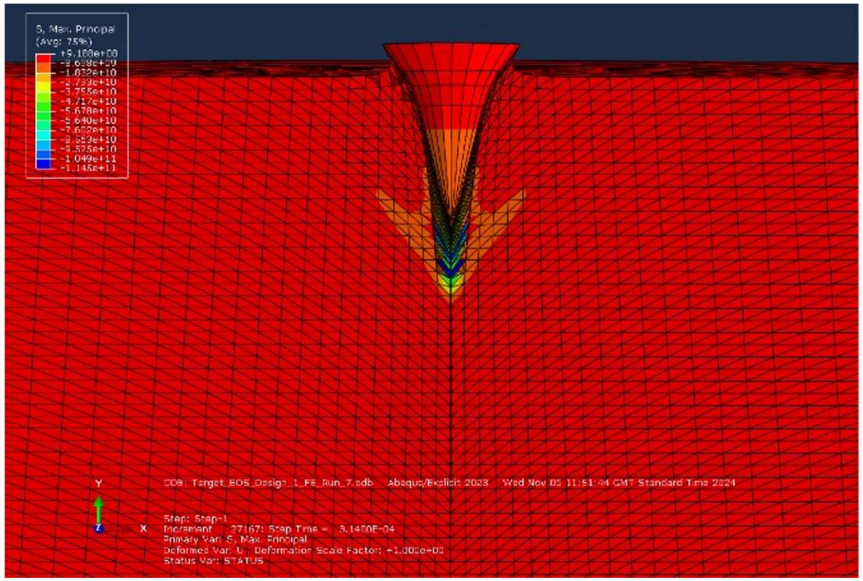
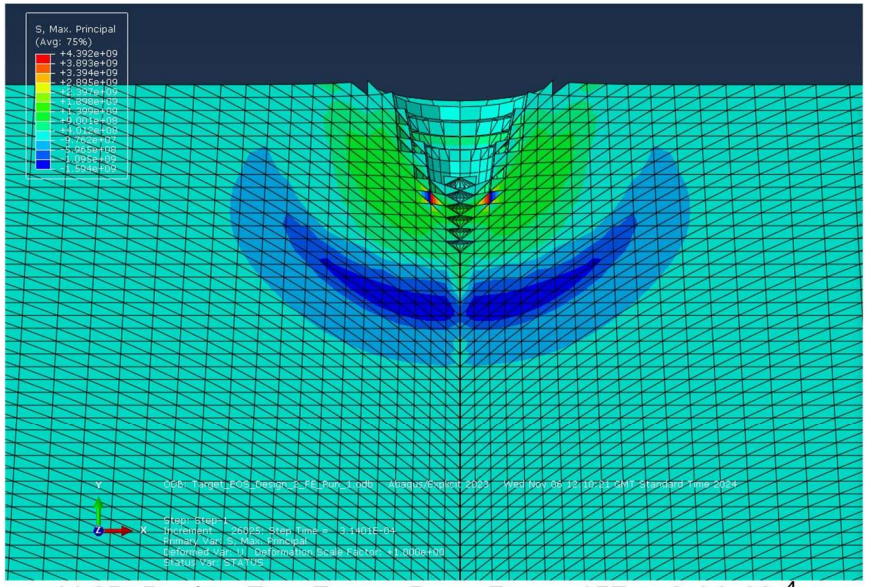


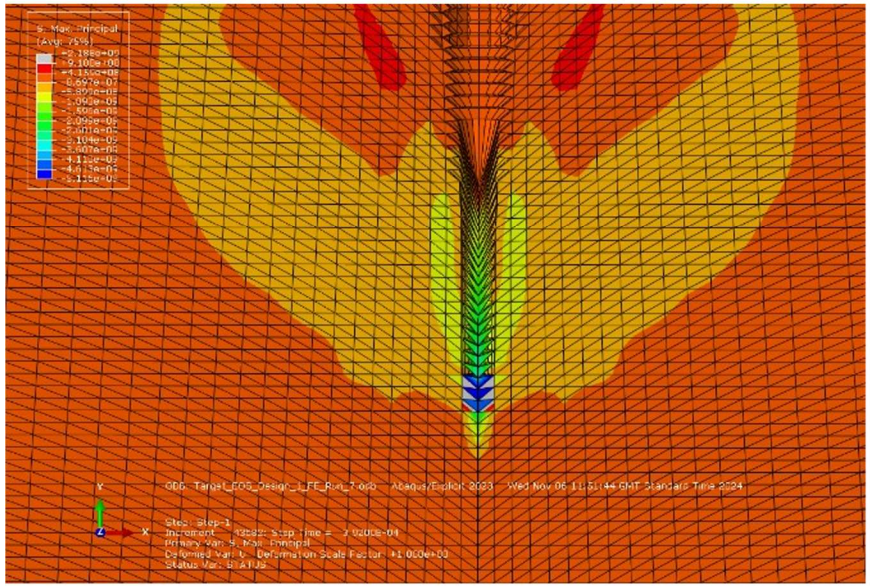
Figure 6-31 – 2D_Design_Two_Target_Run Jet Penetration Depth at a) 3.06x10 $^{-4}$s, b) 3.14x10 $^{-4}$s, c) 3.64x10 $^{-4}$s, d) 4.02x10 $^{-4}$s, e) 4.16x10 $^{-4}$s and f) 6.50x10 $^{-4}$s



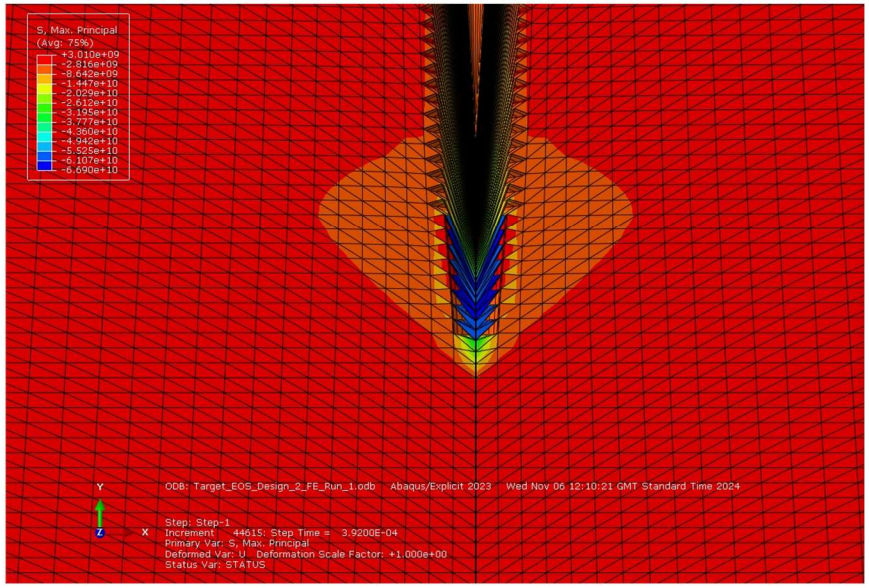
a) 2D_Design_One_Target_Run – Frame 157, t=3.14x10^{-4}s



b) 2D_Design_Two_Target_Run – Frame 157, t=3.14x10^{-4}s



c) 2D_Design_One_Target_Run – Frame 196, t=3.92x10^{-4}s



d) 2D_Design_Two_Target_Run – Frame 196, t=3.92x10^{-4}s

Figure 6-32 - Stress Comparison between 2D_Design_One_Target_Run and 2D_Design_Two_Target_Run

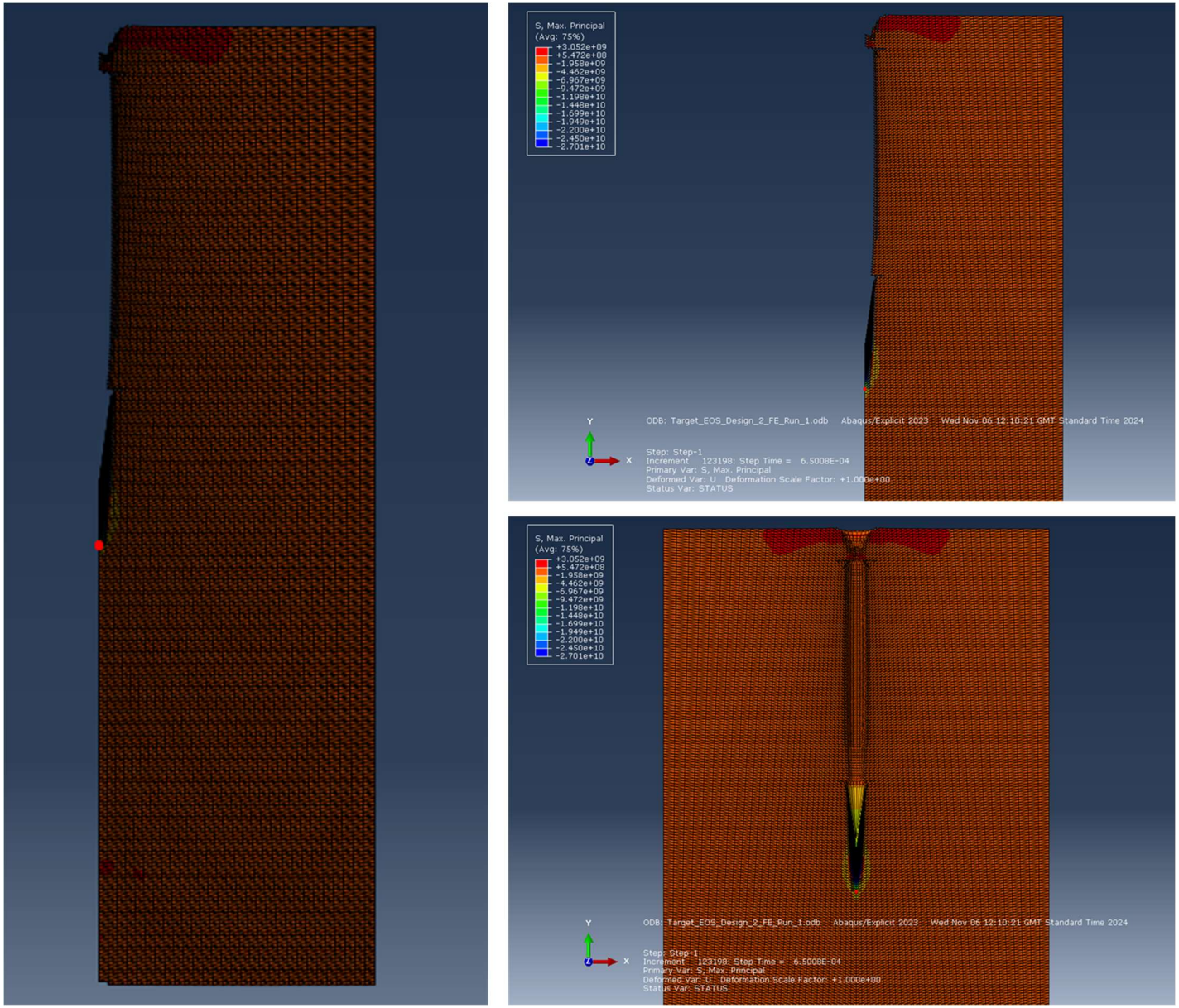
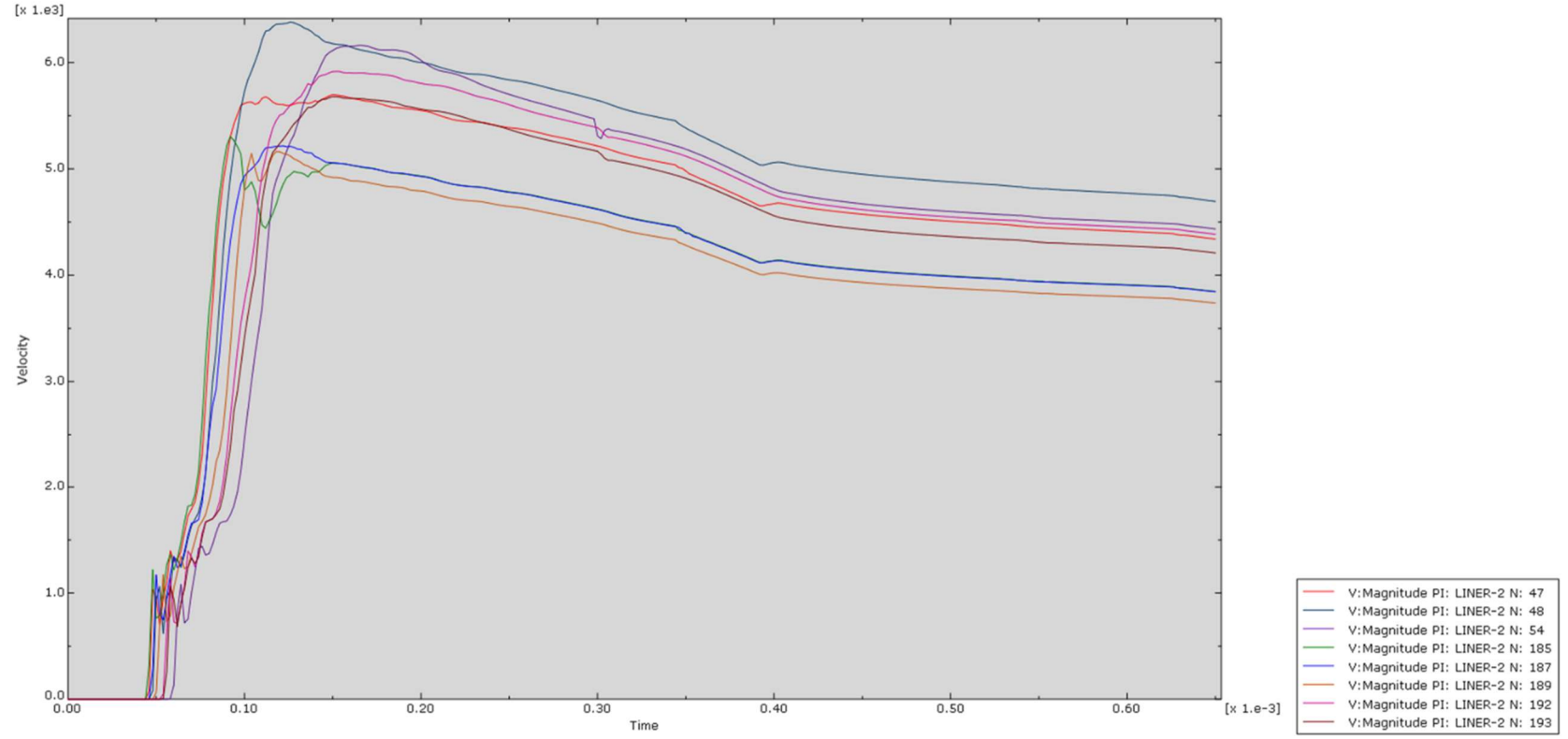
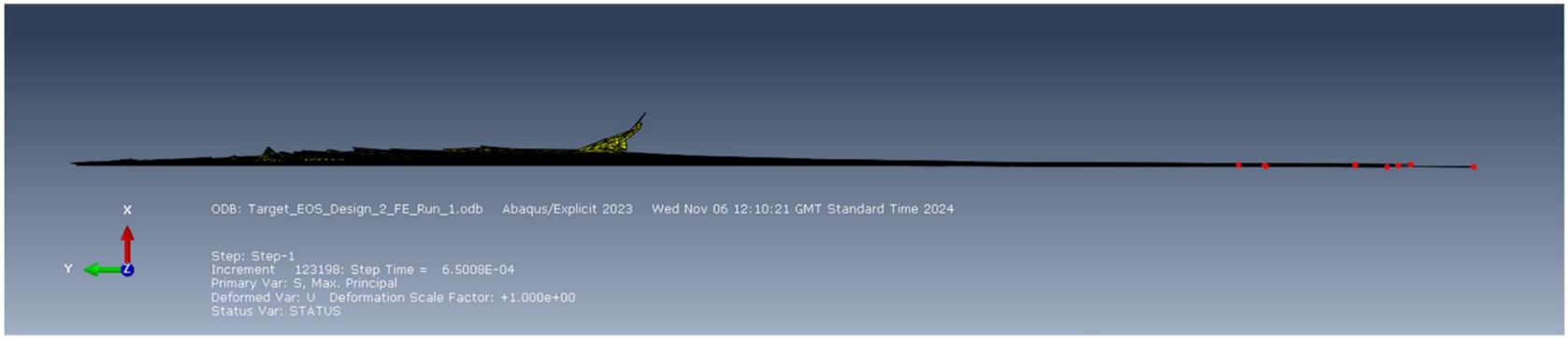


Figure 6-33 – 2D_Design_Two_Target_Run Final Penetration Depth



a) Velocity Time Graph



b) Selected nodes for Velocity Time Graph

Figure 6-34 - 2D_Design_Two_Target_Run Jet Tip a) Velocity Graph for b) Selected Nodes

7 3D Simulation

7.1 The 3D Model

Based on the results of the 2D designs, it was decided that Design One would be brought forward for further testing in 3D. The 3D model was created using the 2D Design One sketches to produce a 180° cross section of the shaped charge shown in Figure 7-1.

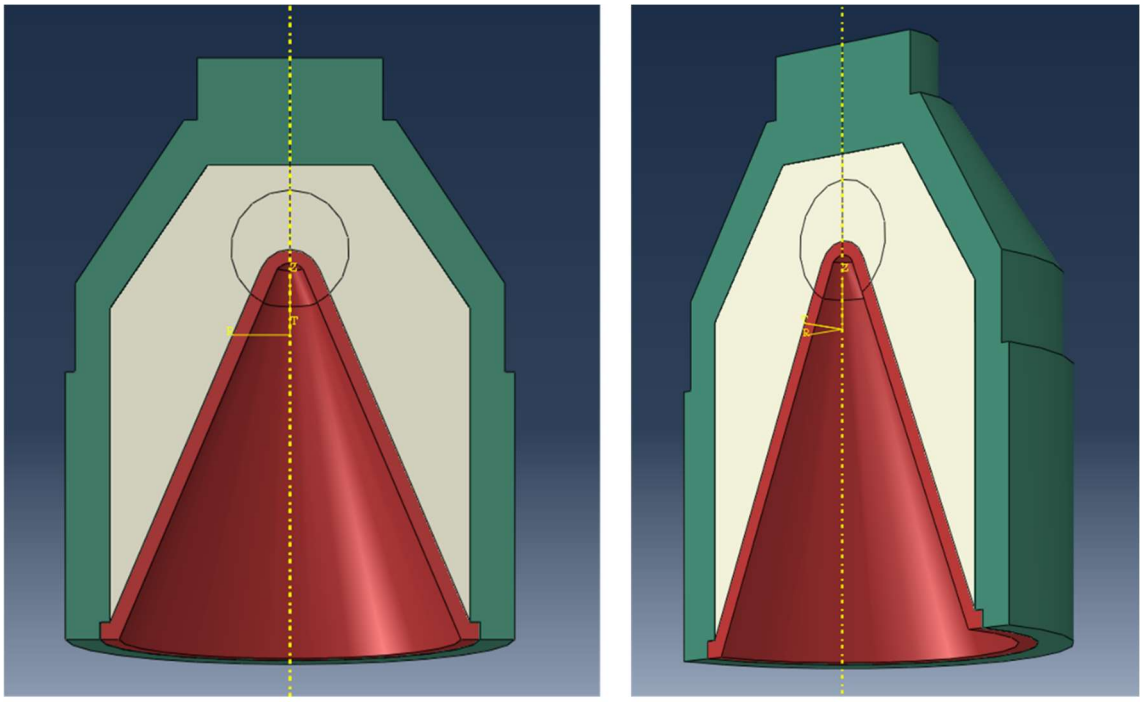


Figure 7-1 - Assembled 3D model of Design One

As with the 2D simulation the shaped charge was directed above a target, with the same dimensions as the 2D version, at a standoff distance of 1m. To provide a comparison, all 3D components have the same material properties as their 2D counterparts.

7.1.1 The 3D Mesh

The teaching version of Abaqus has a hard limit of 250,000 nodes, therefore, this places a restriction on the shape and complexity of the mesh. Due to the complex shape, a tetrahedral mesh was applied to all components of the design. To support detailed analysis, partitions in the model were created to enable more detailed zones of graduated mesh. Figure 7-2 shows the shaped charge's mesh, highlighting the partitions in the high explosive and around the apex of the liner. Figure 7-3 provides a detailed view of the mesh on the target showcasing its partition and gradual mesh.

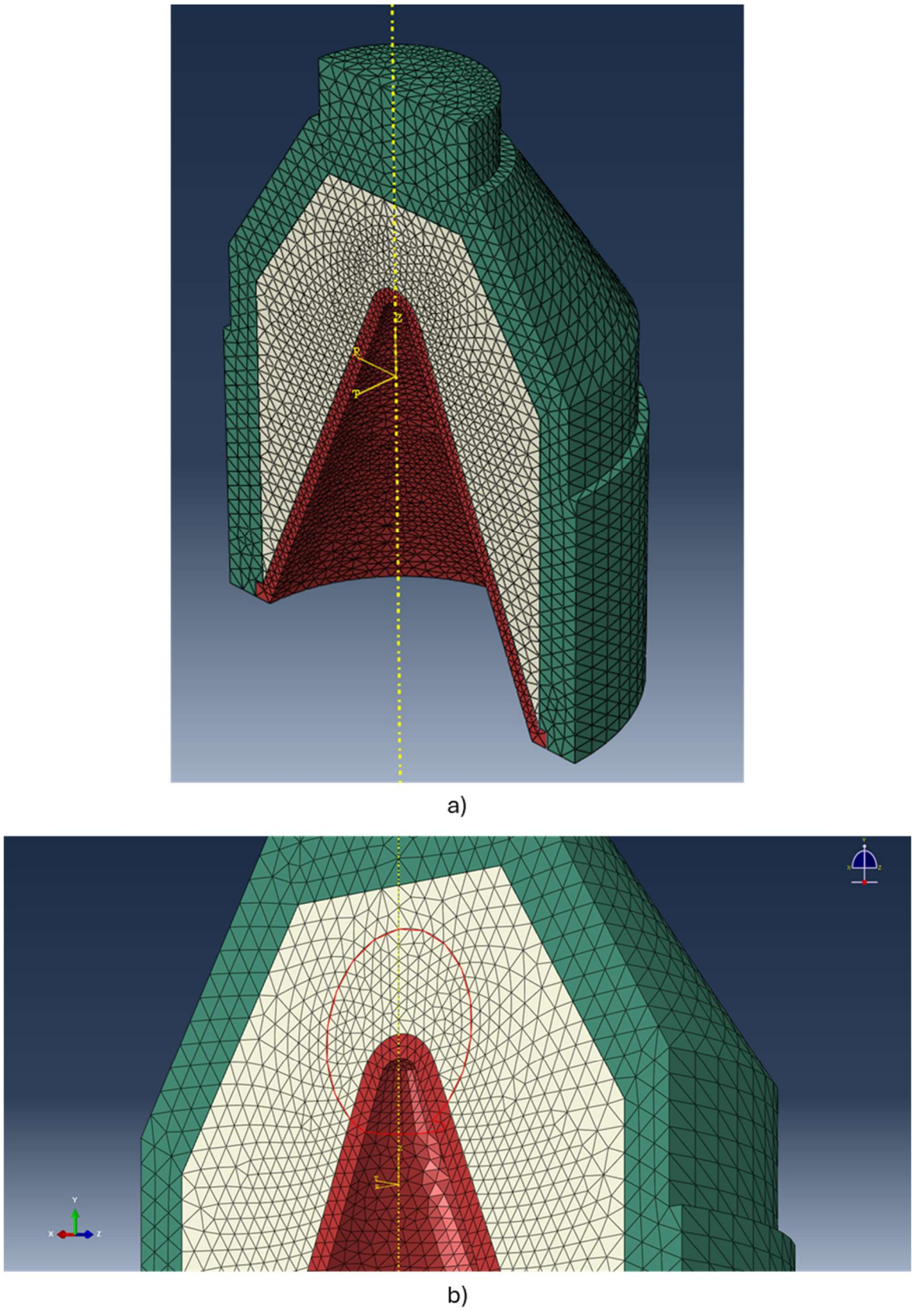


Figure 7-2 – The 3D Shaped Charge Design a) Assembled Mesh with b) The Partitions Highlighted

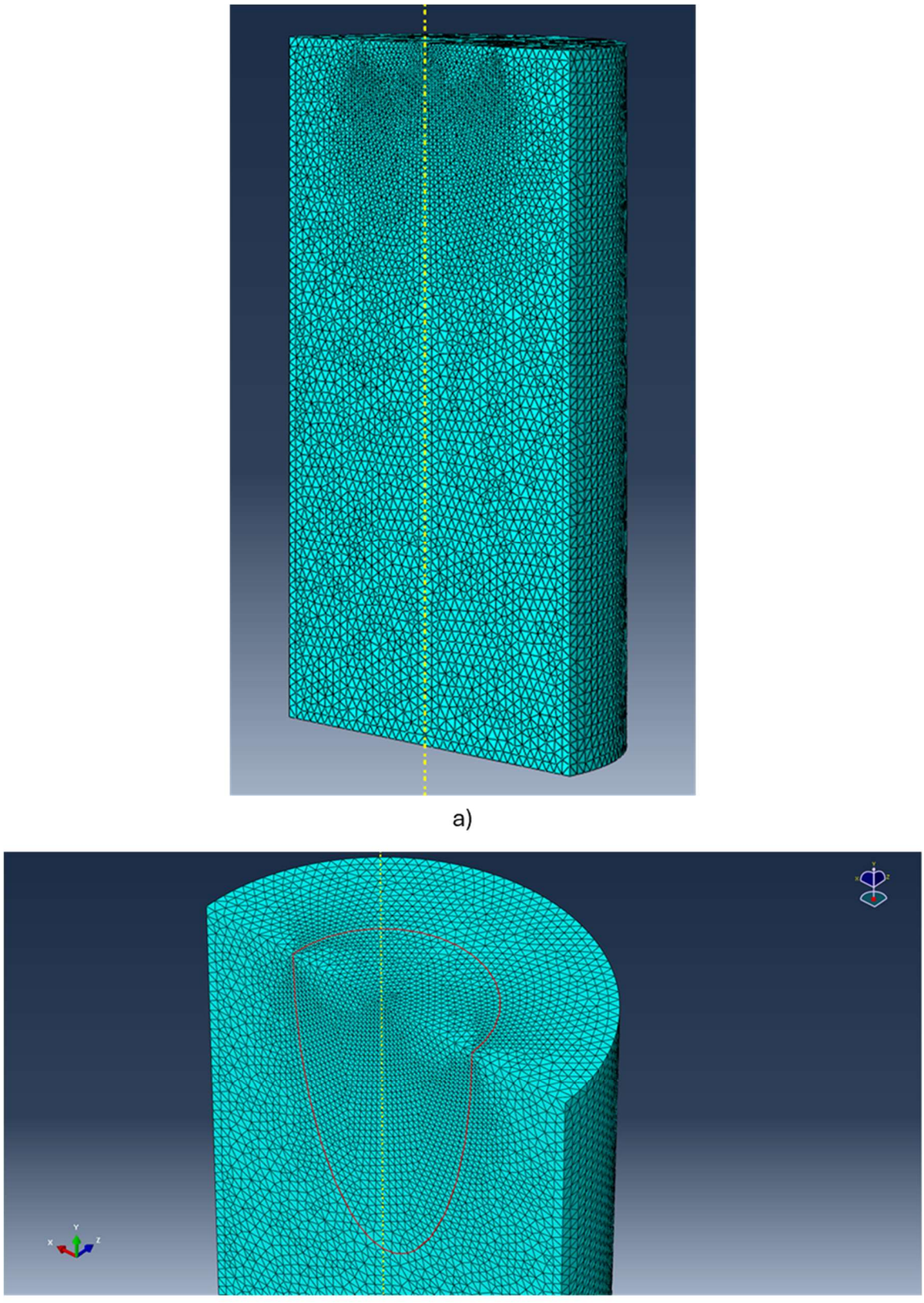


Figure 7-3 - The 3D Target Design a) Mesh with b) The Partitions Highlighted

7.1.2 3D Adaptive Mesh

Initially, to provide a baseline for further analysis and improvement, a standard mesh was applied to the model. With this mesh applied the simulation aborted after 2.5741×10^{-5}s due to excessively distorted elements with only 13 frames. These elements were in the High Explosive just above the apex liner as illustrated in Figure 7-4

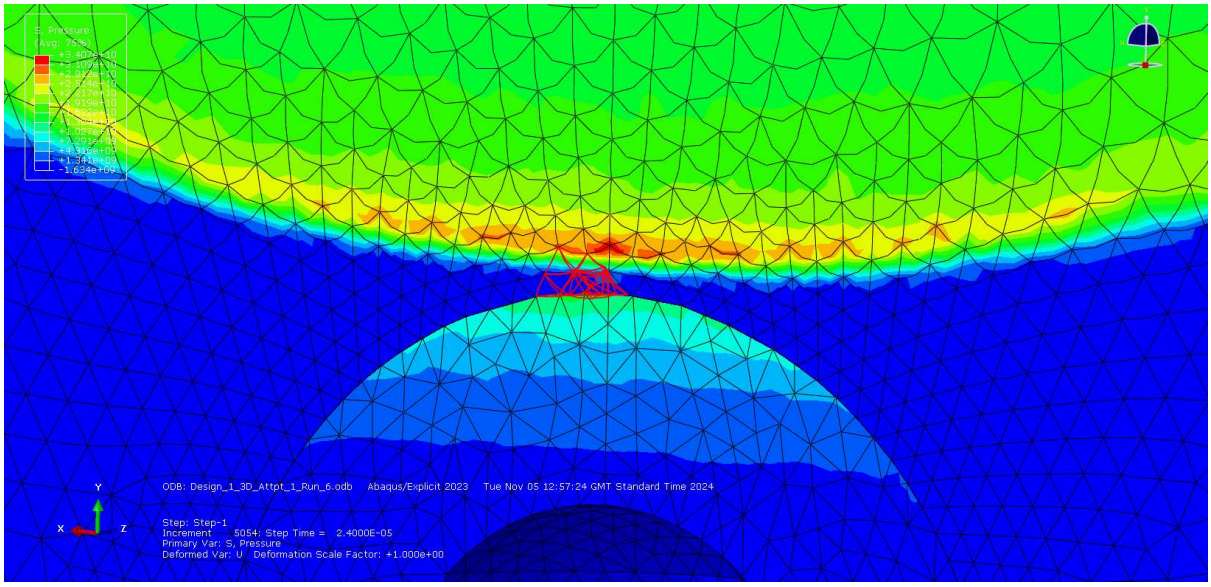


Figure 7-4 - 3D Model - Standard Mesh - Excessively Distorted Nodes

An adaptive mesh can be used in areas of the simulation where large deformations occur. During the simulation, the nodes are repositioned while the mesh properties stay the same [24].

Since the distorted nodes were above the apex of the liner, the adaptive mesh setting was applied to the smaller partitions created in the High Explosive and the liner. As there was no requirement for the mesh to be adaptive before the initial point of abortion, a second step was added to enable the adaptive mesh to start after 2.5×10^{-5}s.

Multiple runs of the simulation were conducted to assess and improve the performance of the adaptive mesh, each time increasing the frequency and sweep levels of the mesh. The run taken forward for analysis had a frequency value of 100000 and a sweep value of 10000.

7.2 3D Analysis

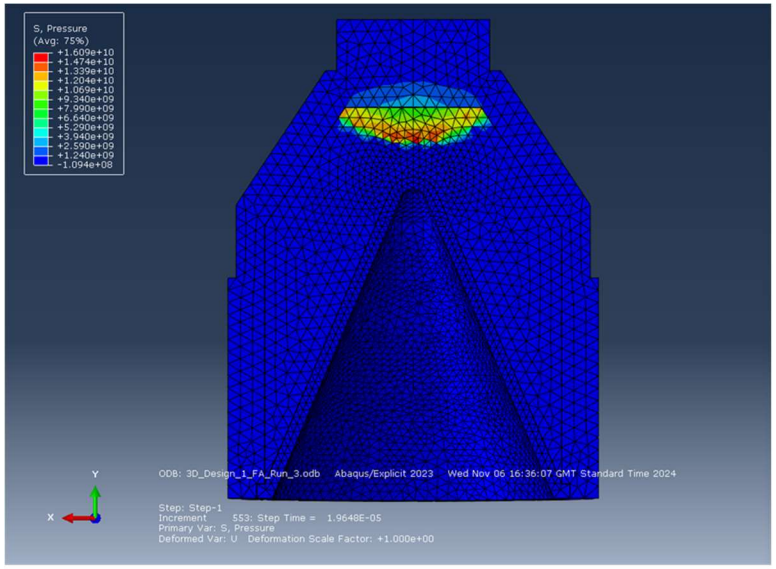
7.2.1 3D Jet Formation Analysis

The adaptive mesh simulation (3D_Design_Jet_Run) was initially conducted without the target to enable analysis on the jet formation. Step one completed successfully, while step two ran for 2.8648×10^{-5}s with an output of 143 frames and aborted due to an excessively distorted element in the liner. This element was in the section of the liner that did not have adaptive mesh applied.

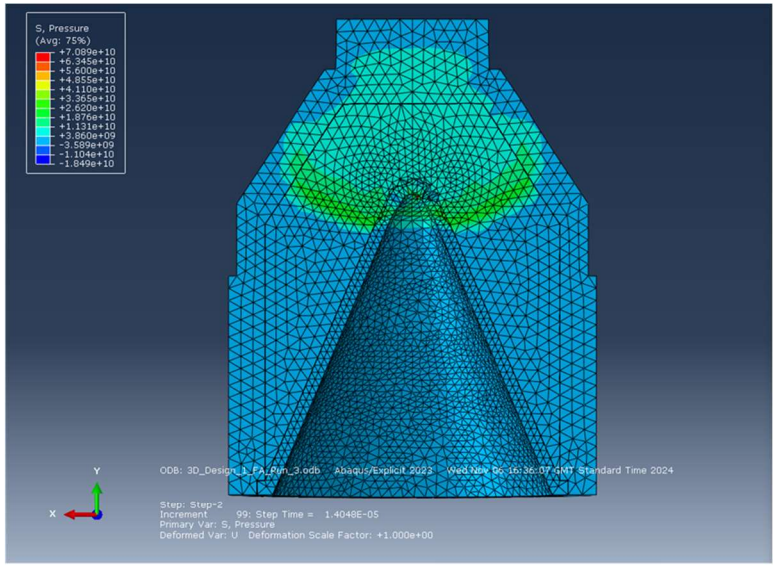
Any results that denote stress are shown in Max Principle to show the tensile and compressive stress and S23 to show the shear stress. In Max Principle, the negative values indicate stress due to compression and the positive due to tension.

Figure 7-5 shows how the pressure wave travelled through the explosive material, while Figure 7-6 shows the resulting tensile and compressive stress. It can be seen in Figure 7-7 that high pressure

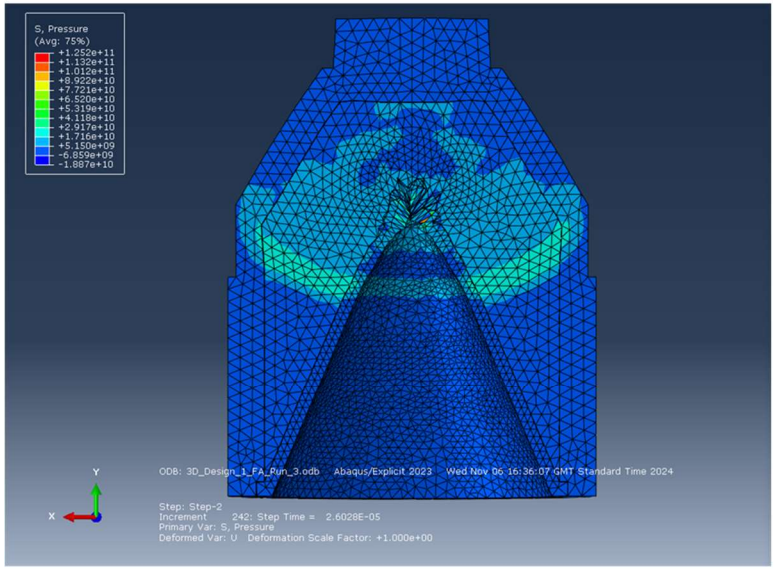
was exerted onto the apex of the liner as the detonation wave passes, in the region of 20-30GPa. This is different to the 2D simulations where the high levels of pressure were to the side of the apex. This variation could be accounted for with the extra explosive material present in the 3D simulation compared to the 2D. As the detonation wave continued to progress through the explosive material the inside of the liner experiences high pressures of 30-40GPa.



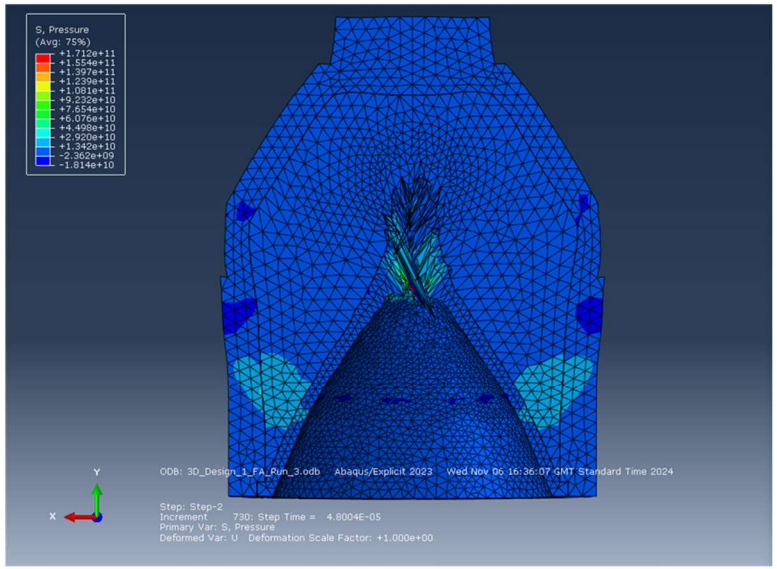
a) Step 1 Frame 491 at $1.9648x10^{-5}s$



b) Step 2 Frame 7 at $3.4048x10^{-5}s$



c) Step 2 Frame 13 at $4.6028x10^{-5}s$



d) Step 2 Frame 24 at $6.8005x10^{-5}s$

Figure 7-5 - 3D_Design_Jet_Run Results – Pressure Exerted From the Detonation Wave at a)1.9648x10 $^{-5}$s, b) 3.4048x10 $^{-5}$s, c) 4.6028x10 $^{-5}$s and d) 6.8005x10 $^{-5}$s

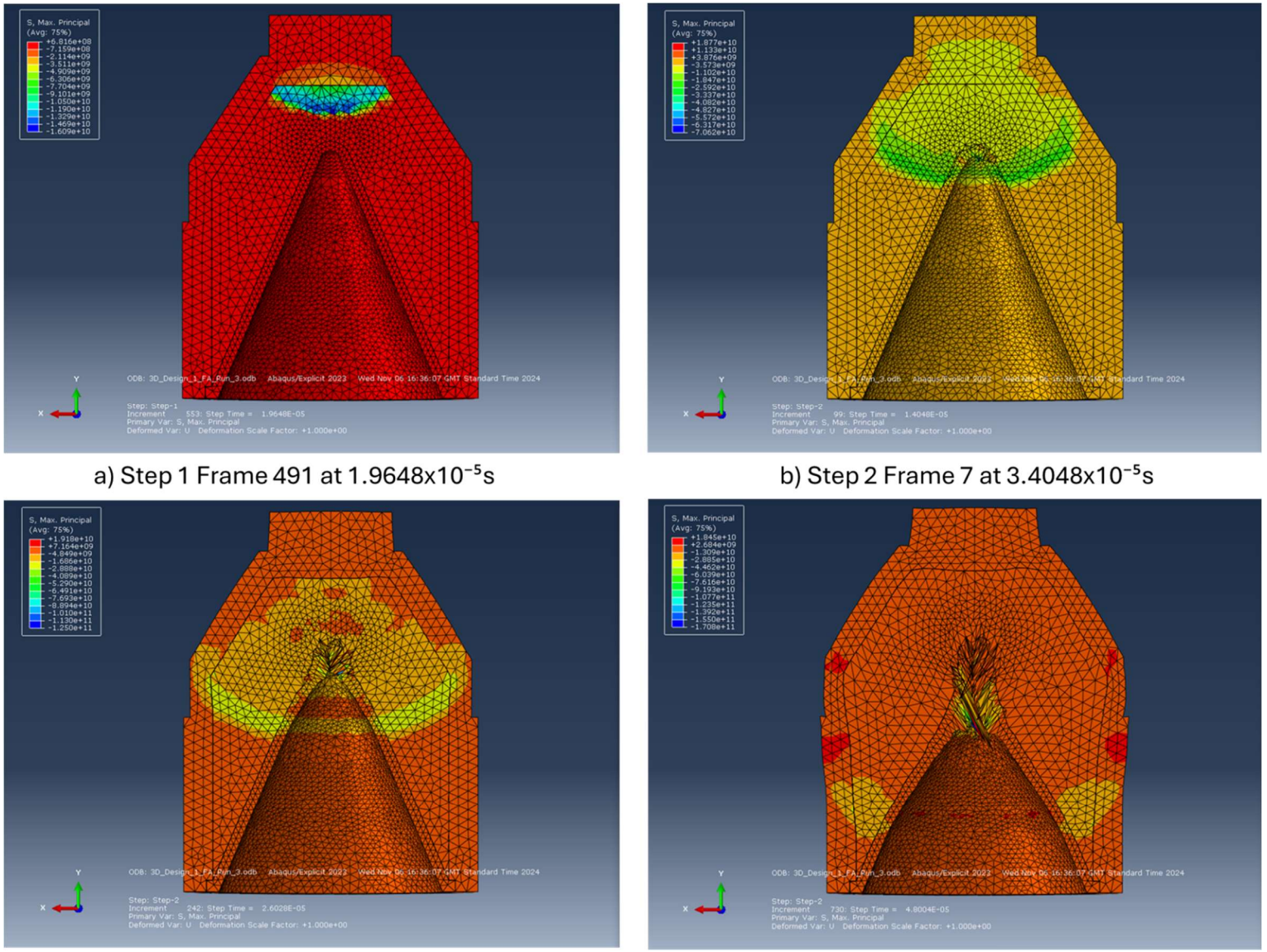
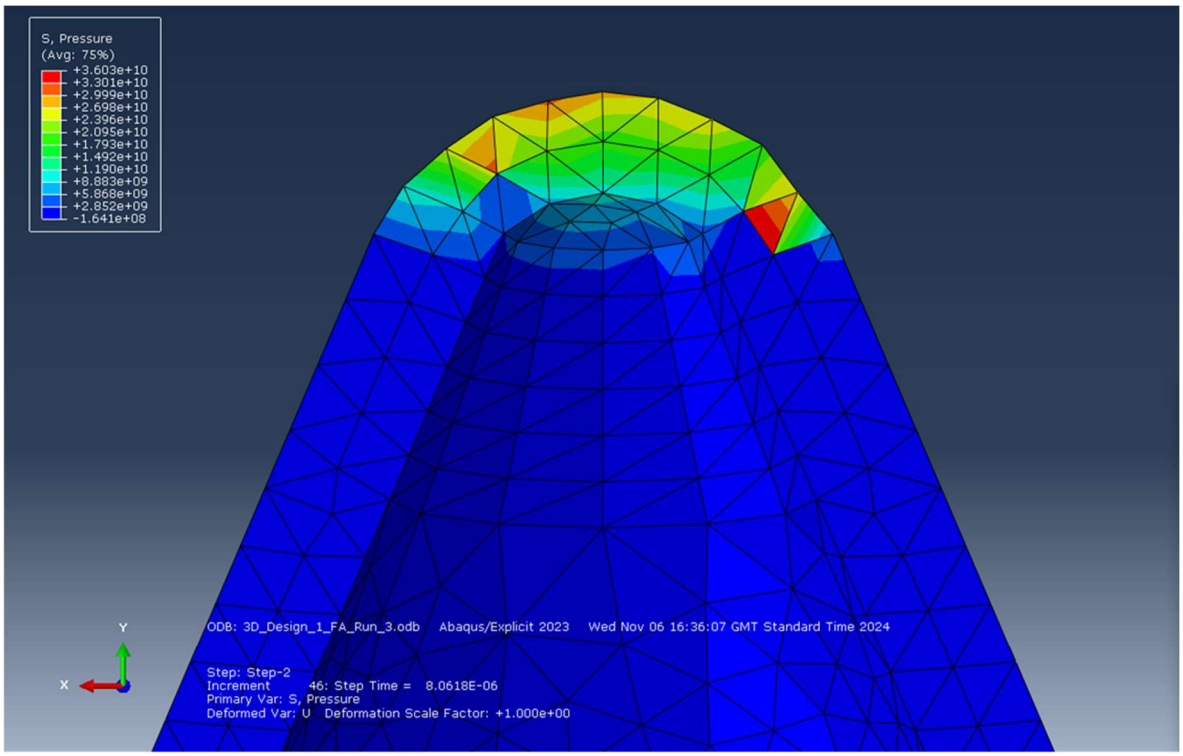
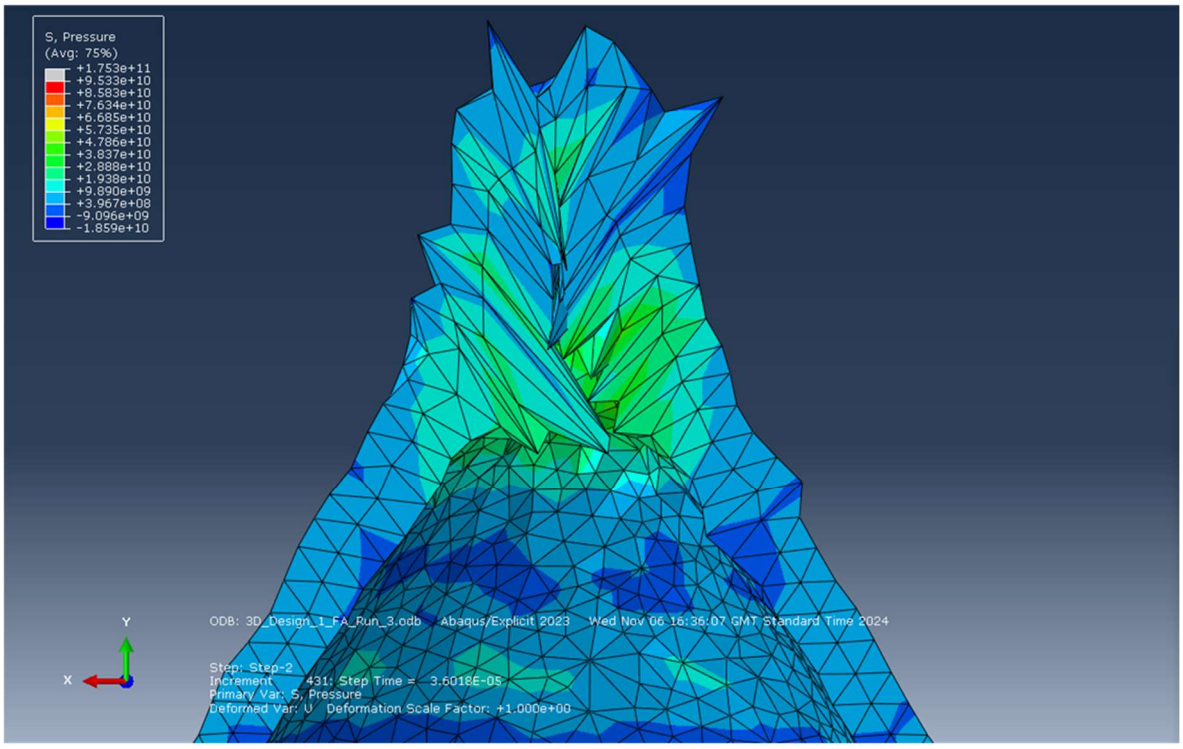


Figure 7-6 - 3D_Design_Jet_Run Results – Tensile and Compressive Stress Exerted From the Detonation Wave at a)1.9648x10 $^{-5}$s, b) 3.4048x10 $^{-5}$s, c) 4.6028x10 $^{-5}$s and d) 6.8005x10 $^{-5}$s.



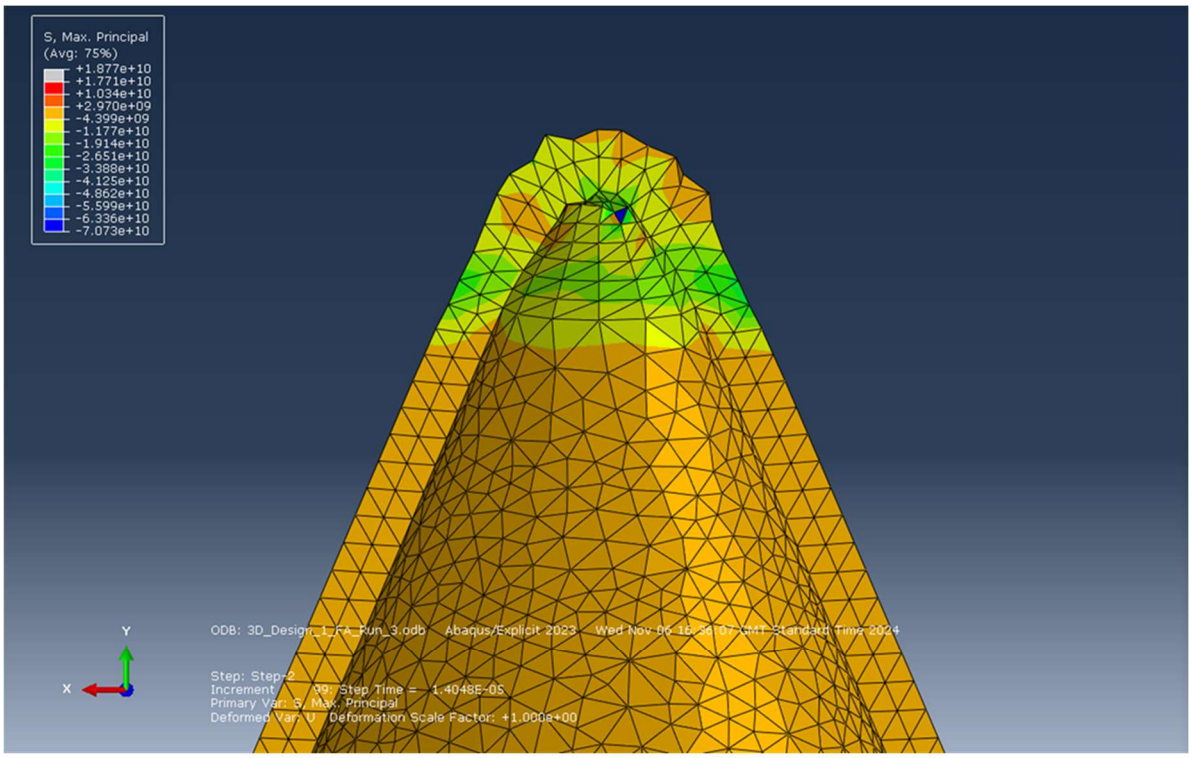
a) Step 2 Frame 4, time = 2.8062×10^{-5}s



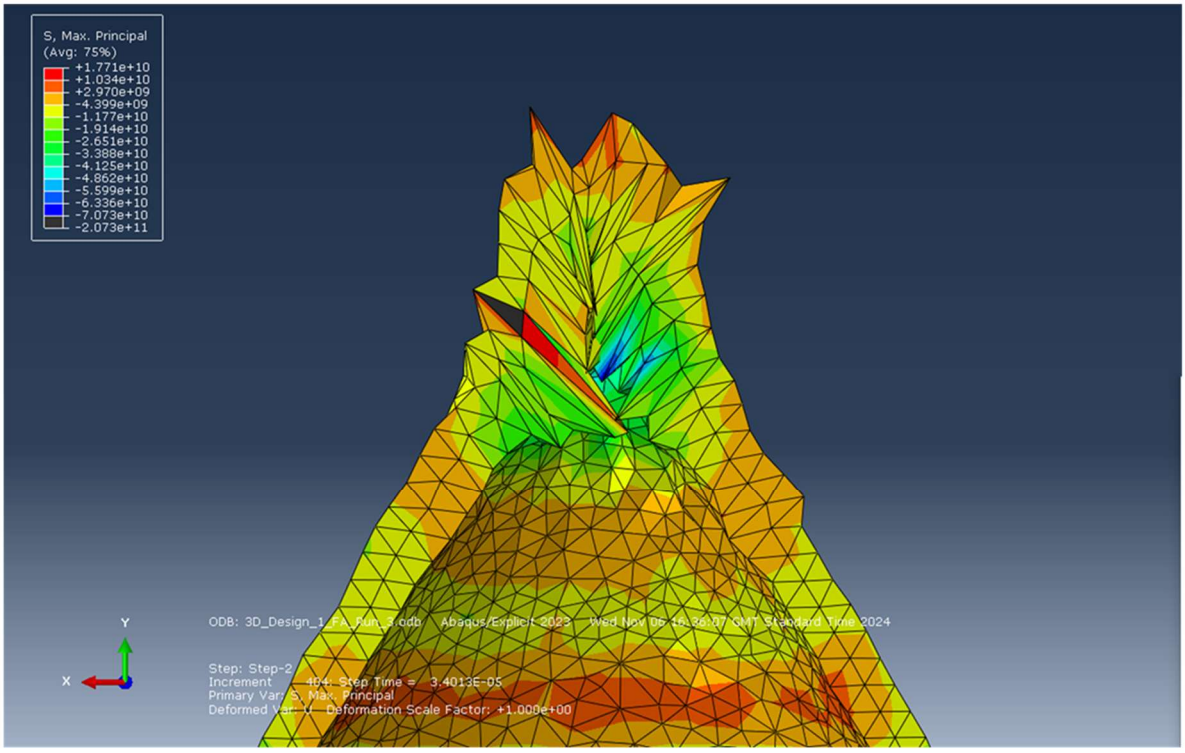
b) Step 2 Frame 18, time = 5.6018×10^{-5}s

Figure 7-7 - 3D_Design_Jet_Run Apex Pressure at a) 2.8062×10^{-5}s and b) 5.6018×10^{-5}s

As the liner compressed during the initial collapse, high compressive stresses of 20-30GPa originated from the external side of the liner and moved to the inside as the collapse progressed. This is represented by the green colouring in Figure 7-8.



a) Step 2 Frame 7, time = 3.4048×10^{-5}s



b) Step 2 Frame 17, time = 5.4013×10^{-5}s

Figure 7-8 - 3D_Design_Jet_Run Compressive Stress at a) 3.4048×10^{-5}s and b) 5.6018×10^{-5}s

The liner collapsed to form a jet as presented in Figure 7-9. A shaped charge with a conical liner typically has a thin elongated jet [4, 6, 10]. Up until the last few frames the simulation was producing the expected jet formation, however, the result is a jet that appears to have a similar thickness from the slug to the tip. Figure 7-10 shows the length of the jet was approximately 1.2m

and the nodes that make up the tip of the jet originate from the middle of the liner rather than the apex. The resulting jet thickness varies from that of the 2D simulations. The thicker jet in 3D_Design_Jet_Run could be a result of the higher number of nodes available and the increased mass present in the liner. The tip had an average velocity of 5.5kms^{-1}, shown in Figure 7-11 , which is faster than the 2D simulations.

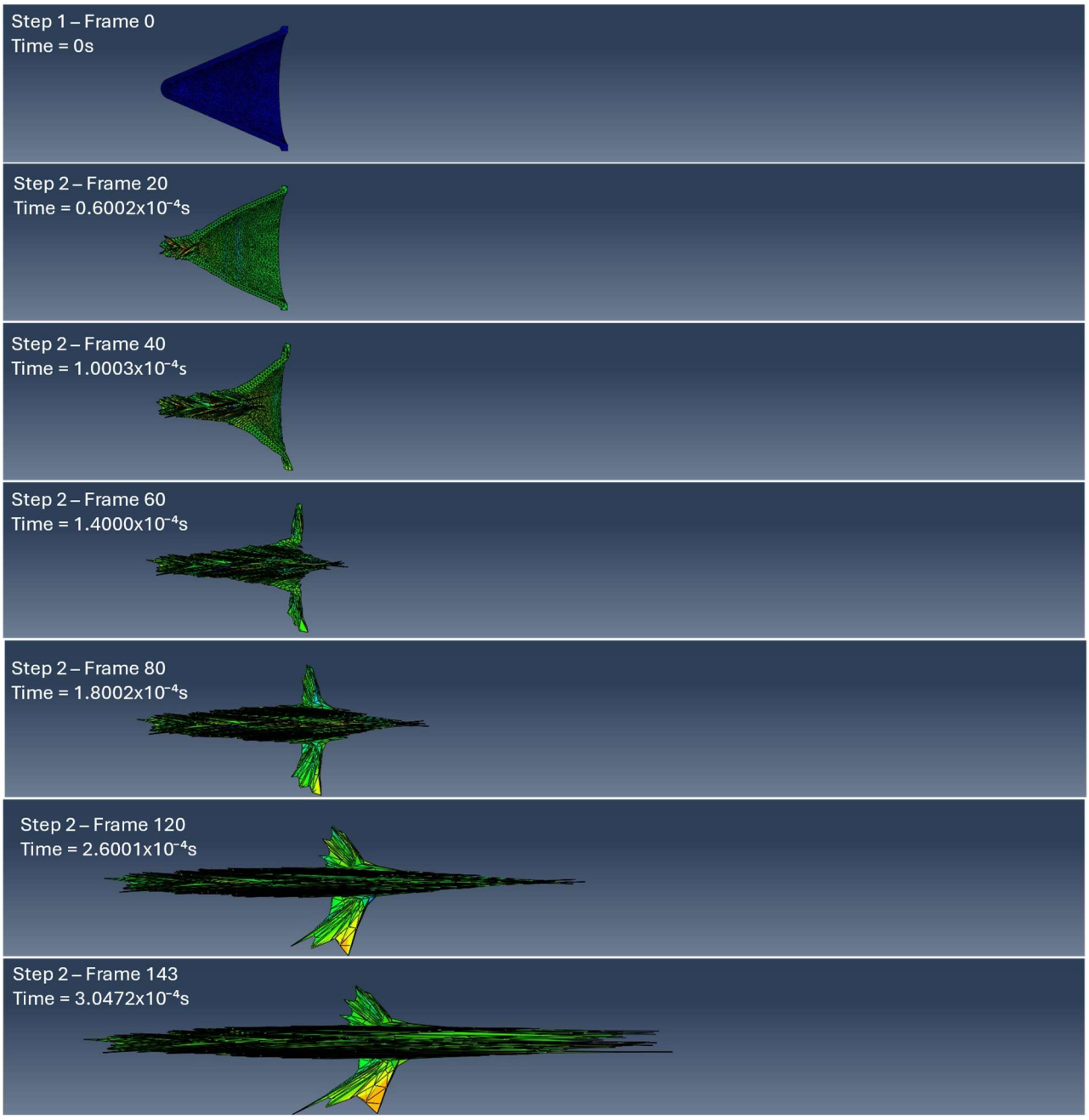
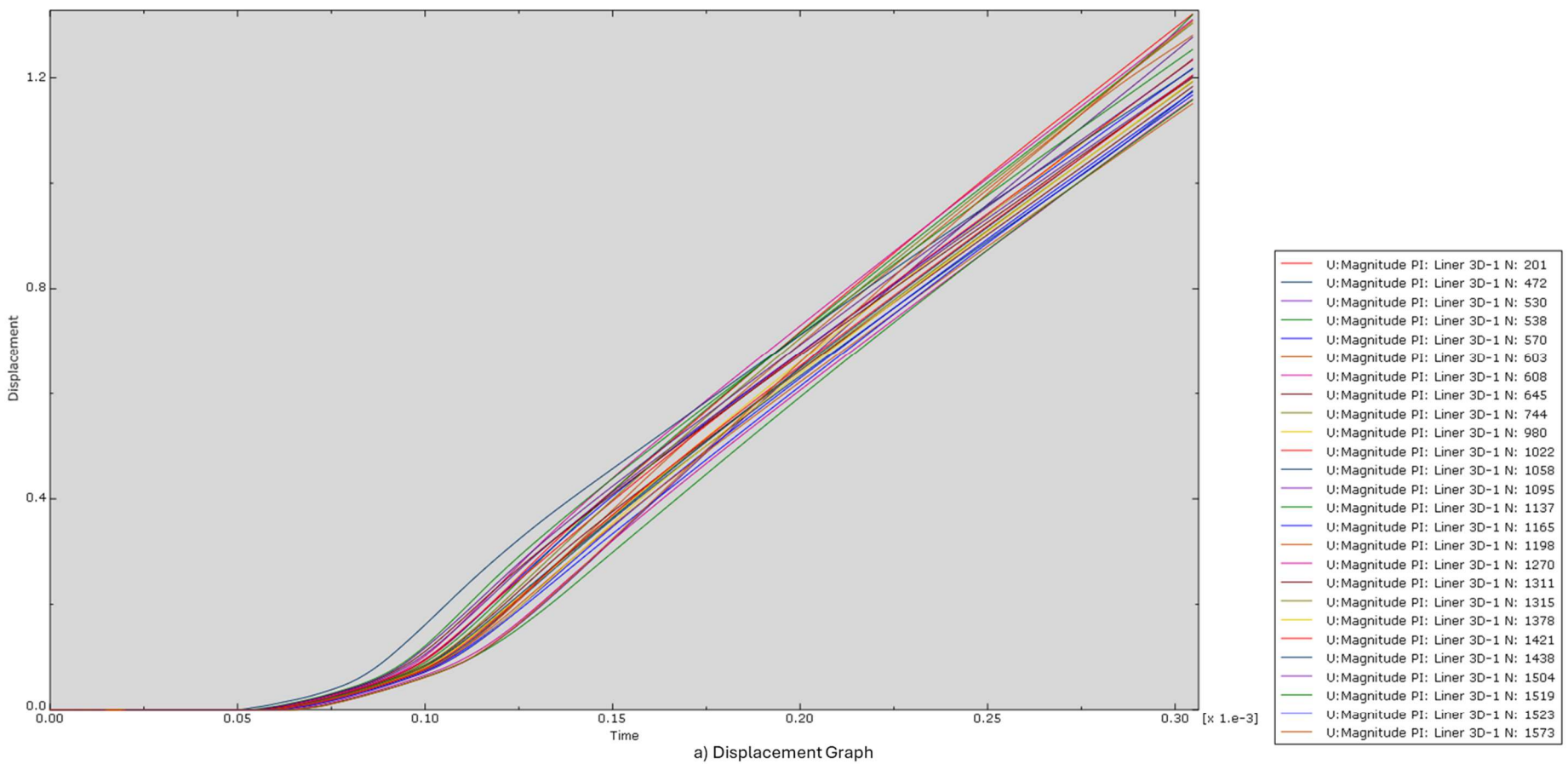


Figure 7-9 - 3D_Design_Jet_Run Jet Formation from Liner Collapse to Abortion



a) Displacement Graph

b) Selected nodes for Displacement Graph

Figure 7-10 - 3D_Design_Jet_Run a) Displacement Graph with b) Selected Nodes

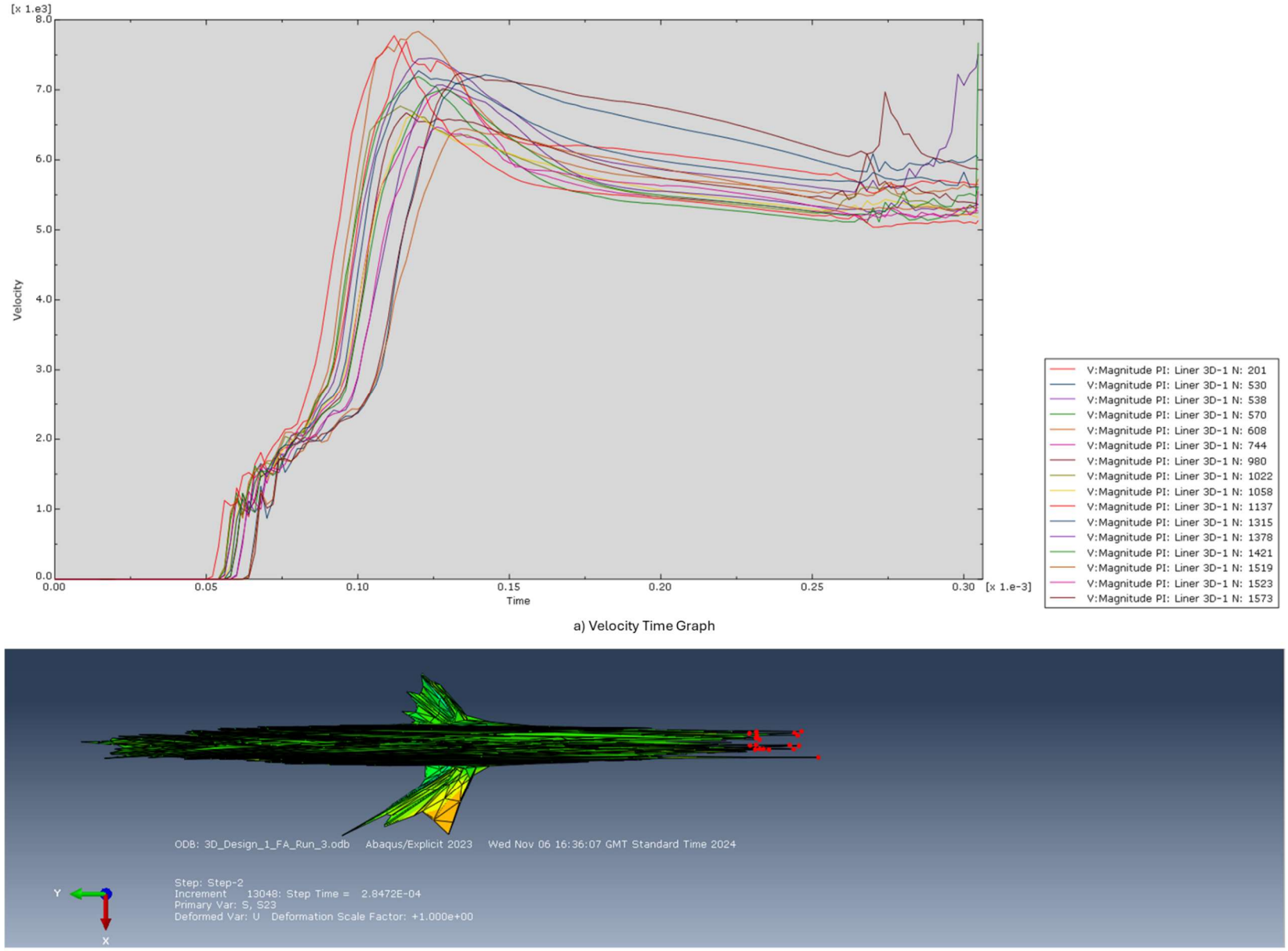


Figure 7-11 -3D_Design_Jet_Run a) Velocity Graph During Jet Formation with b) Selected Nodes

7.2.2 3D Target Penetration Analysis

7.2.2.1 Initial 3D Target Penetration Simulation Analysis

To provide a comparison to the 2D simulation, the 3D simulation previously analysed was repeated with the metal target. An initial test mesh, shown in Figure 7-12, was used for the target to provide a baseline for the penetration analysis.

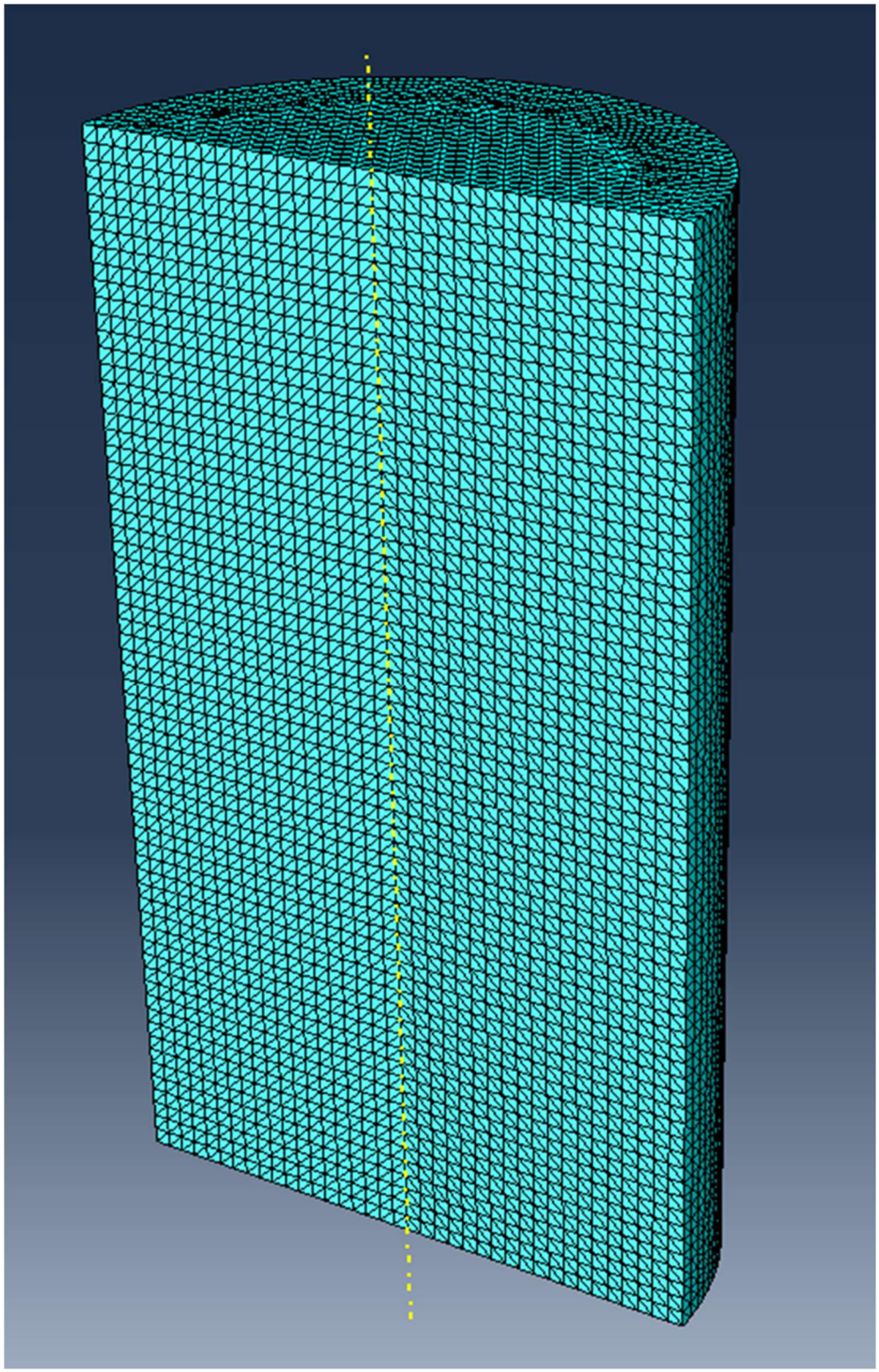


Figure 7-12 - Initial Target 3D mesh

This simulation (3D_Design_Target_Run_1) aborted 2.8831×10^{-4}s into step two with an output of 145 frames, due to an excessively distorted node in the liner, in a similar location to 3D_Design_Jet_Run.

The jet was formed in the same manner as 3D_Design_Jet_Run to produce a thick jet of approximately 1.2m travelling at $5.5 kms^{-1}$. This jet formation is shown in Figure 7-13 while, Figure 7-14 and Figure 7-15 show the respective displacement and velocity graphs. It is evident that at the point of abortion, the thickness was constant from the slug to the tip, with some elements moving away from the main body of the jet, which is not seen in the previous run.

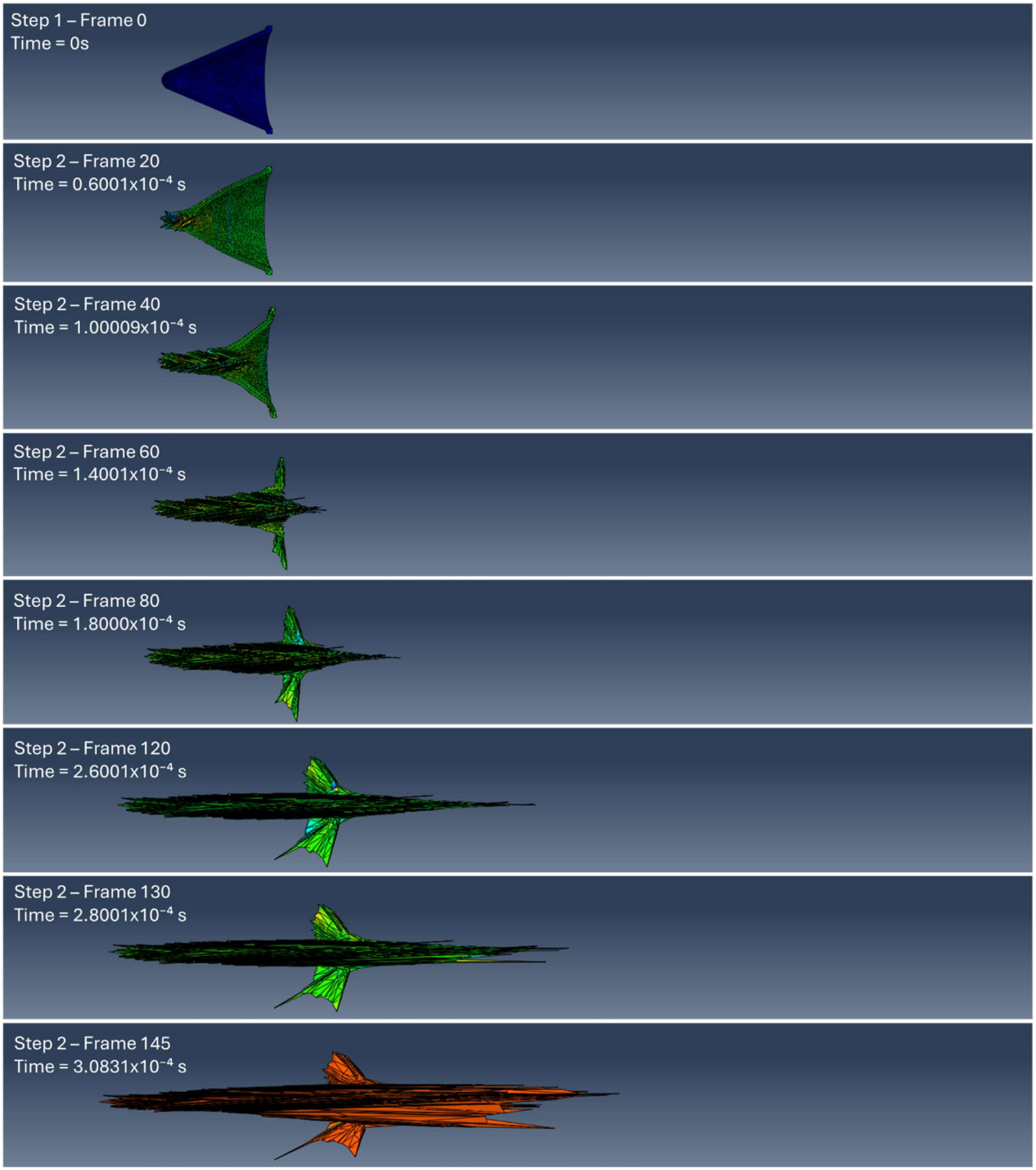
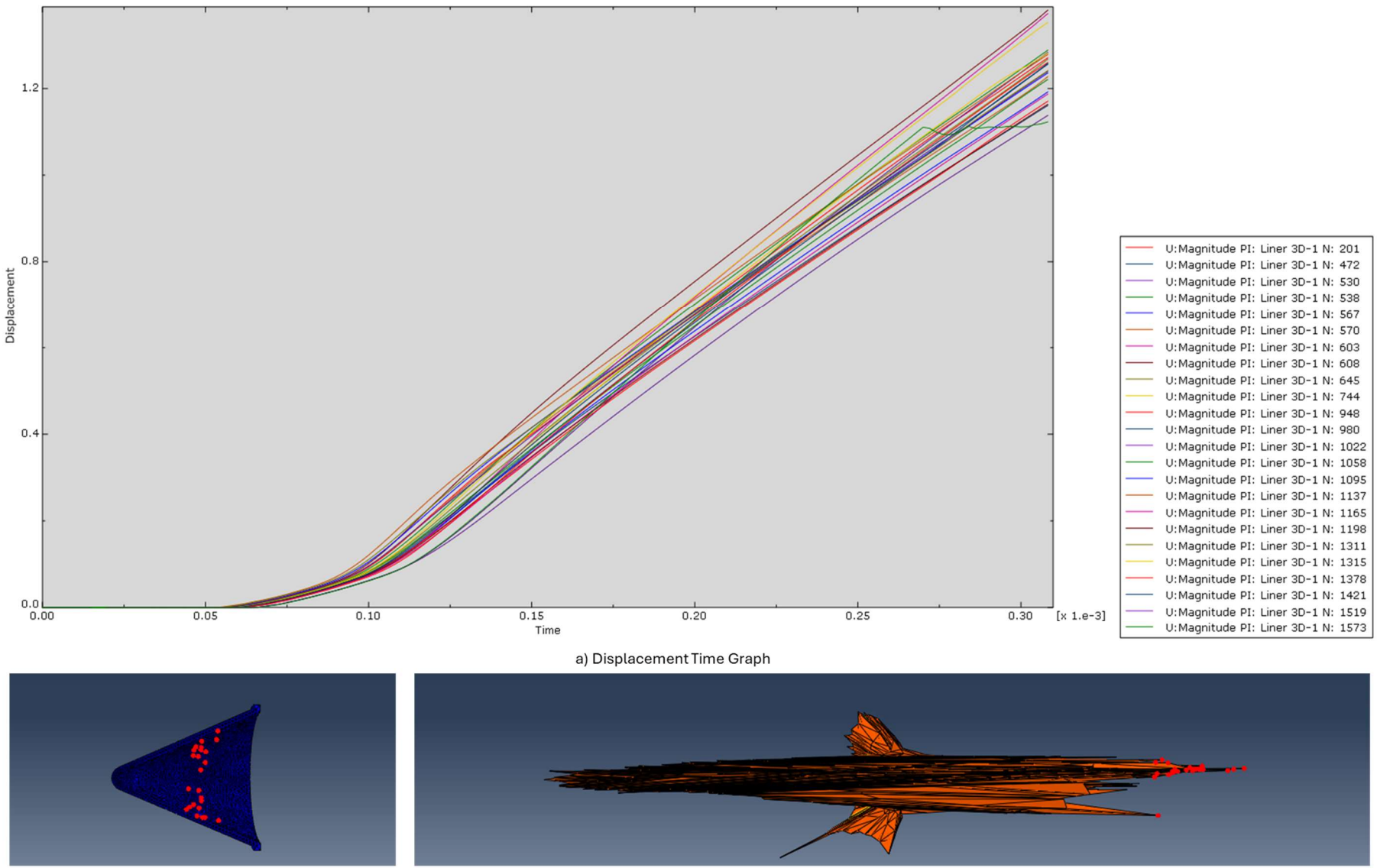


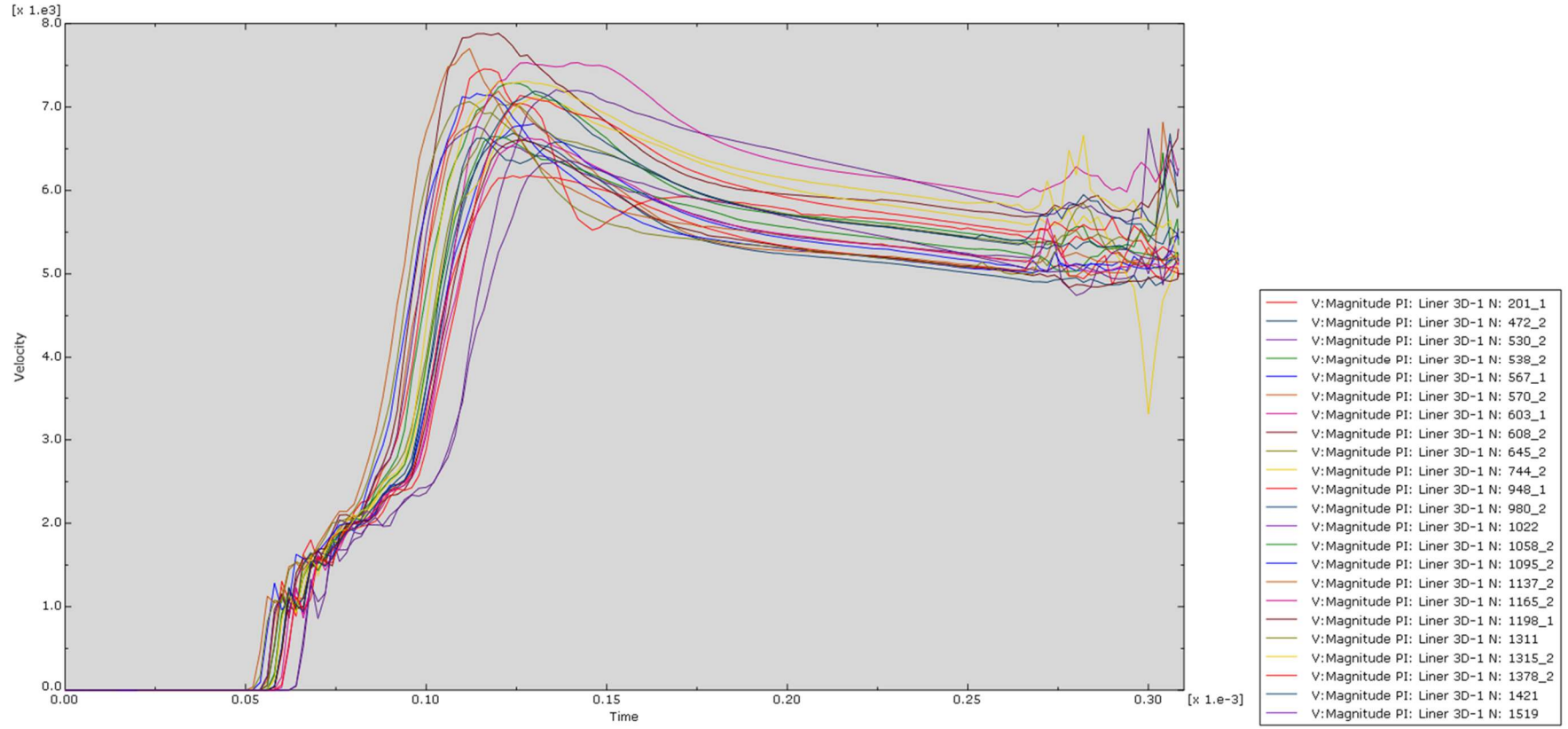
Figure 7-13 - 3D_Design_Target_Run_1 Jet Formation from Liner Collapse to Point of Abortion



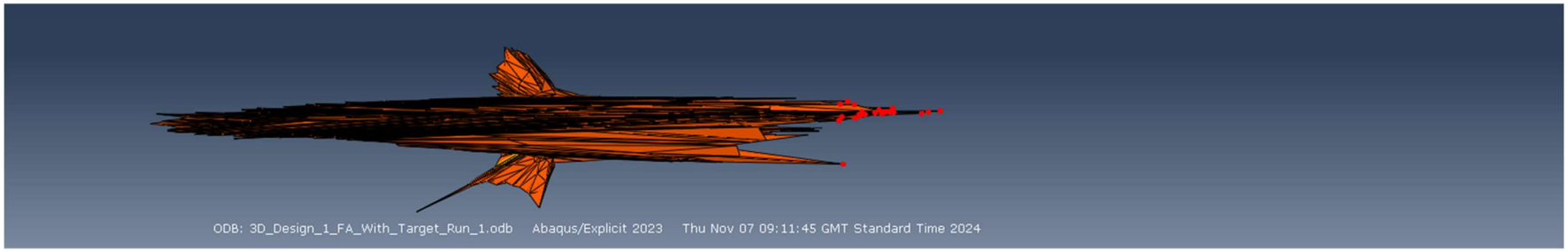
a) Displacement Time Graph

b) Selected nodes for Displacement Time Graph

Figure 7-14 - 3D_Design_Target_Run_1 a) Displacement Graph with b) Selected Nodes



a) Velocity Time Graph



b) Selected nodes for Velocity Time Graph

Figure 7-15 - 3D_Design_Target_Run_1 a) Velocity Graph with b) Selected Nodes

Effects from the jet interacting with the target can be seen from 2.72 x10^{-4}s with element deletion occurring at 2.78 x10^{-4}s. This deletion, shown in Figure 7-16, appears to be the result of high compression in the region of 5.45x10^{11}Pa. This significant damage seems abnormally severe considering that only a small portion of the jet has reached the target.

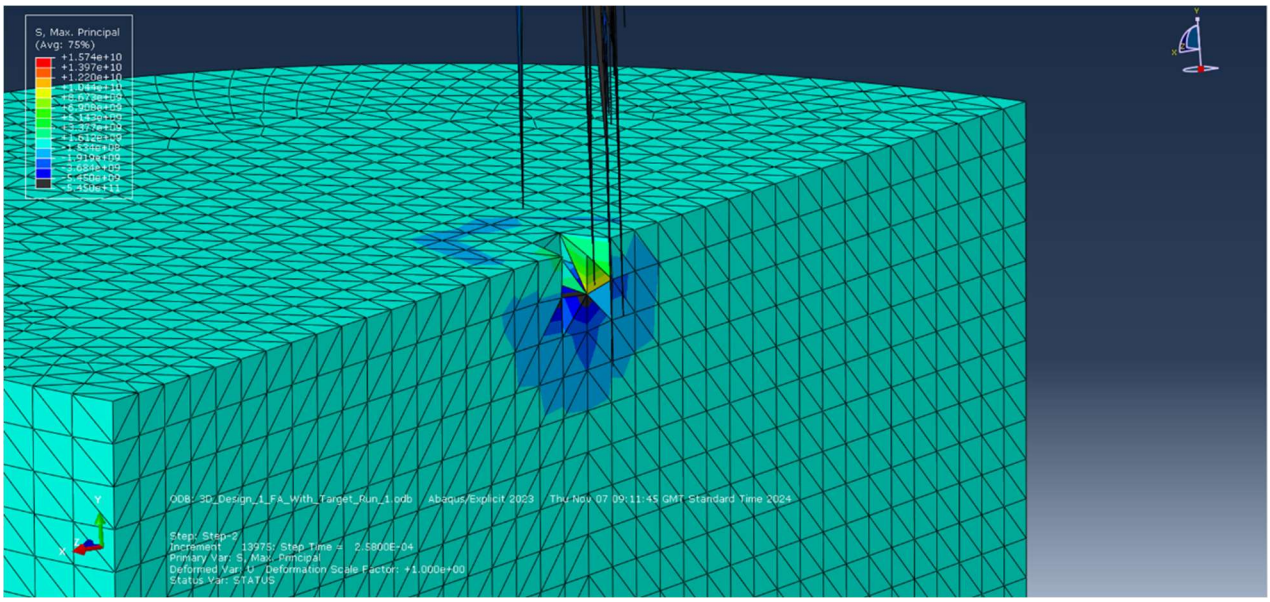
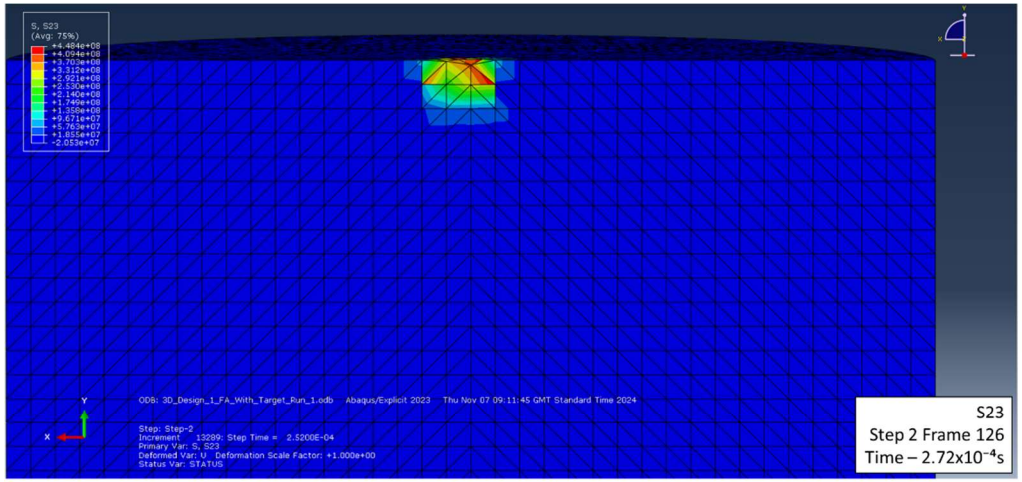
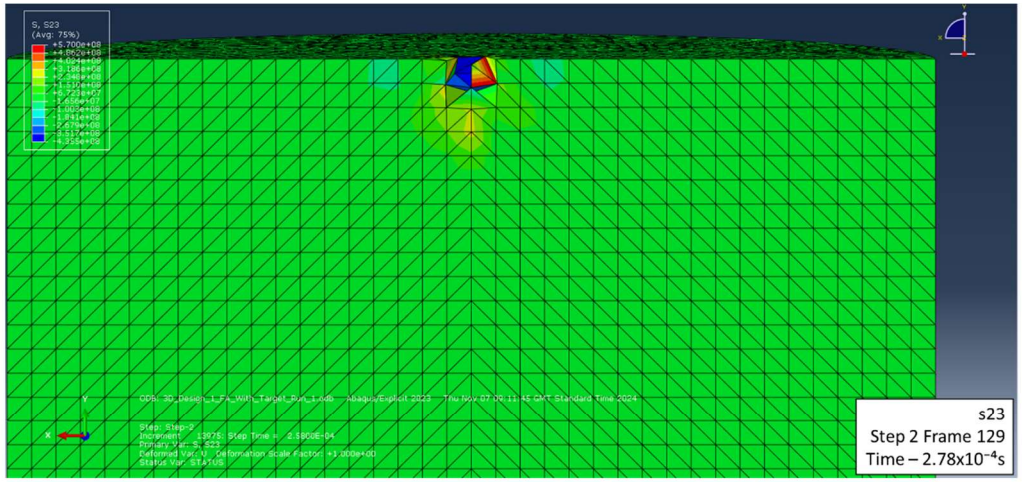


Figure 7-16 - 3D_Design_Target_Run_1 Initial Target element deletion at 2.78x10 $^{-4}$s.

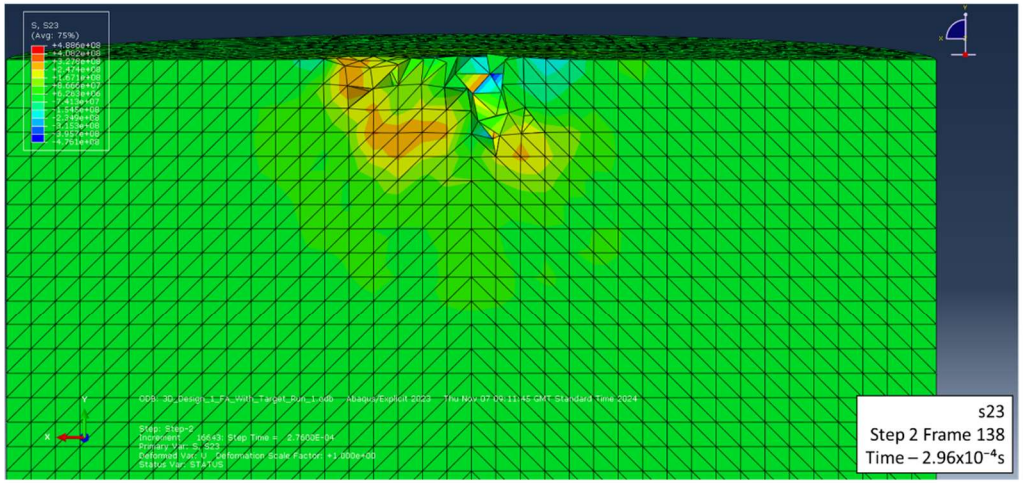
Figure 7-17 and Figure 7-18 present how the liner penetrated the target from initial contact to point of abortion, showcasing the Shear stress and Max Principal stress respectively. The liner has been removed to aid with the visualisation. As shown by the yellow-orange red colour ahead of the liner in Figure 7-17**Error! Reference source not found.**, a stress wave travelled through the target, exerting shear stress of approximately 0.15-0.20GPa. Comparatively, the compressive stresses, shown in Figure 7-18,are in the region of 5-10GPa, indicating that compressive rather than shear stress is causing the most damage to the target.



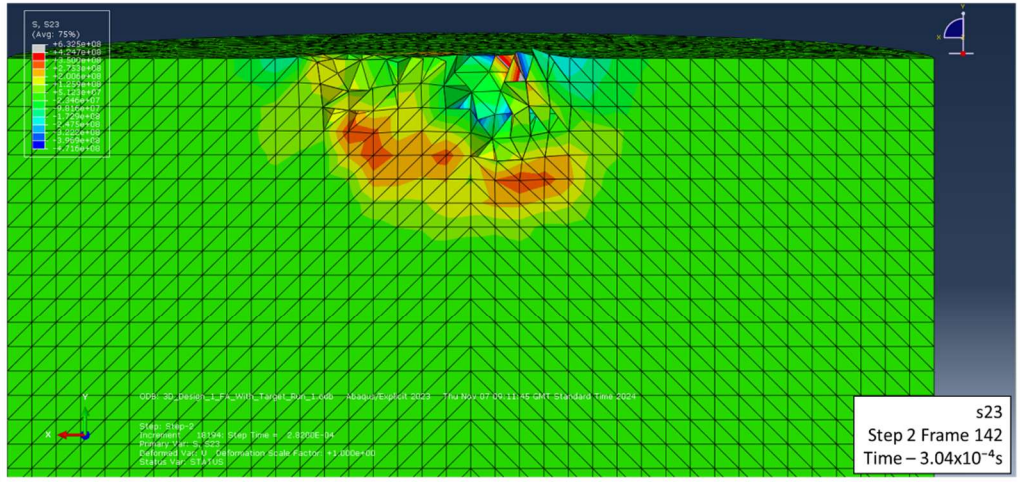
a) Step Two Frame 126, Time = 2.72×10^{-4}s



b) Step Two Frame 129, Time = 2.78×10^{-4}s

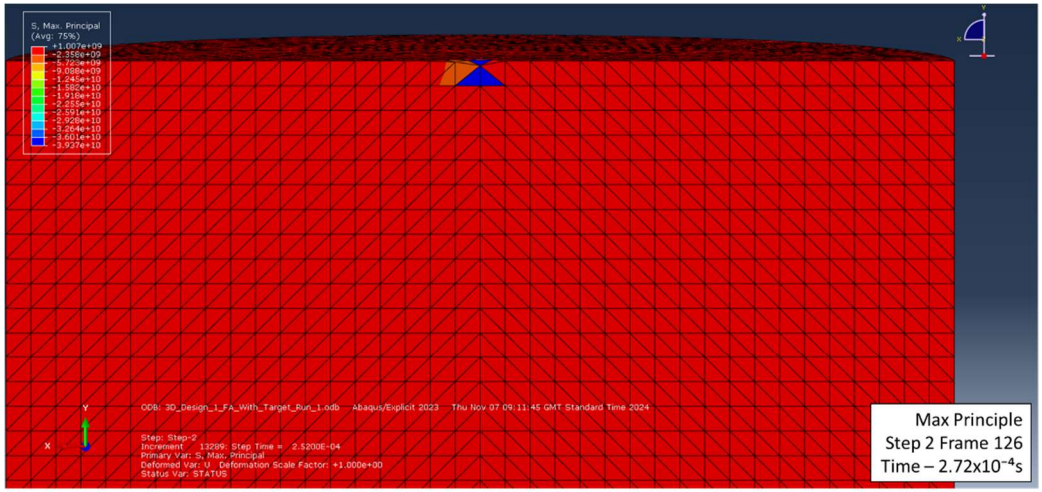


c) Step Two Frame 138, Time = 2.96×10^{-4}s

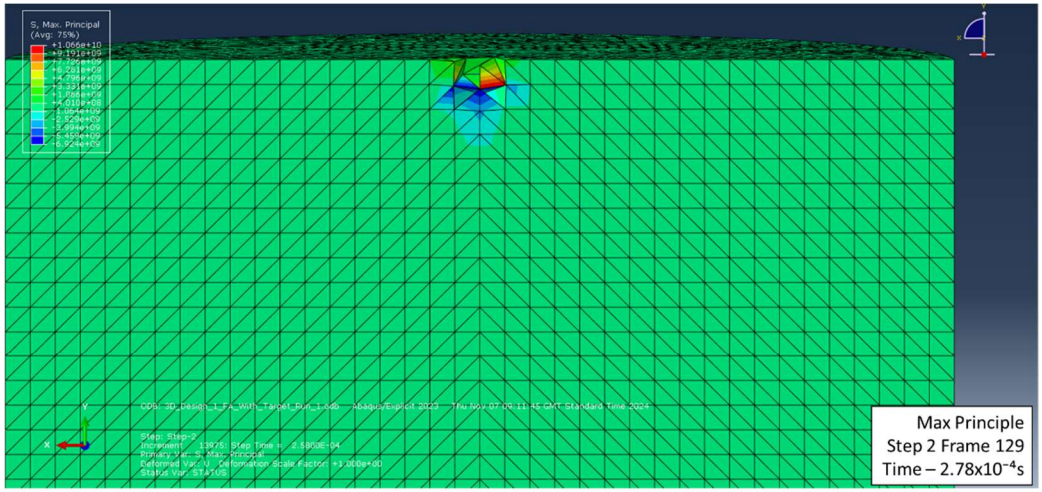


d) Step Two Frame 142, Time = 3.04×10^{-4}s

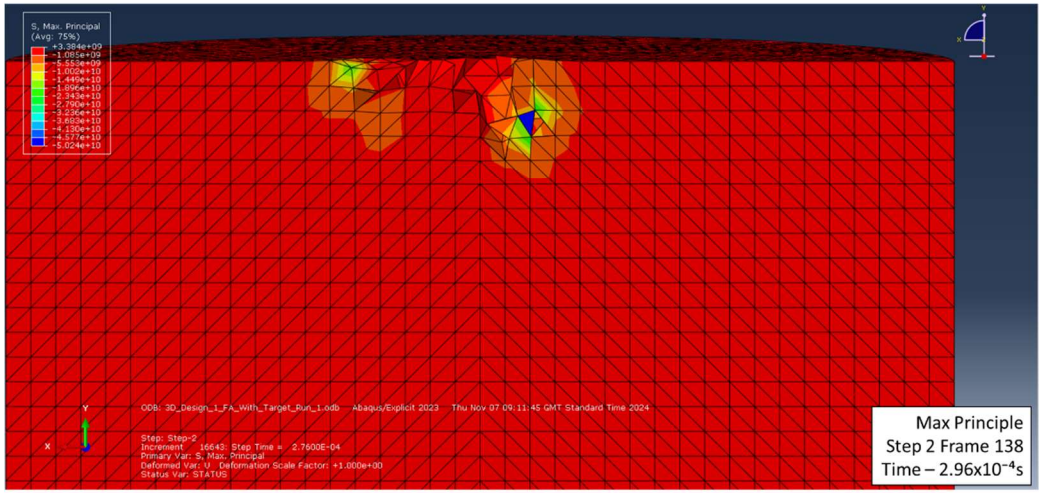
Figure 7-17 -- 3D_Design_Target_Run_1 Progression in Shear Stress at a) 2.72×10^{-4}s, b) 2.78×10^{-4}s, c) 2.96×10^{-4}s and d) 3.04×10^{-4}



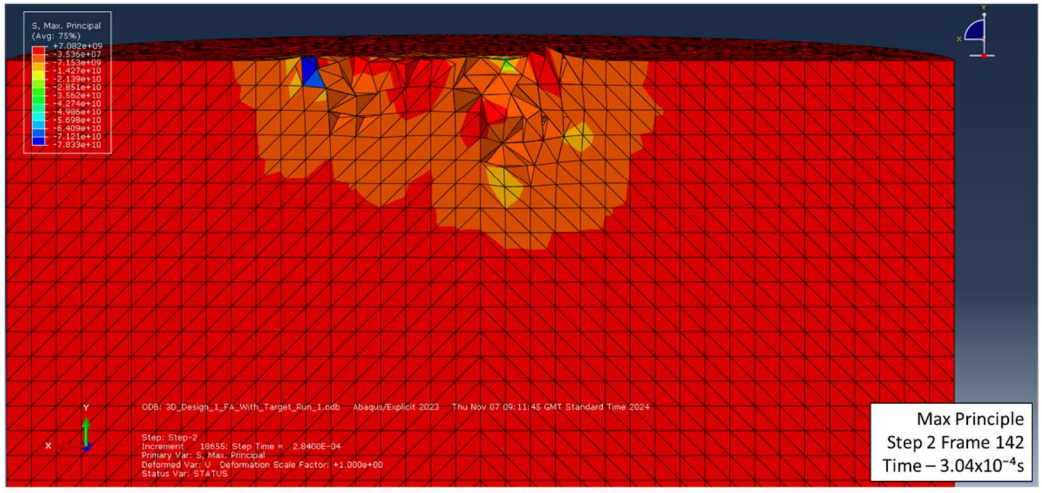
a) Step Two Frame 126, Time = 2.72x10^{-4}s



b) Step Two Frame 129, Time = 2.78x10^{-4}s



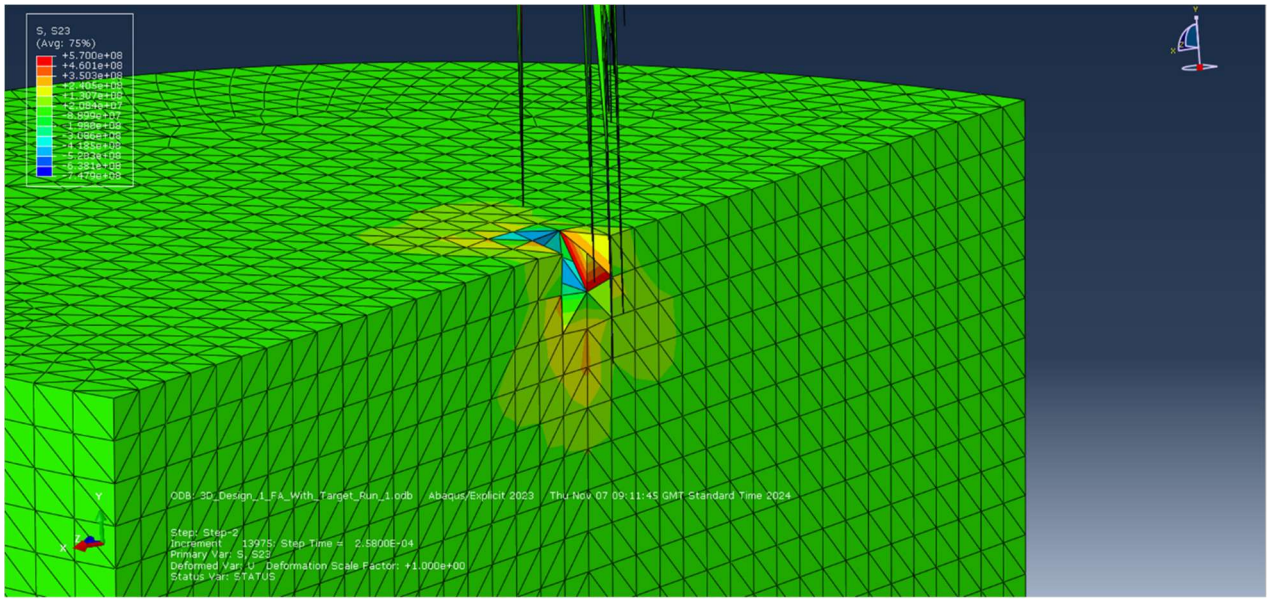
c) Step Two Frame 138, Time = 2.96x10^{-4}s



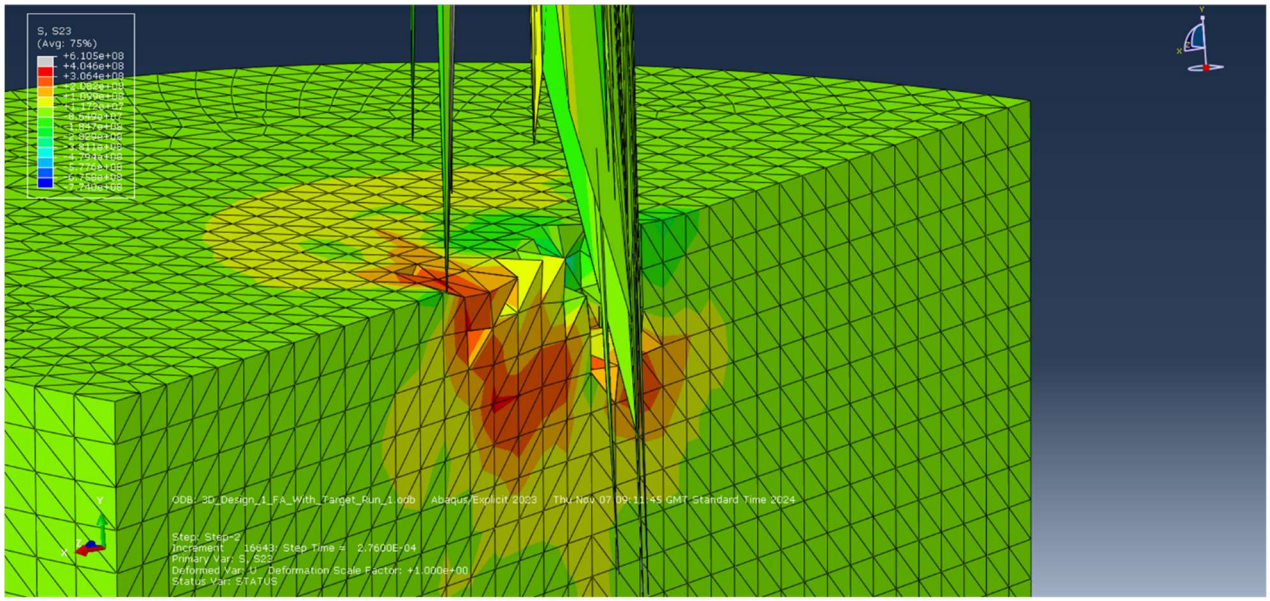
d) Step Two Frame 142, Time = 3.04x10^{-4}s

Figure 7-18 - 3D_Design_Target_Run_1 Penetration Progression in Max Principle at a) 2.72x10 $^{-4}$s, b) 2.78x10 $^{-4}$s, c) 2.96x10 $^{-4}$s and d) 3.04x10 $^{-4}$s

The stress waves are shown to have radiated out towards the edge of the target from the point of impact. Figure 7-19, shows the shear stress on the top of the target at a) $2.78x10^{-4}$s and b) $2.96x10^{-4}$s, during the liner penetration. If the liner was to penetrate further, it would be a reasonable expectation to see damage increase towards the edge of the target as well as deeper into it.



a) Step Two Frame 129, Time = $2.78x10^{-4}$s



b) Step Two Frame 138, Time = $2.96x10^{-4}$s

Figure 7-19 - 3D_Design_Target_Run_1 Representation of Shear Stress Radiating Towards the Edge of the Target

At the point of abortion, the liner has penetrated the target and caused damage to a depth of 0.075m, as highlighted in Figure 7-20.

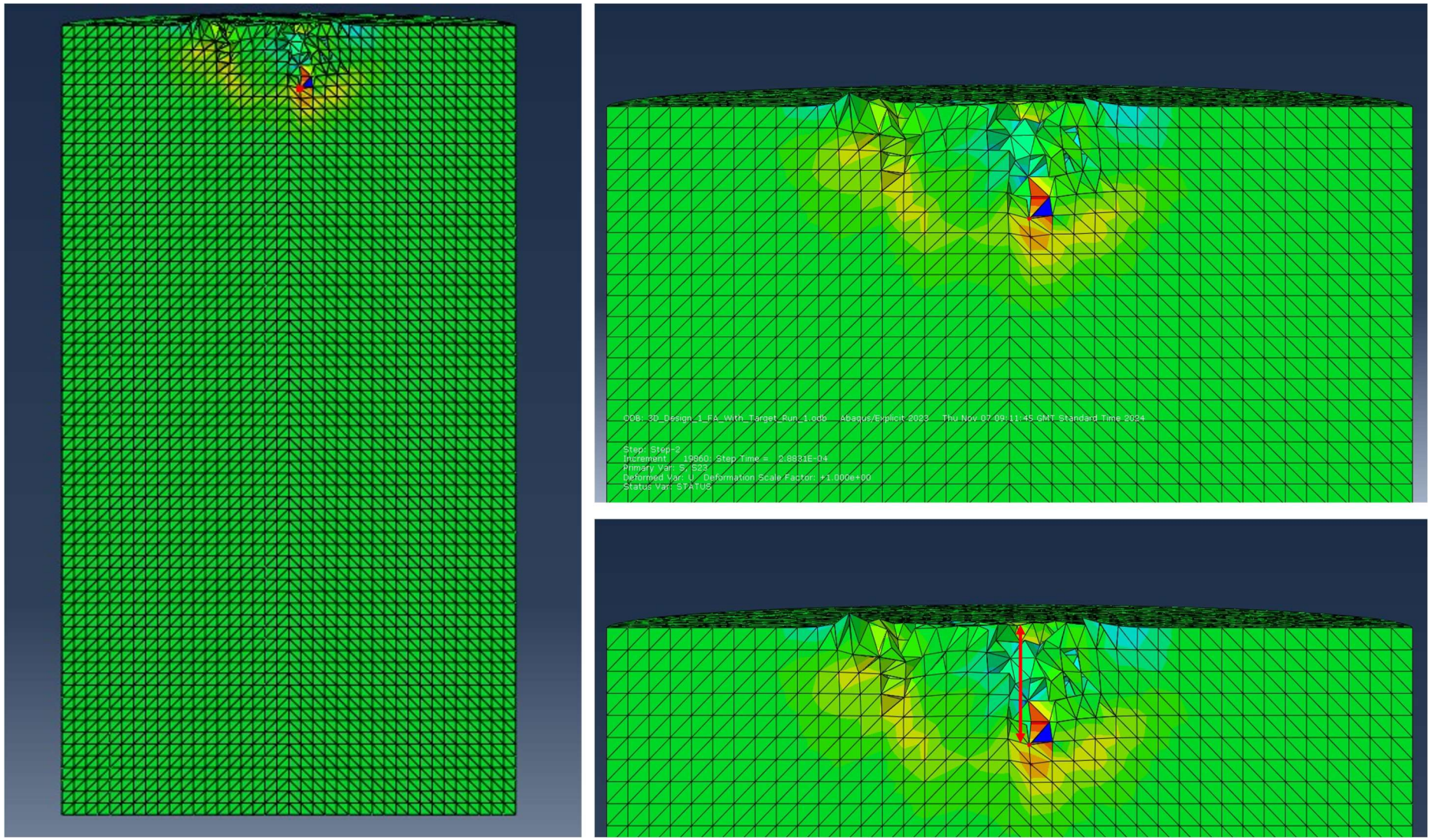


Figure 7-20 - 3D_Design_Target_Run_1 Penetration Depth

7.2.2.2 Second 3D Target Penetration Simulation Analysis

To improve the results, a finer mesh shown in Figure 7-21 with a gradual partition applied to the target.

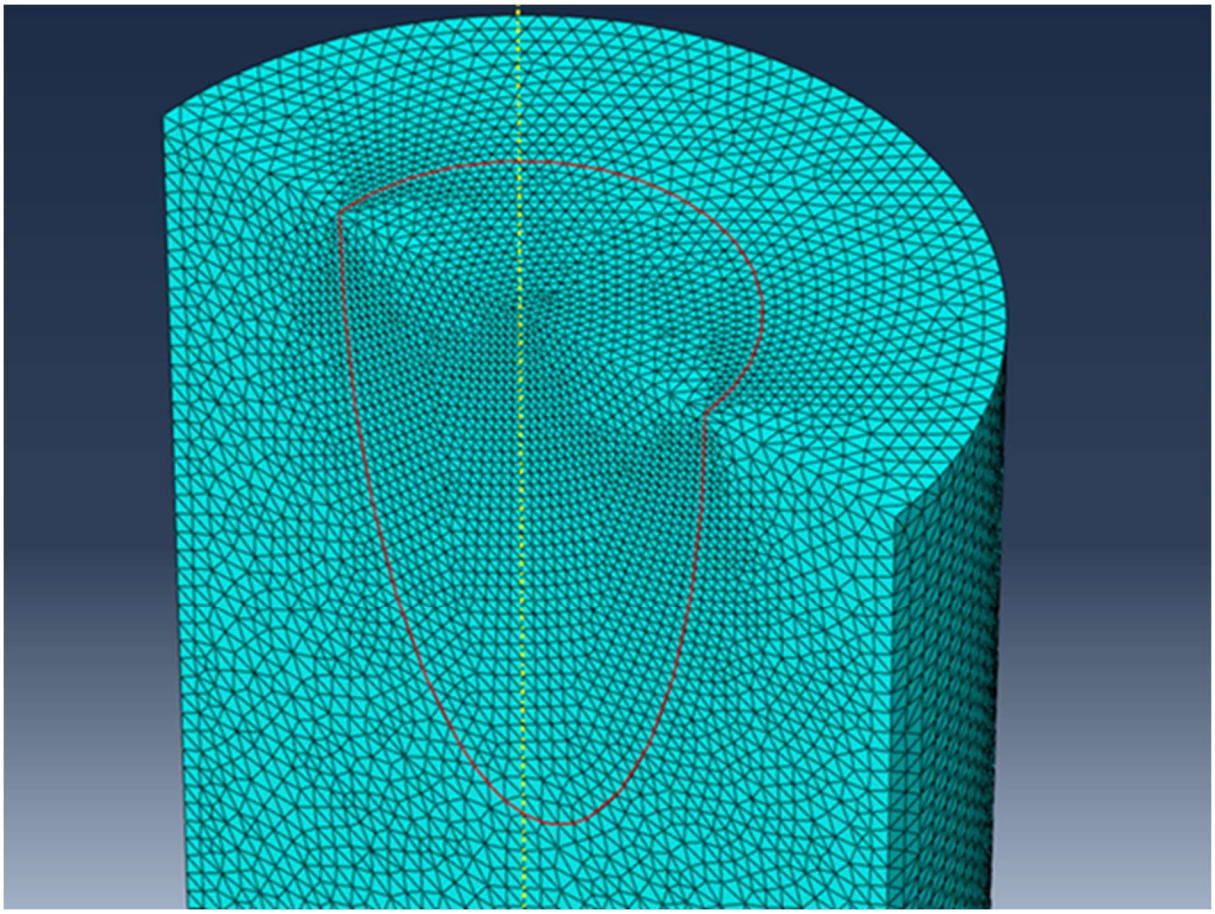


Figure 7-21 – 3D Target Finer Mesh Detailed View

This run (3D_Design_Target_Run_2) aborted due to an excessively distorted element in the liner after running for 2.5504×10^{-4}s in step two producing an output of 128 frames.

From the jet formation presented in Figure 7-22 a jet with a thinner tip was produced, however, it has the same approximate length as 3D_Design_Target_Run_1 of 1.2m with a velocity of $5.5 kms^{-1}$. This is evident in the displacement graph in Figure 7-23 and the velocity graph in Figure 7-24.

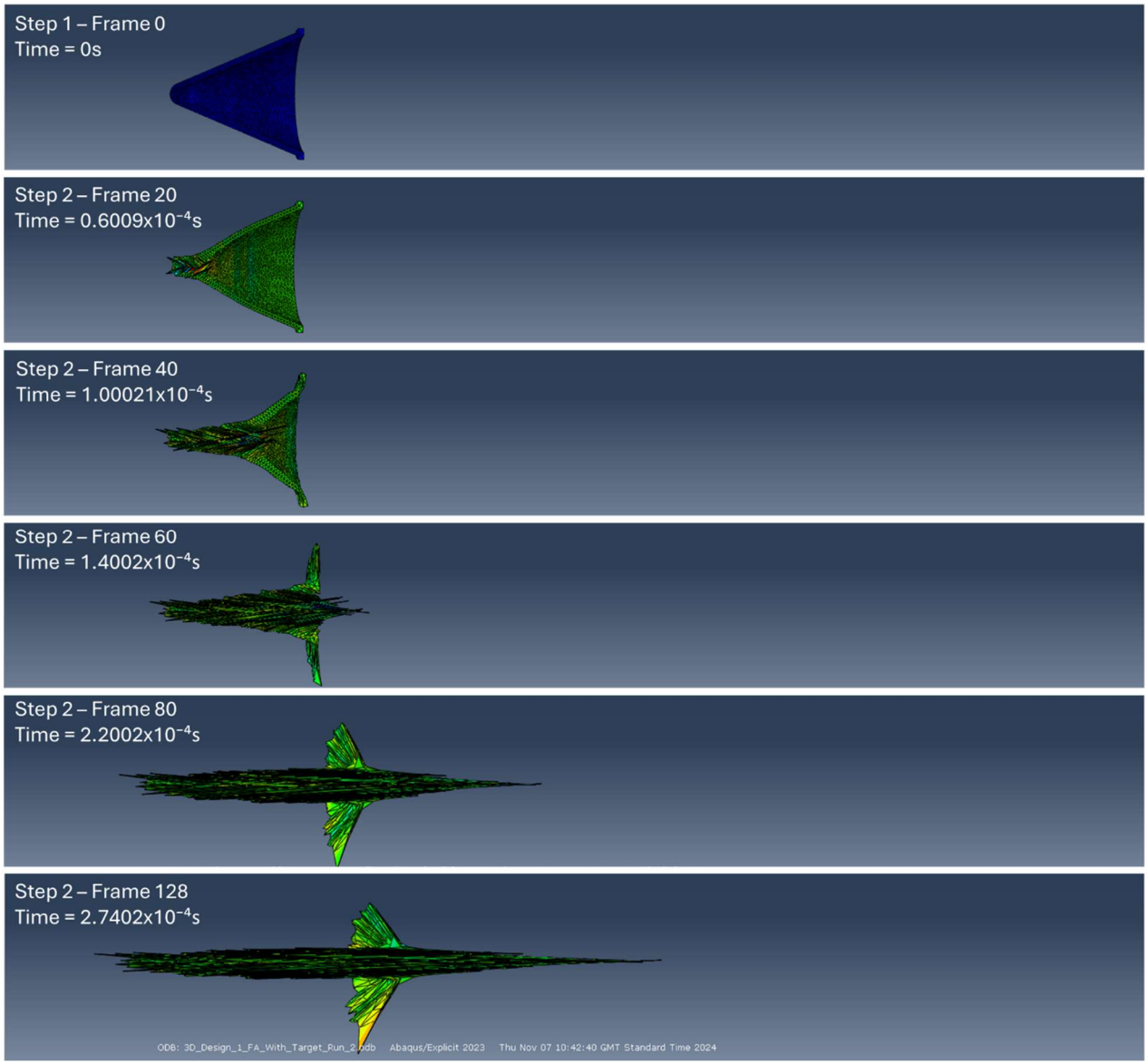


Figure 7-22 - 3D_Design_Target_Run_2 Jet Formation from Liner Collapse to Point of Abortion

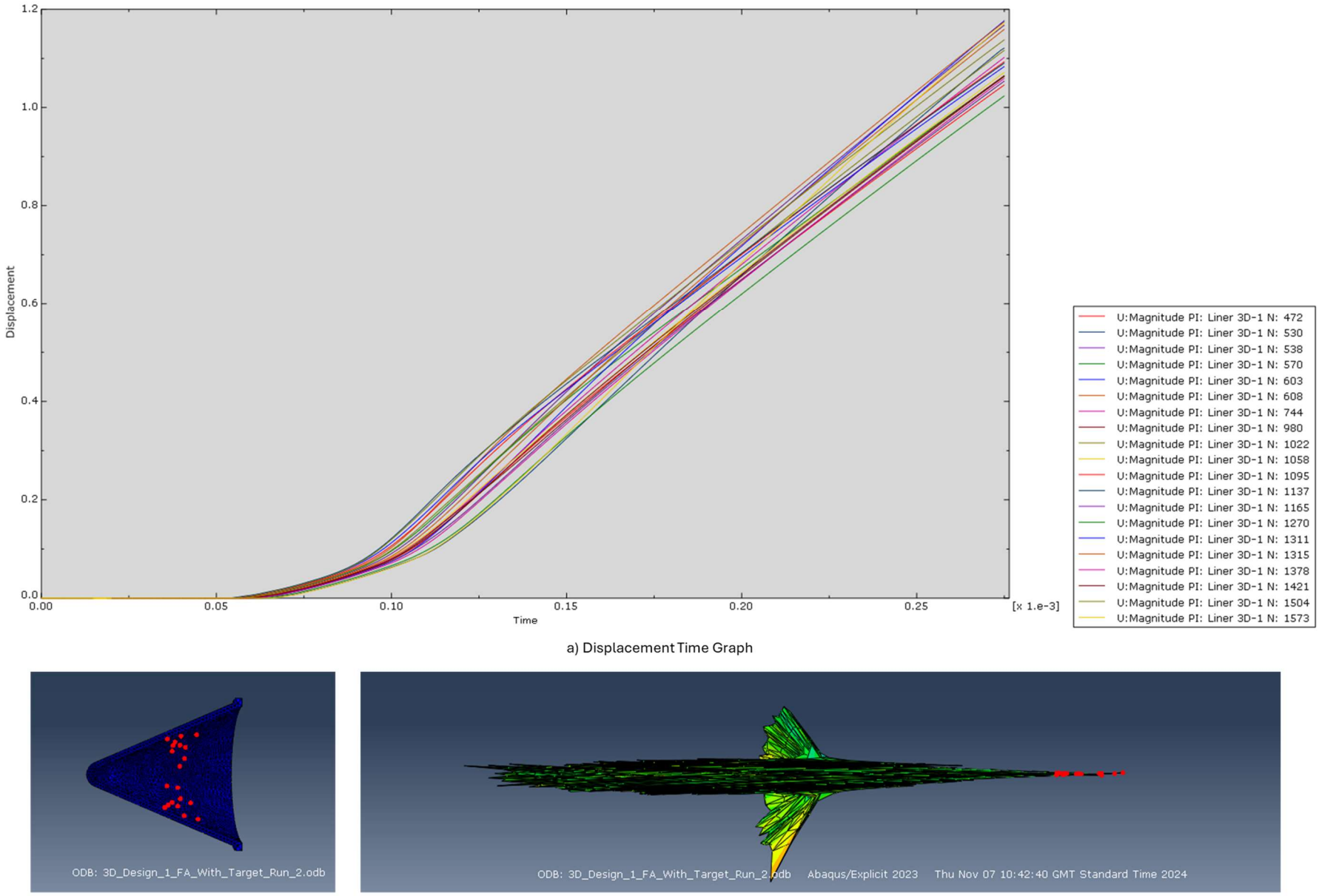
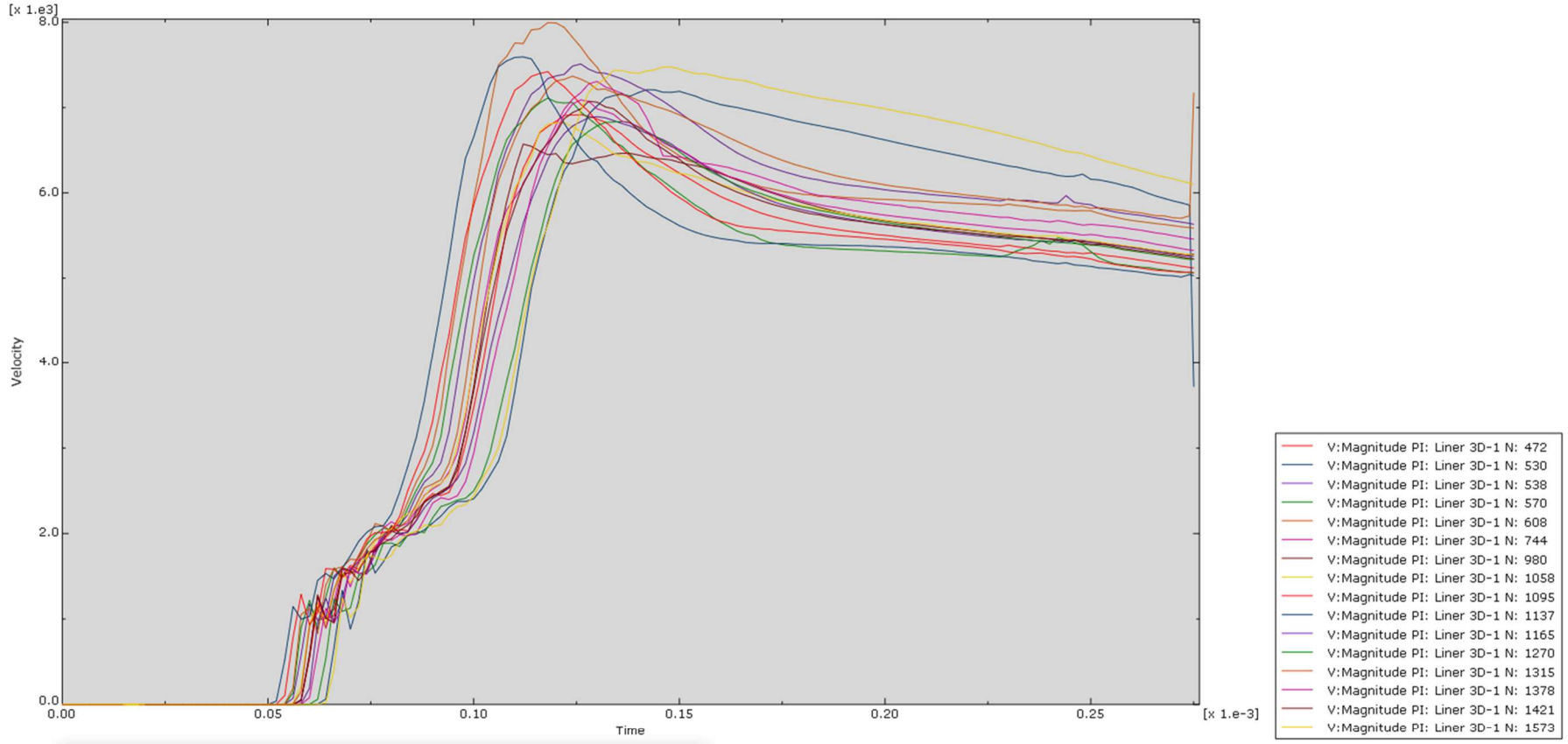
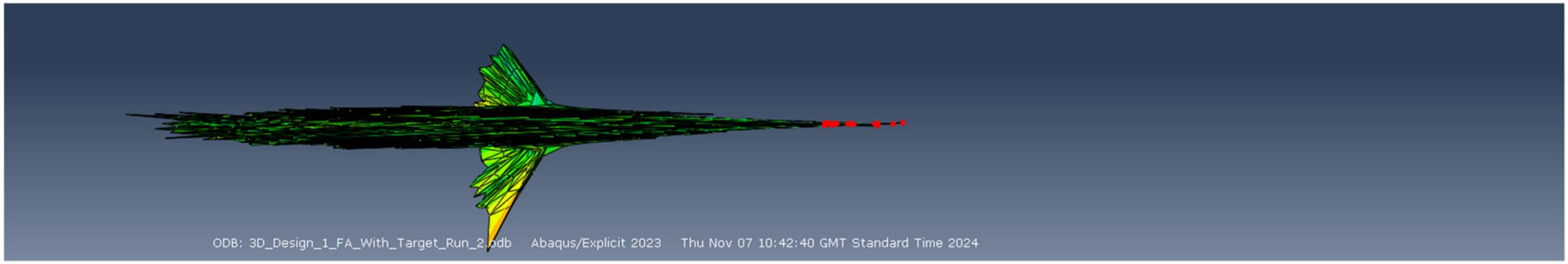


Figure 7-23 - 3D_Design_Target_Run_2 a) Displacement Graph with b) Selected Nodes



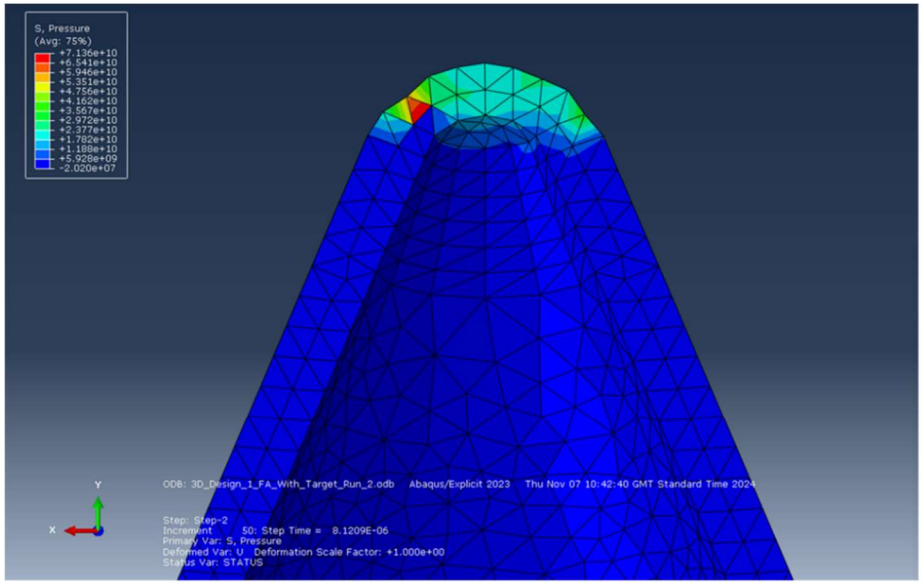
a) Velocity Time Graph



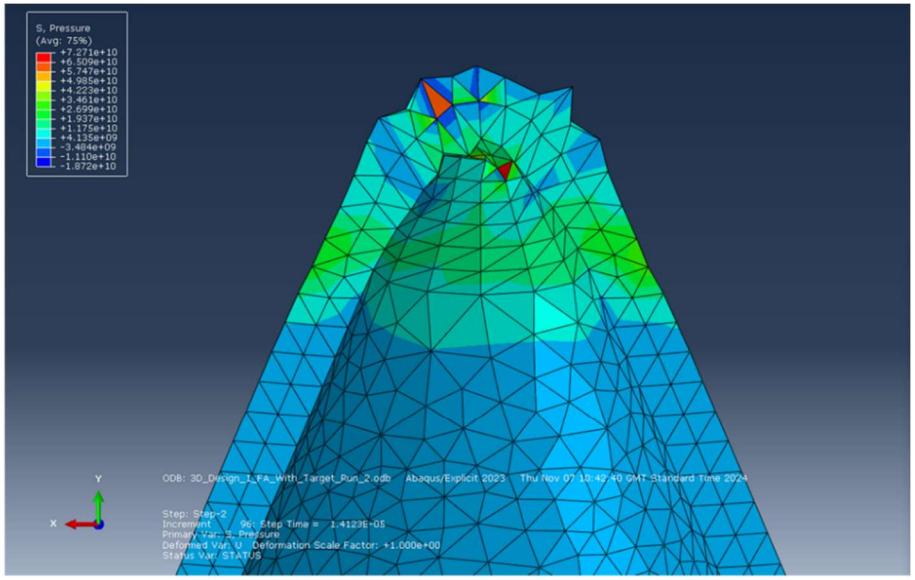
b) Selected nodes for Velocity Time Graph

Figure 7-24 - 3D_Design_Target_Run_2 a) Jet Velocity Graph with b) Selected Nodes

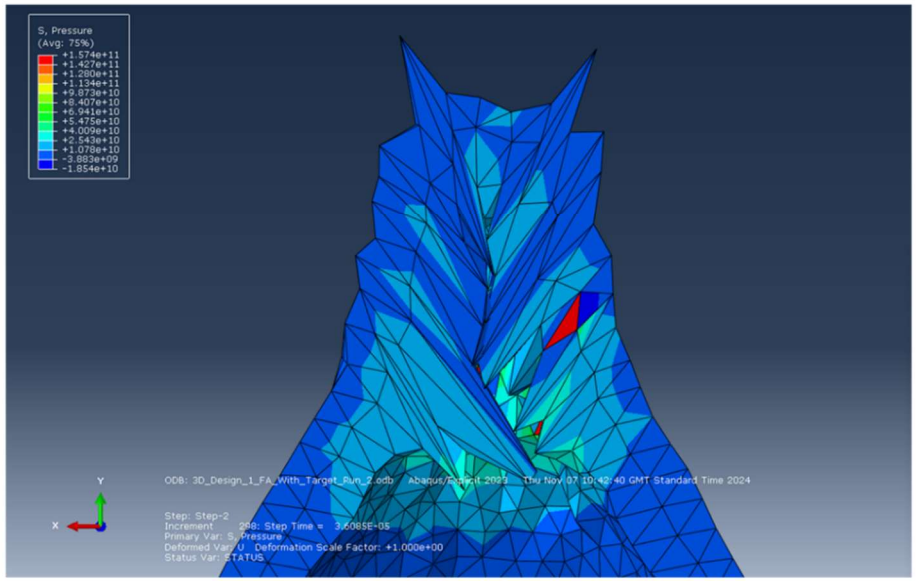
The liner experiences high pressure during its collapse, as is evident in Figure 7-25, with the pressure initially in the region of 10GPa at the apex and increasing to 25-30GPa on the sides of the liner. As the wave progresses, high pressures of 40-50GPa are achieved at 5.8909×10^{-5}s, with some areas reaching 150GPa which is significantly higher than the 2D simulations. Figure 7-26 highlights high compressive stresses of 20-30GPa while Figure 7-27 highlights low shear stress in the region of 0.2GPa. This indicates that compression is the main contributor to the liner collapse.



a) Step 2 Frame 4, Time = 2.8191×10^{-5}s

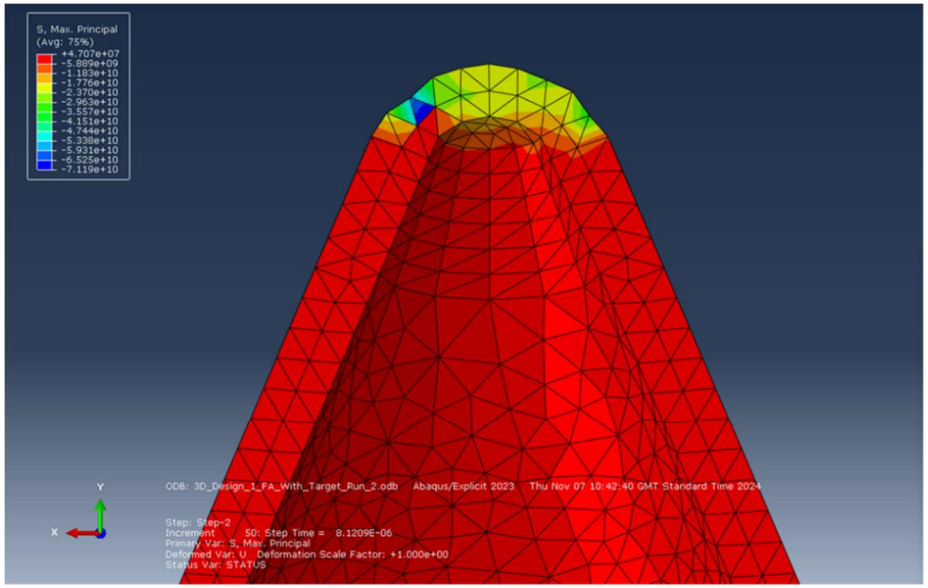


b) Step 2 Frame 7, Time = 3.4123×10^{-5}s

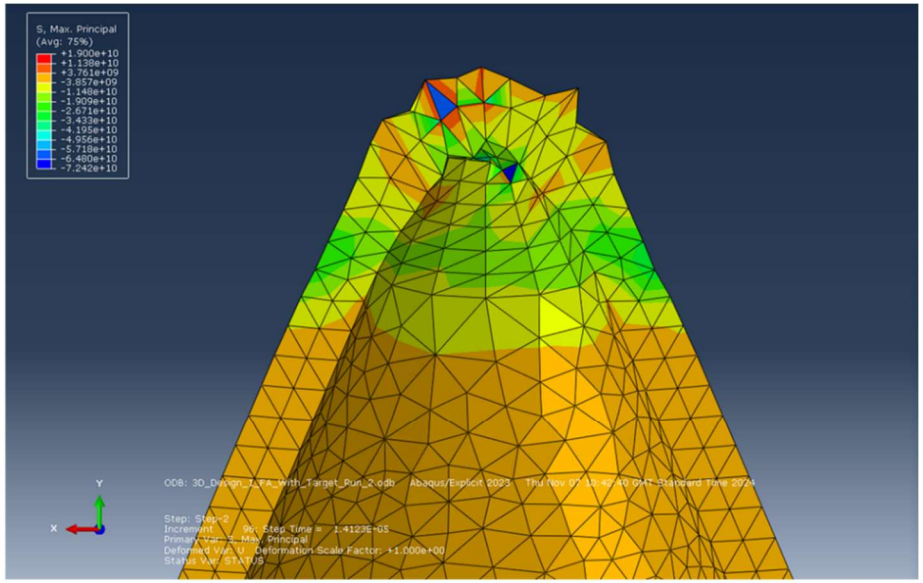


c) Step 2 Frame 18, Time = 5.8909×10^{-5}s

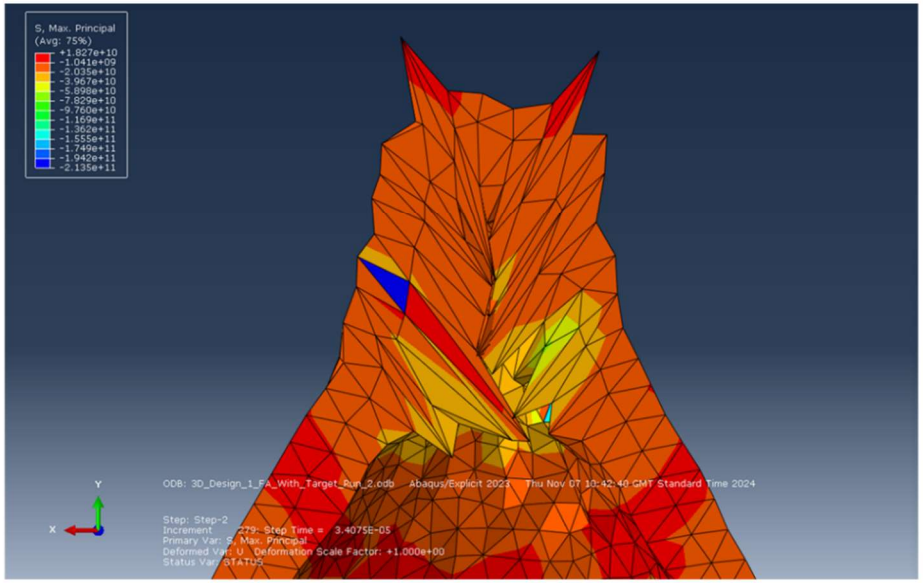
Figure 7-25 - 3D_Design_Target_Run_2 Liner Pressure at a) 2.8191×10^{-5}s, b) 3.4123×10^{-5}s, and c) 5.8909×10^{-5}s



a) Step 2 Frame 4, Time = 2.8191×10^{-5}s

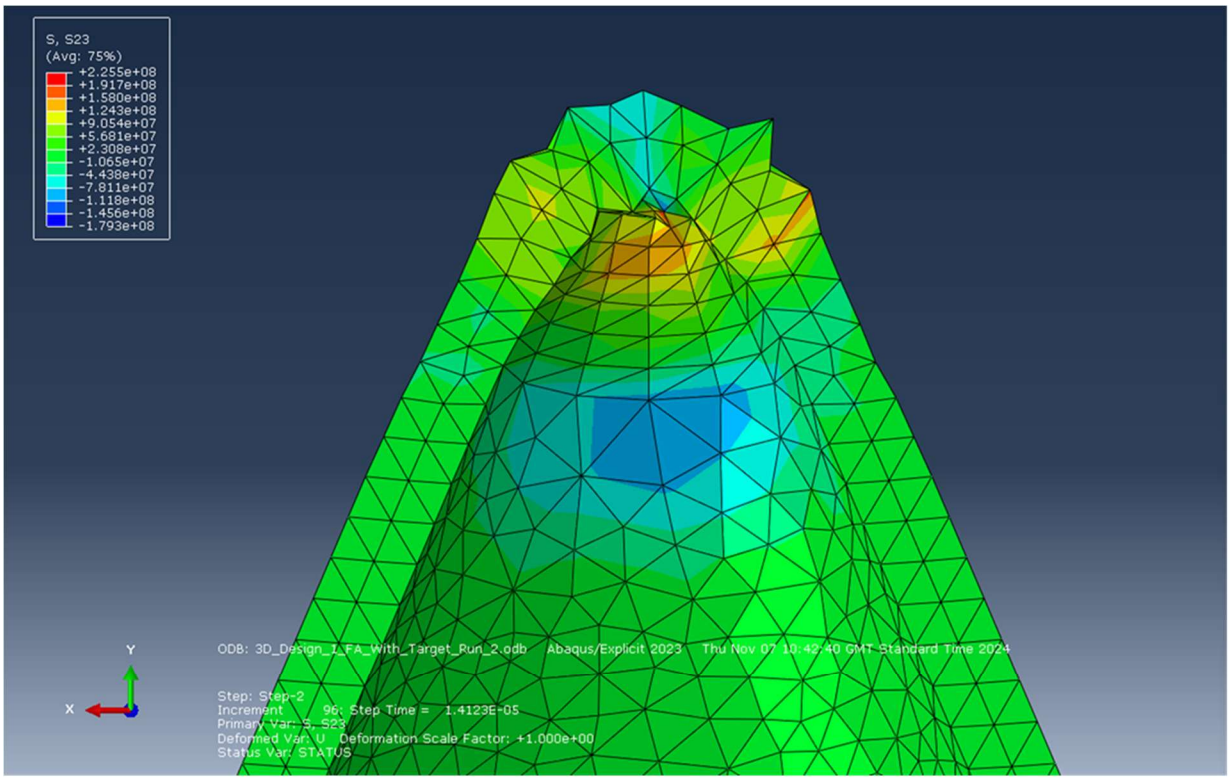


b) Step 2 Frame 7, Time = 3.4123×10^{-5}s

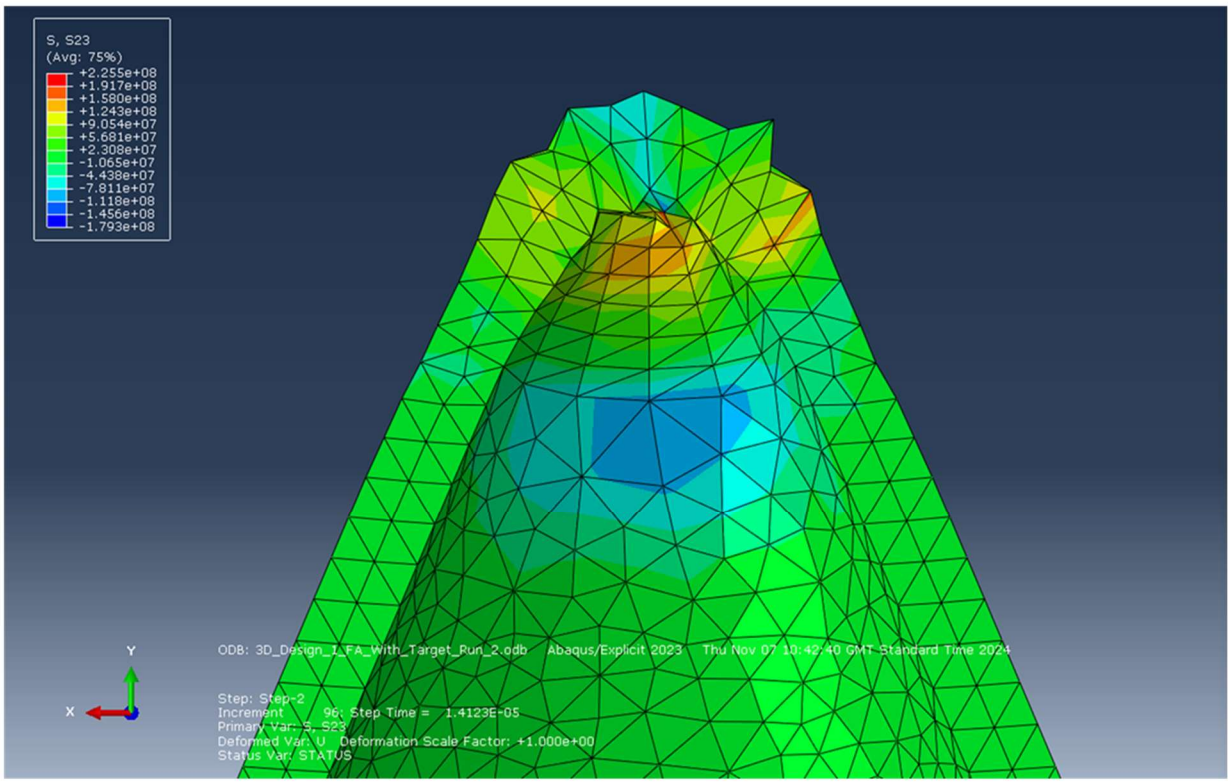


c) Step 2 Frame 18, Time = 5.8909×10^{-5}s

Figure 7-26 - 3D_Design_Target_Run_2 Max Principal Stress at a) 2.8191×10^{-5}s, b) 3.4123×10^{-5}s, and c) 5.8909×10^{-5}s



a) Step 2 Frame 7, Time = 3.4123×10^{-5}s



b) Step 2 Frame 18, Time = 5.8909×10^{-5}s

Figure 7-27 - 3D_Design_Target_Run_2 Shear stress at a) 3.4123×10^{-5}s, and b) 5.8909×10^{-5}s

The jet interacts with the target at the abortion point of 2.7504x10^{-4}s. From the results in Figure 7-28, areas of high pressure in the region of 30-40GPa were exerted onto the target.

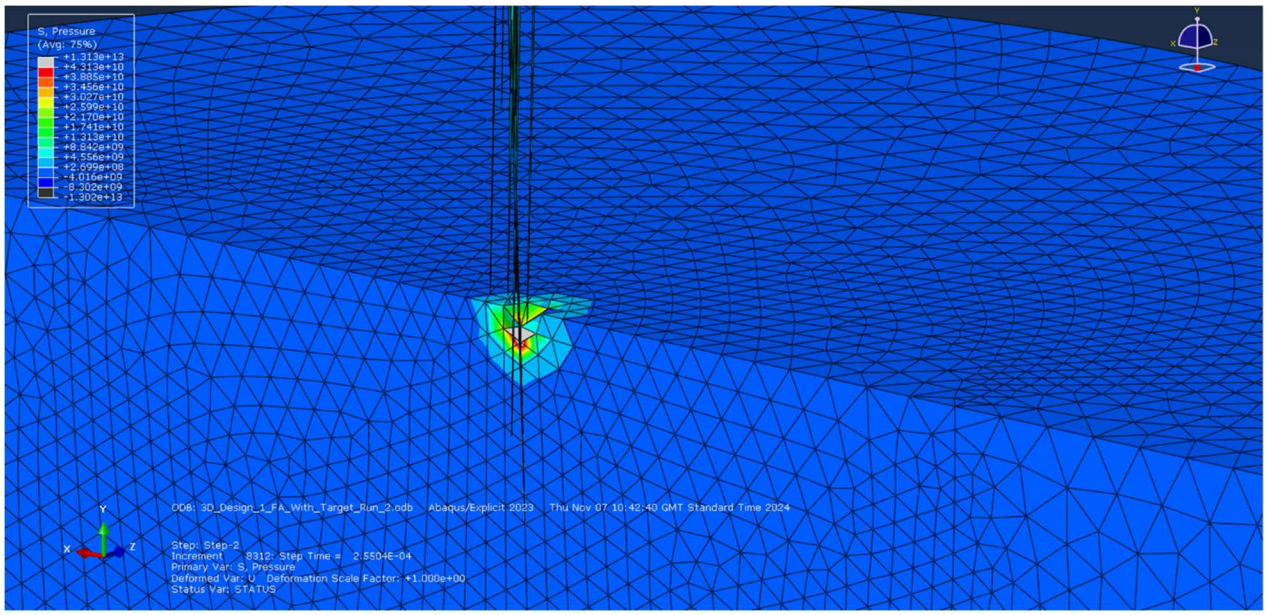


Figure 7-28 - 3D_Design_Target_Run_2 Target Interaction

The only variation in 3D_Design_Target_Run_2 compared to 3D_Design_Target_Run_1 is the addition of the gradual mesh in the target. This has had a clear impact on the jet formation and how the software has computed the simulated results.

8 Conclusion

This report analysed the jet formation and penetration capability of two shaped charge designs, using the FEA software Abaqus. Design One consisted of a constant thickness liner, whereas Design Two has a gradual thickness liner. Both designs were analysed in 2D with Design One taken forward for 3D analysis.

The 2D designs produced a jet capable of penetrating the steel target, with Design Two penetrating deeper to a depth of 0.54m. Both designs aborted before the simulation was complete due excessively distorted elements in the metal casing. Improvements to the metal casing's mesh either in size or the addition of element deletion, may enable the simulation to run further. Applying a damage model to the casing, may also improve the simulation, however, the additional computational costs need to be considered.

Design One was developed into a 3D model to see if conducting the simulation in 3D would improve the results. Due to the increased number of nodes and elements for the software to calculate, there was an additional computational cost to consider. The limit to the number of nodes available restricted the mesh of the 3D design, however, adaptive mesh provided a method to mitigate some problems.

The design produced a jet which interacted with the target, this jet was thicker and shorter than the 2D simulation. The mesh of the target significantly altered the jet formation, indicating the number of nodes and elements impact how the software calculated the simulation. Further study would be required to understand how and why this occurs.

Methods to improve the simulation include:

- Altering the adaptive mesh to incorporate the elements distorting excessively or adding an additional step of adaptive mesh to cover a new partition.
- Conducing the simulation on a version of the software that enables more nodes to allow further mesh refinement.

Overall, based on the results of the simulations produced, altering the design of a shaped charge liner does alter its performance. From the 2D simulations conducted it can be seen Design Two had greater penetrative power.

Simulating shaped charges in 2D provided better results for analysis as the 3D simulation encountered more computational challenges with its design and simulation.

9 References

[1] H. Mehmannavaz, A. Ramezani, M. A. Nabakhteh and G. Liaghat, "A Practical Review Study on Shaped Charge in The Last Two Decades (2000–2020)," *International Journal of Protctive Structures,* vol. 12(4), pp. 665-693, 2021.

[2] S. Sen and I. G. Aksoy, "An Application of Explosive Metal Forming in Military Field: The Relationship Between Shaped Charge Jet Formation and Thickness Variation Along Liner Length of Conical Copper Liner," *Arab J Sci Eng,* pp. 3551-3562, 4 September 2013.

[3] W. Walters, "An Overview of the Shape Charge Concept," 2003.

[4] W. P. Walters and J. A. Zukas, Fundamentals of Shaped Charges, John Wiley & Sons, Inc, 1989.

[5] T. Elshenawy, E. Ezzat, A. M. Riad and M. A. Elkader, "Influence of Liner Wall Thickenss on the Penetration Performance of PETEN-HTPB PBX-based Shaped Charges into Steel Target," *Central European Journal of Energetic Materials,* vol. 19(1), pp. 63-90, 31 March 2022.

[6] M. Kumar, Y. Singh and P. Kumar, "Effect of Liner Cone Angle, Liner Thickness and Wave Shaper in Large Caliber Shaped Charge Warheads," *Explosion Shock Waves and High Strain Rate Phenomena,* vol. 13, pp. 134-140, 2019.

[7] K. Naeem, A. Hussain and S. Abbas, "A Review of Shaped Charge Variables for its Optiumn Performance," *Engineering, Technology & Applies Science Research,* vol. 9, no. 6, pp. 4917-4924, 2019.

[8] S. Y. Mohamed, A. M. Riad and Y. Kresha, "Modeling of Shaped Charge Jet Formation," in *9th International Conference on Aerospace Sciences and Avaiation Technology*, Cairo, Egypt, 2001.

[9] P. Dehestani, A. Fathi and H. M. Daniali, "Numerical Study of the Stand-off Distance and Liner Thickness Effect on the Penetration Depth Efficiency of Shaped Charge Process," *Journal of Mechanical Engineering Science,* vol. 233(3), pp. 977-986, 2019.

[10] C. Poole, "Penetration of a Shaped Charge," 2005.

[11] T. A. E. Elshenawy, "Criteria of Design Improvement of Shaped Charges Used as Oil Well Perforators," 2012.

[12] SyBridge Technologies, "A Beginner's Guide to Finite Element Analysis (FEA)," 7 July 2021. [Online]. Available: https://sybridge.com/finite-element-analysis-guide/. [Accessed 2024 October 20].

[13] V. K. R. Sirigiri, V. Y. Gudiga, U. S. Gattu, G. Suneesh and K. M. Buddaraju, "A Review on Johnson Cook Material Model," *Materials Today: Proceedings,* vol. 62, pp. 3450-3456, 26 April 2022.

[14] H. Cai, P. Song, X.-H. Gu, H. Zhou, B.-Y. Xing, L. Jiang and R. Guo, “Determination of the JWL Parameters of Detonation Products Using Adaptive Genetic Algorithm,” *Propellants, Explosives and Pyrotechnics,* vol. 45, pp. 1920-1930, 9 Novemeber 2020.

[15] O. Heuze, “Complete Forms of Mie-Gruneisen Equation of State,” *AIP Conference Proceedings,* vol. 1793(1), pp. 050001-1 - 050001-4, 13 January 2017.

[16] B. Zhu, L. Xiong and M. Xu, “Double-edged cutting simulation with a New Combined Constitutive Model for AISI 1045 Steel,” *Journal of Materials Processing Tech.,* vol. 302, pp. 1-13, 12 January 2022.

[17] Y. Kang and J. Jeon, “Finite Element Analysis of The Impact of Liner Thickness and Hydrodynamic Limit on The Penetration Depth of a Shaped Charge Warhead,” *Journal of Mechanical Science and Technology,* vol. 13(12), pp. 5797-5805, 30 August 2018.

[18] “AISI 1045 Steel, Cold Drawn, Annealed, 19-32mm (0.75-1.25 in) round,” [Online]. Available: https://matweb.com/search/DataSheet.aspx?MatGUID=43364bf60fe843f9bd4daf66f31c2535&ckck=1. [Accessed 2024 October 15].

[19] D. Somasundaram, S. K. Roy, M. Trabia, B. O’Toole and R. Hixson, “Parametric Sensistivity Comparison of Simulation Models for Flyer Plate Impact Experiments,” *Journal of Computational and Experimental Methods,* vol. 3, no. 4, pp. 305-315, 2015.

[20] D. Christman, W. M. Isbell and S. G. Babcock, “Measurements of Dynamic Properties of Materials - Volume V: OFHC Copper,” 1971.

[21] J. Pinto and D. A. Wiegand, “Yield and Plastic Flow in Composition B and TNT,” 1993.

[22] SIMULIA, “Abaqus Material Data Definiation,” [Online]. Available: https://help.3ds.com/2023/english/dssimulia_established/SIMACAEMATRefMap/simamat-c-materialdata.htm?contextscope=all. [Accessed 15 December 2024].

[23] Structural Numerical Research Center, “Understanding and Fixing Distorted Elements in Abaqus,” [Online]. Available: https://numericalarchive.com/2024/03/22/understanding-and-fixing-distorted-elements-in-abaqus/. [Accessed 15 December 2024].

[24] “14.6 Understanding Adaptive Meshing,” [Online]. Available: https://classes.engineering.wustl.edu/2009/spring/mase5513/abaqus/docs/v6.5/books/usi/default.htm?startat=pt03ch14s06.html. [Accessed 15 December 2024].